

Towards an Understanding of the Correlations in Jet Substructure

Report of BOOST2013, hosted by the University of Arizona, 12th-16th of August 2013.

D. Adams¹, A. Arce², L. Asquith³, M. Backovic⁴, T. Barillari⁵, P. Berta⁶, D. Bertolini²,
A. Buckley⁸, J. Butterworth⁹, R. C. Camacho Toro¹⁰, J. Caudron⁹, Y.-T. Chien¹¹, J. Cogan¹²,
B. Cooper⁹, D. Curtin¹⁷, C. Debenedetti¹⁸, J. Dolen⁹, M. Eklund²², S. El Hedri²²,
S. D. Ellis²², T. Embry²², D. Ferencek²³, J. Ferrando²⁴, S. Fleischmann¹⁶, M. Freytsis²⁵,
M. Giulini²¹, Z. Han²⁷, D. Hare⁴, P. Harris⁴, A. Hinzmann⁴, R. Hoing⁴, A. Hornig²²,
M. Jankowiak⁴, K. Johns²⁸, G. Kasieczka²³, T. Knight²⁴, G. Kasieczka²⁹, R. Kogler³⁰,
W. Lampl⁴, A. J. Larkoski⁴, C. Lee³¹, R. Leone³¹, P. Loch³¹, D. Lopez Mateos²⁷,
H. K. Lou²⁷, M. Low²⁷, P. Maksimovic³², I. Marchesini³², S. Marzani³², L. Masetti³³,
R. McCarthy³², S. Menke³², D. W. Miller³⁵, K. Mishra³⁶, B. Nachman³², P. Nef⁴,
F. T. O'Grady²⁴, A. Ovcharova²³, A. Picazio³⁷, C. Pollard³⁸, B. Potter Landua²⁹,
C. Potter²⁹, S. Rappoccio³⁹, J. Rojo⁴⁸, J. Rutherford⁴⁰, G. P. Salam^{10,11}, J. Schabinger²³,
A. Schwartzman⁴, M. D. Schwartz²⁷, B. Shuve⁴³, P. Sinervo⁴⁴, D. Soper⁴⁵,
D. E. Sosa Corral⁴⁵, M. Spannowsky³², E. Strauss³⁴, M. Swiatlowski⁴, J. Thaler³⁴,
C. Thomas³⁴, E. Thompson¹, N. V. Tran³⁶, J. Tseng³⁶, E. Usai³⁶, L. Valery³⁶, J. Veatch²³,
M. Vos²³, W. Waalewijn⁴, and C. Young⁴⁷

¹Columbia University, Nevis Laboratory, Irvington, NY 10533, USA

²Duke University, Durham, NC 27708, USA

³Argonne National Laboratory, Lemont, IL 60439, USA

⁴SLAC National Accelerator Laboratory, Menlo Park, CA 94025, USA

⁵Deutsches Elektronen-Synchrotron, DESY, D-15738 Zeuthen, Germany

⁶Cornell University, Ithaca, NY 14853, USA

⁷Lund University, Lund, SE 22100, Sweden

⁸University of Edinburgh, EH9 3JZ, UK

⁹University College London, WC1E 6BT, UK

¹⁰LPTHE, UPMC Univ. Paris 6 and CNRS UMR 7589, Paris, France

¹¹CERN, CH-1211 Geneva 23, Switzerland

¹²CAFPE and U. of Granada, Granada, E-18071, Spain

¹³McGill University, Montreal, Quebec H3A 2T8, Canada

¹⁴Iowa State University, Ames, Iowa 50011, USA

¹⁵Rutgers University, Piscataway, NJ 08854, USA

¹⁶Bergische Universitaet Wuppertal, Wuppertal, D-42097, Germany

¹⁷YITP, Stony Brook University, Stony Brook, NY 11794-3840, USA

¹⁸University of Manchester, Manchester, M13 9PL, UK

¹⁹UNESP - Universidade Estadual Paulista, Sao Paulo, 01140-070, Brazil

²⁰INFN and University of Naples, IT80216, Italy

²¹University of Geneva, CH-1211 Geneva 4, Switzerland

²²University of Washington, Seattle, WA 98195, USA

²³Instituto de Fisica Corpuscular, IFIC/Csic-UVeG, E-46071 Valencia, Spain

²⁴University of Glasgow, Glasgow, G12 8QQ, UK

²⁵Berkeley National Laboratory, University of California, Berkeley, CA 94720, USA

²⁶Universidad de Buenos Aires, AR-1428, Argentina

²⁷Harvard University, Cambridge, MA 02138, USA

²⁸Weizmann Institute, 76100 Rehovot, Israel

²⁹Universitaet Hamburg, DE-22761, Germany

³⁰Universitaet Heidelberg, DE-69117, Germany

³¹University of Arizona, Tucson, AZ 85719, USA

³²IPPP, University of Durham, Durham, DH1 3LE, UK

³³Universitaet Mainz, DE 55099, Germany

³⁴MIT, Cambridge, MA 02139, USA

³⁵University of Chicago, IL 60637, USA

³⁶Fermi National Accelerator Laboratory, Batavia, IL 60510, USA

³⁷Indiana University, Bloomington, IN 47405, USA

³⁸University of California, Davis, CA 95616, USA

³⁹Johns Hopkins University, Baltimore, MD 21218, USA

⁴⁰INFN and University of Pisa, Pisa, IT-56127, Italy

⁴¹Texas A & M University, College Station, TX 77843, USA

⁴²INFN and University of Calabria, Rende, IT-87036, Italy

⁴³Brown University, Richmond, RI 02912, USA

⁴⁴Yale University, New Haven, CT 06511, USA

⁴⁵CEA Saclay, Gif-sur-Yvette, FR-91191, France

⁴⁶University of Illinois, Chicago, IL 60607, USA

⁴⁷University of California, Berkeley, CA 94720, USA

Abstract Insert your abstract here. Insert your abstract here. Insert your abstract here. Insert your abstract here. Insert your abstract here. Insert your abstract here. Insert your abstract here.

1 Introduction

The characteristic feature of collisions at the LHC is a center-of-mass energy, 7 TeV in 2010 and 2011, of 8 TeV in 2012, and near 14 TeV with the start of the second phase of operation in 2015, that is large compared to even the heaviest of the known particles. Thus these particles (and also previously unknown ones) will often be produced at the LHC with substantial boosts. As a result, when decaying hadronically, these particles will not be observed as multiple jets in the detector, but rather as a single hadronic jet with distinctive internal substructure. This realization has led to a new era of sophistication in our understanding of both standard QCD jets and jets containing the decay of a heavy particle, with an array of new jet observables and detection techniques introduced and studied. To allow the efficient sharing of results from these jet substructure studies, a series of BOOST Workshops have been held on a yearly basis: SLAC (2009, [?]), Oxford University (2010, [?]), Princeton University (2011, [?]), IFIC Valencia (2012 [?]), University of Arizona (2013 [?]), and, most recently, University College London (2014 [?]). After each of these meetings Working Groups have functioned during the following year to generate reports highlighting the most interesting new results, including studies of ever maturing details. Previous BOOST reports can be found at [1–3].

This report from BOOST 2013 thus views the study and implementation of jet substructure techniques as a fairly mature field, and focuses on the question of the correlations between the plethora of observables that have been developed and employed, and their dependence on the underlying jet parameters, especially the jet radius R and jet p_T . Samples of quark-, gluon-, W - and Top-initiated jets are reconstructed at the particle-level using FASTJET [4], and the performance, in terms of separating signal from background, of various groomed jet masses and jet substructure observables investigated through Receiver Operating Characteristic (ROC) curves, which show the efficiency to “tag” the signal as a function of the efficiency (or rejection, being $1/\text{efficiency}$) to “tag” the background. We investigate the separation of a quark signal from a gluon background (q/g tagging), a W signal from a gluon background (W -tagging) and a Top signal from a mixed quark/gluon QCD background (Top-tagging). In the case of Top-tagging, we also investigate the performance of dedicated Top-tagging algorithms, the HepTopTagger [5] and the Johns Hopkins Tagger [6]. Using multivariate techniques, we study the degree to which

the discriminatory information provided by the observables and taggers overlaps, by examining in particular the extent to which the signal-background separation performance increases when two or more variables/taggers are combined, via a Boosted Decision Tree (BDT), into a single discriminant.

The report is organized as follows. In Section 2 we describe the generation of the Monte Carlo event samples that we use in the studies that follow. In Section 3 we detail the jet algorithms, observables and taggers investigated in each section of the report, and in Section 4 the multivariate techniques used to combine the one or more of the observables into single discriminants. In Section 5 we describe the q/g-tagging studies, in Section 6 we describe the W -tagging studies, and in Section 7 we describe the Top-tagging studies. Finally we offer some summary of the studies and general conclusions in Section 8.

2 Monte Carlo Samples

In the below sections the Monte Carlo samples used in the q/g tagging, W tagging and Top tagging sections of this report are described. Note that in all cases the samples used contain no additional proton-proton interactions beyond the hard scatter (no pile-up), and there is no attempt to emulate the degradation in angular and p_T resolution that would result when reconstructing the jets inside a real detector.

2.1 Quark/gluon and W tagging

Samples were generated at $\sqrt{s} = 8$ TeV for QCD dijets, and for W^+W^- pairs produced in the decay of a (pseudo) scalar resonance and decaying hadronically. The QCD events were split into subsamples of gg and $q\bar{q}$ events, allowing for tests of discrimination of hadronic W bosons, quarks, and gluons.

Individual gg and $q\bar{q}$ samples were produced at leading order (LO) using MADGRAPH5 [7], while W^+W^- samples were generated using the JHU GENERATOR [8–10] to allow for separation of longitudinal and transverse polarizations. Both were generated using CTEQ6L1 PDFs [11]. The samples were produced in exclusive p_T bins of width 100 GeV, with the slicing parameter chosen to be the p_T of any final state parton or W at LO. At the parton-level the p_T bins investigated were 300–400 GeV, 500–600 GeV and 1.0–1.1 TeV. Since no matching was performed, a cut on any parton was equivalent. The samples were then all showered through PYTHIA8 (version 8.176) [12] using the default tune 4C [13]. **ED: Need to report the size of the samples used**

2.2 Top tagging

Samples were generated at $\sqrt{s} = 14$ TeV. Standard Model dijet and top pair samples were produced with SHERPA 2.0.Q [14–19], with matrix elements of up to two extra partons matched to the shower. The top samples included only hadronic decays and were generated in exclusive p_T bins of width 100 GeV, taking as slicing parameter the maximum of the top/anti-top p_T . The QCD samples were generated with a cut on the leading parton-level jet p_T , where parton-level jets are clustered with the anti- k_t algorithm and jet radii of $R = 0.4, 0.8, 1.2$. The matching scale is selected to be $Q_{\text{cut}} = 40, 60, 80$ GeV for the $p_{T \text{ min}} = 600, 1000, \text{ and } 1500$ GeV bins, respectively. For the top samples, 100k events were generated in each bin, while 200k QCD events were generated in each bin.

3 Jet Algorithms and Substructure Observables

In this section, we define the jet algorithms and observables used in our analysis. Over the course of our study, we considered a larger set of observables, but for the final analysis we eliminated redundant observables for presentation purposes. In Sections 3.1, 3.2, 3.3 and 3.4 we first describe the various jet algorithms, groomers, taggers and other substructure variables used in these studies.

3.1 Jet Clustering Algorithms

Jet clustering: Jets were clustered using sequential jet clustering algorithms [20] implemented in FASTJET 3.0.3. Final state particles i, j are assigned a mutual distance d_{ij} and a distance to the beam, d_{iB} . The particle pair with smallest d_{ij} are recombined and the algorithm repeated until the smallest distance is instead the distance to the beam, d_{iB} , in which case i is set aside and labelled as a jet. The distance metrics are defined as

$$d_{ij} = \min(p_{Ti}^{2\gamma}, p_{Tj}^{2\gamma}) \frac{\Delta R_{ij}^2}{R^2}, \quad (1)$$

$$d_{iB} = p_{Ti}^{2\gamma}, \quad (2)$$

where $\Delta R_{ij}^2 = (\Delta\eta)^2 + (\Delta\phi)^2$. In this analysis, we use the anti- k_t algorithm ($\gamma = -1$) [21], the Cambridge/Aachen (C/A) algorithm ($\gamma = 0$) [22, 23], and the k_t algorithm ($\gamma = 1$) [24, 25], each of which has varying sensitivity to soft radiation in defining the jet.

Qjets: We also perform non-deterministic jet clustering [26]. Instead of always clustering the particle pair with smallest distance d_{ij} , the pair selected for combination is chosen probabilistically according to a measure

$$P_{ij} \propto e^{-\alpha(d_{ij}-d_{\text{min}})/d_{\text{min}}}, \quad (3)$$

where d_{min} is the minimum distance for the usual jet clustering algorithm at a particular step. This leads to a different cluster sequence for the jet each time the Qjet algorithm is used, and consequently different substructure properties. The parameter α is called the rigidity and is used to control how sharply peaked the probability distribution is around the usual, deterministic value. The Qjets method uses statistical analysis of the resulting distributions to extract more information from the jet than can be found in the usual cluster sequence. We use $\alpha = 0.1$ and 25 trees per event for all of the studies presented here.

3.2 Jet Grooming Algorithms

Pruning: Given a jet, re-cluster the constituents using the C/A algorithm. At each step, proceed with the merger as usual unless both

$$\frac{\min(p_{Ti}, p_{Tj})}{p_{Tij}} < z_{\text{cut}} \text{ and } \Delta R_{ij} > \frac{2m_j}{p_{Tj}} R_{\text{cut}}, \quad (4)$$

in which case the merger is vetoed and the softer branch discarded. The default parameters used for pruning [27] in this study are $z_{\text{cut}} = 0.1$ and $R_{\text{cut}} = 0.5$. One advantage of pruning is that the thresholds used to veto soft, wide-angle radiation scale with the jet kinematics, and so the algorithm is expected to perform comparably over a wide range of momenta.

Trimming: Given a jet, re-cluster the constituents into subjets of radius R_{trim} with the k_t algorithm. Discard all subjets i with

$$p_{Ti} < f_{\text{cut}} p_{TJ}. \quad (5)$$

The default parameters used for trimming [28] in this study are $R_{\text{trim}} = 0.2$ and $f_{\text{cut}} = 0.03$.

Filtering: Given a jet, re-cluster the constituents into subjets of radius R_{filt} with the C/A algorithm. Re-define the jet to consist of only the hardest N subjets, where N is determined by the final state topology and is typically one more than the number of hard prongs in the resonance decay (to include the leading final-state gluon emission) [29]. While we do not independently use filtering, it is an important step of the HEPTopTagger to be defined later.

Soft drop: Given a jet, re-cluster all of the constituents using the C/A algorithm. Iteratively undo the last stage of the C/A clustering from j into subjets j_1, j_2 . If

$$\frac{\min(p_{T1}, p_{T2})}{p_{T1} + p_{T2}} < z_{\text{cut}} \left(\frac{\Delta R_{12}}{R} \right)^\beta, \quad (6)$$

166 discard the softer subjet and repeat. Otherwise, take j to be
 167 the final soft-drop jet [30]. Soft drop has two input param-
 168 eters, the angular exponent β and the soft-drop scale z_{cut} , with
 169 default value $z_{\text{cut}} = 0.1$. **ED: Soft-drop actually functions**
 170 **as a tagger when $\beta = -1$**

171 3.3 Jet Tagging Algorithms

Modified Mass Drop Tagger: Given a jet, re-cluster all of
 the constituents using the C/A algorithm. Iteratively undo
 the last stage of the C/A clustering from j into subjets j_1, j_2
 with $m_{j_1} > m_{j_2}$. If either

$$m_{j_1} > \mu m_j \text{ or } \frac{\min(p_{T1}^2, p_{T2}^2)}{m_j^2} \Delta R_{12}^2 < y_{\text{cut}}, \quad (7)$$

172 then discard the branch with the smaller transverse mass
 173 $m_T = \sqrt{m_i^2 + p_{Ti}^2}$, and re-define j as the branch with the
 174 larger transverse mass. Otherwise, the jet is tagged. If de-
 175 clustering continues until only one branch remains, the jet is
 176 untagged [31]. In this study we use by default $\mu = 1.0$ and
 177 $y_{\text{cut}} = 0.1$.

178
 179 **Johns Hopkins Tagger:** Re-cluster the jet using the C/A al-
 180 gorithm. The jet is iteratively de-clustered, and at each step
 181 the softer prong is discarded if its p_T is less than $\delta_p p_{T\text{jet}}$.
 182 This continues until both prongs are harder than the p_T thresh-
 183 old, both prongs are softer than the p_T threshold, or if they
 184 are too close ($|\Delta\eta_{ij}| + |\Delta\phi_{ij}| < \delta_R$); the jet is rejected if ei-
 185 ther of the latter conditions apply. If both are harder than the
 186 p_T threshold, the same procedure is applied to each: this re-
 187 sults in 2, 3, or 4 subjets. If there exist 3 or 4 subjets, then
 188 the jet is accepted: the top candidate is the sum of the sub-
 189 jets, and W candidate is the pair of subjets closest to the W
 190 mass [6]. The output of the tagger is m_t, m_W , and θ_h , a helic-
 191 ity angle defined as the angle, measured in the rest frame of
 192 the W candidate, between the top direction and one of the W
 193 decay products. The two free input parameters of the John
 194 Hopkins tagger in this study are δ_p and δ_R , defined above.

195
 196 **HEPTopTagger:** Re-cluster the jet using the C/A algorithm.
 197 The jet is iteratively de-clustered, and at each step the softer
 198 prong is discarded if $m_1/m_{12} > \mu$ (there is not a significant
 199 mass drop). Otherwise, both prongs are kept. This continues
 200 until a prong has a mass $m_i < m$, at which point it is added to
 201 the list of subjets. Filter the jet using $R_{\text{filt}} = \min(0.3, \Delta R_{ij})$,
 202 keeping the five hardest subjets (where ΔR_{ij} is the distance
 203 between the two hardest subjets). Select the three subjets
 204 whose invariant mass is closest to m_t [5]. The output of the
 205 tagger is m_t, m_W , and θ_h , a helicity angle defined as the an-
 206 gle, measured in the rest frame of the W candidate, between
 207 the top direction and one of the W decay products. The two
 208 free input parameters of the HEPTopTagger in this study are

m and μ , defined above.

Top Tagging with Pruning: For comparison with the other
 top taggers, we add a W reconstruction step to the trimming
 algorithm described above. A W candidate is found as fol-
 lows: if there are two subjets, the highest-mass subjet is the
 W candidate (because the W prongs end up clustered in the
 same subjet); if there are three subjets, the two subjets with
 the smallest invariant mass comprise the W candidate. In the
 case of only one subjet, no W is reconstructed.

Top Tagging with Trimming: For comparison with the other
 top taggers, we add a W reconstruction step to the trimming
 algorithm described above. A W candidate is found as fol-
 lows: if there are two subjets, the highest-mass subjet is the
 W candidate (because the W prongs end up clustered in the
 same subjet); if there are three subjets, the two subjets with
 the smallest invariant mass comprise the W candidate. In the
 case of only one subjet, no W is reconstructed.

3.4 Other Jet Substructure Observables

Qjet mass volatility: As described above, Qjet algorithms
 re-cluster the same jet non-deterministically to obtain a col-
 lection of interpretations of the jet. For each jet interpreta-
 tion, the pruned jet mass is computed with the default prun-
 ing parameters. The mass volatility, Γ_{Qjet} , is defined as [26]

$$\Gamma_{\text{Qjet}} = \frac{\sqrt{\langle m_J^2 \rangle - \langle m_J \rangle^2}}{\langle m_J \rangle}, \quad (8)$$

where averages are computed over the Qjet interpretations.

N -subjettiness: N -subjettiness [32] quantifies how well the
 radiation in the jet is aligned along N directions. To compute
 N -subjettiness, $\tau_N^{(\beta)}$, one must first identify N axes within
 the jet. Then,

$$\tau_N = \frac{1}{d_0} \sum_i p_{Ti} \min(\Delta R_{1i}^\beta, \dots, \Delta R_{Ni}^\beta), \quad (9)$$

where distances are between particles i in the jet and the
 axes,

$$d_0 = \sum_i p_{Ti} R^\beta \quad (10)$$

and R is the jet clustering radius. The exponent β is a free
 parameter. There is also some choice in how the axes used to
 compute N -subjettiness are determined. The optimal config-
 uration of axes is the one that minimizes N -subjettiness; re-
 cently, it was shown that the ‘‘winner-takes-all’’ (WTA) axes

can be easily computed and have superior performance compared to other minimization techniques [33]. We use both the WTA and one-pass k_t optimization axes in our analyses

A more powerful discriminant is often the ratio,

$$\tau_{N,N-1} \equiv \frac{\tau_N}{\tau_{N-1}}. \quad (11)$$

While this is not an infrared-collinear (IRC) safe observable it is calculable [34] and can be made IRC safe with a loose lower cut on τ_{N-1} .

Energy correlation functions: The transverse momentum version of the energy correlation functions are defined as [35]:

$$\text{ECF}(N, \beta) = \sum_{i_1 < i_2 < \dots < i_N \in j} \left(\prod_{a=1}^N p_{T i_a} \right) \left(\prod_{b=1}^{N-1} \prod_{c=b+1}^N \Delta R_{i_b i_c} \right)^{\beta}, \quad (12)$$

where i is a particle inside the jet. It is preferable to work in terms of dimensionless quantities, particularly the energy correlation function double ratio:

$$C_N^{(\beta)} = \frac{\text{ECF}(N+1, \beta) \text{ECF}(N-1, \beta)}{\text{ECF}(N, \beta)^2}. \quad (13)$$

This observable measures higher-order radiation from leading-order substructure.

4 Multivariate Analysis Techniques

Multivariate techniques are used to combine variables into an optimal discriminant. In all cases variables are combined using a boosted decision tree (BDT) as implemented in the TMVA package [36]. We use the BDT implementation including gradient boost. An example of the BDT settings are as follows:

- NTrees=1000
- BoostType=Grad
- Shrinkage=0.1
- UseBaggedGrad=F
- nCuts=10000
- MaxDepth=3
- UseYesNoLeaf=F
- nEventsMin=200

Exact parameter values are chosen to best reduce the effect of overtraining. **ED: Can we describe a bit more the tests we do to ensure that we are not suffering from overtraining?**

5 Quark-Gluon Discrimination

In this section, we examine the differences between quark- and gluon-initiated jets in terms of substructure variables, and to determine to what extent these variables are correlated. Along the way, we provide some theoretical understanding of these observables and their performance. The motivation for these studies comes not only from the desire to “tag” a jet as originating from a quark or gluon, but also to improve our understanding of the quark and gluon components of the QCD backgrounds relative to boosted resonances. While recent studies have suggested that quark/gluon tagging efficiencies depend highly on the Monte Carlo generator used [REF], we are more interested in understanding the scaling performance with p_T and R , and the correlations between observables, which are expected to be treated consistently within a single shower scheme.

5.1 Methodology

These studies use the qq and gg MC samples, described previously in Section 2. The showered events were clustered with FASTJET 3.03 [REF] using the anti- k_T algorithm [REF] with jet radii of $R = 0.4, 0.8, 1.2$. In both signal (quark) and background (gluon) samples, an upper and lower cut on the leading jet p_T is applied after showering/clustering, to ensure similar p_T spectra for signal and background in each p_T bin. The bins in leading jet p_T that are considered are 300-400 GeV, 500-600 GeV, 1.0-1.1 TeV, for the 300-400 GeV, 500-600 GeV, 1.0-1.1 TeV parton p_T slices respectively. Various jet grooming approaches are applied to the jets, as described in Section 3.4. Only leading and subleading jets in each sample are used. The following observables are studied in this section:

- The ungroomed jet mass, m .
- 1-subjettiness, τ_1^β with $\beta = 1, 2$. The N -subjettiness axes are computed using one-pass k_t axis optimization.
- 1-point energy correlation functions, $C_1^{(\beta)}$ with $\beta = 1, 2$.
- The pruned Qjet mass volatility, Γ_{Qjet} .
- The number of constituents (N_{constits}).

5.2 Single Variable Discrimination

Figure 1 shows the mass of jets in the quark and gluon samples when using different groomers, and the ungroomed jet mass, for jets with $R=0.8$ and in the $p_T = 500 - 600$ GeV bin. Qualitatively, the application of grooming shifts the mass distributions towards lower values when compared to the ungroomed mass, as expected. No clear gain in discrimination can be seen, and for certain grooming parameters,

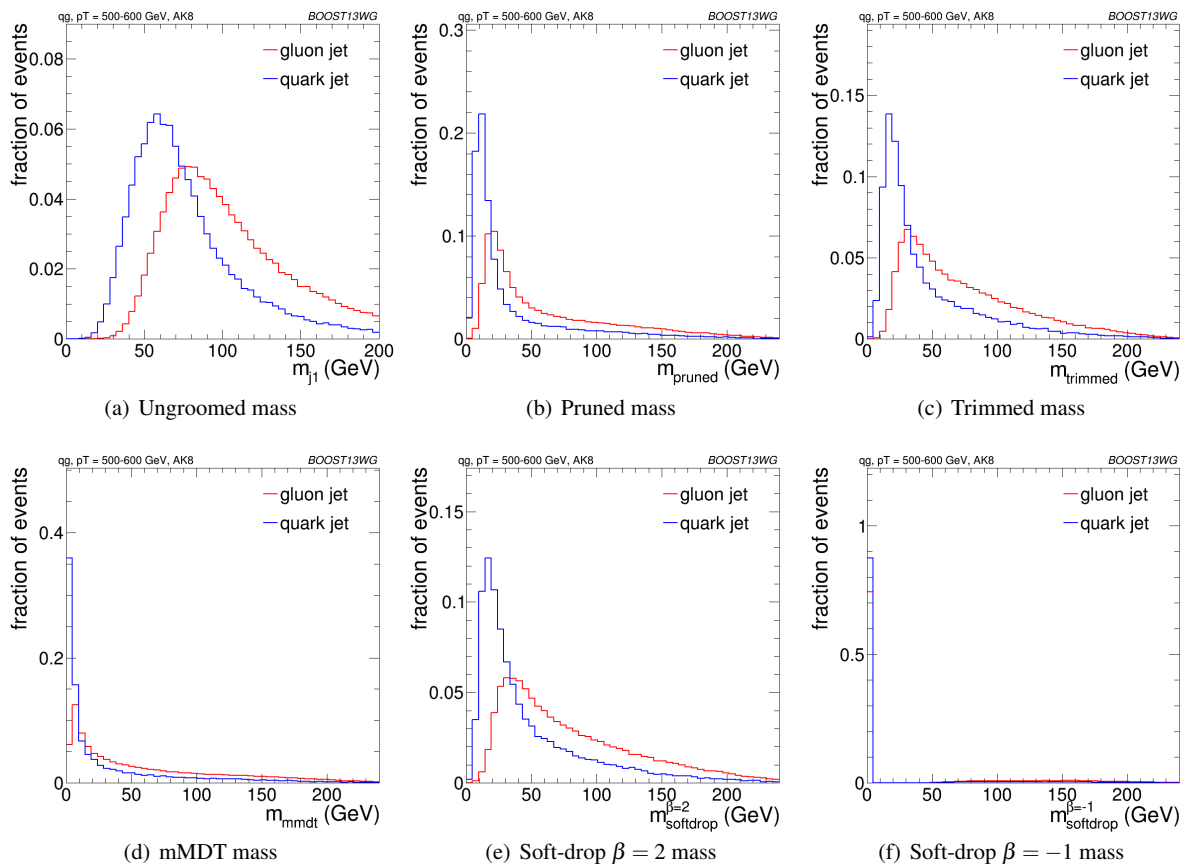


Fig. 1 Comparisons of ungroomed and groomed quark and gluon mass distributions for leading jets in the $p_T = 500 - 600$ GeV bin using the anti- k_T $R=0.8$ algorithm.

309 such as the use of soft drop with $\beta = -1$ a clear loss in dis-331
 310 crimination power is observed; this is because the soft-drop332
 311 condition for $\beta = -1$ discards collinear radiation, and the333
 312 differences between quarks and gluons are manifest in the334
 313 collinear structure (spin, splitting functions, etc.). 335

314 The quark and gluon distributions of different substructure336
 315 variables are shown in Figure 2. Among those consid-337
 316 ered, one can see by eye that n_{constits} provides the highest338
 317 separation power, followed by $C_1^{\beta=0}$ and $C_1^{\beta=1}$, as was also339
 318 found by the CMS and ATLAS Collaborations[REF]. 340

319 To more quantitatively study the power of each observ-342
 320 able as a discriminator for quark/gluon tagging, ROC curves343
 321 are built by scanning each distribution and plotting the back-344
 322 ground efficiency (to select gluon jets) vs. the signal ef-345
 323 ficiency (to select quark jets). Figure 3 shows these ROG346
 324 curves for all of the substructure variables shown in Fig-347
 325 ure 2, along with the ungroomed mass, representing the best348
 326 performing mass variable, for $R=0.4, 0.8$ and 1.2 jets in the349
 327 $p_T = 300 - 400$ GeV bin. In addition, the ROC curve for a350
 328 tagger built from a BDT combination of all the variables (see351
 329 Section 4) is shown. Clearly, n_{constits} is the best performing352
 330 variable for all R s, even though $C_1^{\beta=0}$ is close, particularly353

for $R=0.8$. Most other variables have similar performance, except $T_{Q_{\text{jet}}}$, which shows significantly worse discrimination (this may be due to our choice of rigidity $\alpha = 0.1$, with other studies suggesting that a smaller value, such as $\alpha = 0.01$, produces better results[REF]). The combination of all variables shows somewhat better discrimination.

We now examine how performance of masses and substructure observables changes with p_T and R . For jet masses, few variations are observed as the radius parameter of the jet reconstruction is increased in the two highest p_T bins; this is because the radiation is more collimated and the dependence on R is consequently smaller. However, for the $300 - 400$ GeV bin, the use of small- R jets produces a shift in the mass distributions towards lower values, so that large- R jet masses are more stable with p_T and small- R jet masses are smaller at low- p_T as expected from the spatial constraints imposed by the R parameter. These statements are explored more quantitatively later in this section. **(BS: Do we have plots for this?)**

The evolution of some of the substructure variable distributions with p_T and R is less trivial than for the jet masses. In particular, changing the R parameter at high p_T changes significantly the C_a^β for $\beta > 0$ and the n_{constits} distributions,

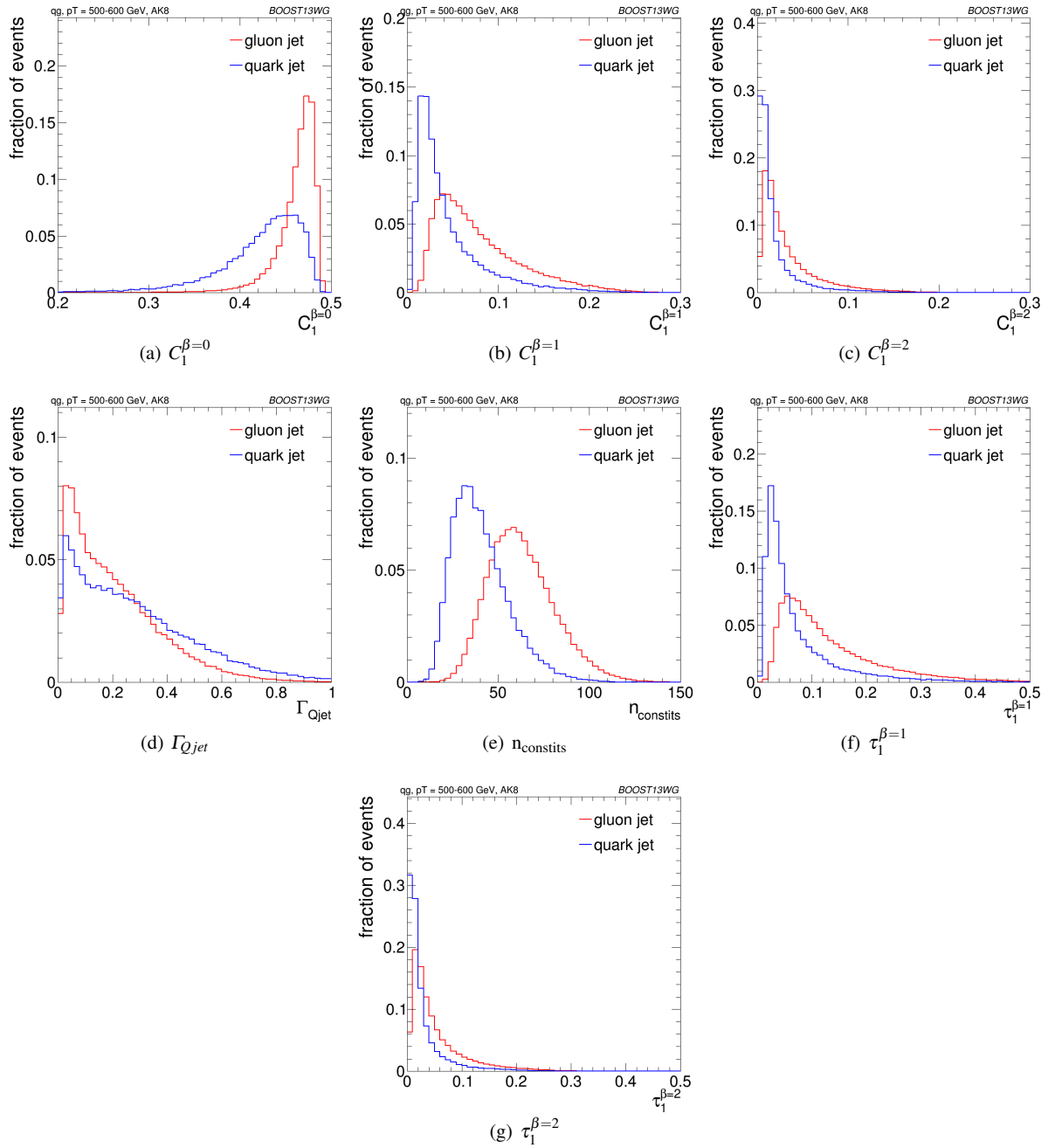


Fig. 2 Comparisons of quark and gluon distributions of different substructure variables for leading jets in the $p_T = 500 - 600$ GeV bin using the anti- k_T $R=0.8$ algorithm.

354 while leaving all other distributions qualitatively unchanged 363
 355 This is illustrated in Figure 4 for $\beta = 0$ and $\beta = 1$ using $a = b$ 364
 356 in both cases for jets with $p_T = 1.0 - 1.1$ TeV. 365

357 The shift towards lower values with changing R is evi- 366
 358 dent for the $C_1^{\beta=1}$ distributions, while the stability of $C_1^{\beta=0}$ 367
 359 can also be observed. These features are present in all p_T 368
 360 bins studied, but are even more pronounced for lower p_T 369
 361 bins. The shape of the Q-jet volatility distribution shows 371
 362 some non-trivial shape that deserves some explanation. Two

peaks are observed, one at low volatility values and one at
 mid-volatility. These peaks are generated by two somewhat
 distinct populations. The high volatility peak arises from jets
 that get their mass primarily from soft (and sometimes wide-
 angle) emissions. The removal of some of the constituents
 when building Q-jets thus changes the mass significantly, in-
 creasing the volatility. The lower volatility peak corresponds
 to jets for which mass is generated by a hard emission, which
 makes the fraction of Q-jets that change the mass signifi-

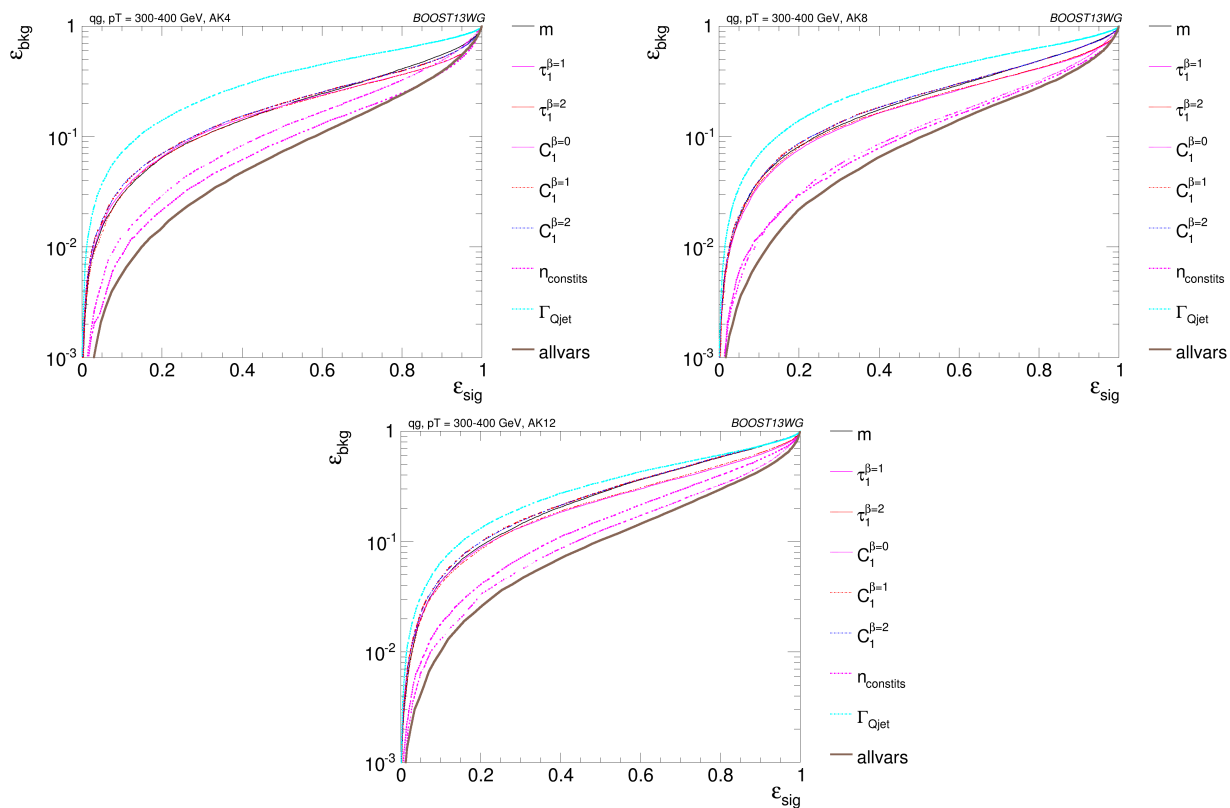


Fig. 3 The ROC curve for all single variables considered for quark-gluon discrimination in the p_T 300-400 GeV bin using the anti- k_T $R=0.4, 0.8$ and 1.2 algorithm. **ED: Hard to tell the lines on the plots apart**

372 cantly to be smaller. Since the probability of a hard emission 395
 373 is proportional to the colour charge (squared), the volatil-396
 374 ity peak is higher for gluon jets by about the colour facto-397
 375 C_A/C_F . 398

376 In summary, the overall discriminating power between 399
 377 quarks and gluons decreases with increasing R due to the 400
 378 reduction in the amount of out-of-cone radiation differences 401
 379 and and increased contamination from the underlying event 402
 380 (**BS: is this ok?**). The broad performance features discussed 403
 381 for this p_T bin also apply to the higher p_T bins. These 404
 382 further quantified in the next section. 405

383 5.3 Combined Performance and Correlations 406

384 The quark/gluon tagging performance can be further im-409
 385 proved over cuts on single observables by combining mul-410
 386 tiple observables in a BDT; due to the challenging nature 411
 387 of q/g -tagging, any improvement in performance with mul-412
 388 tivariable techniques could be critical for certain analyses 413
 389 and the improvement could be more substantial in data than 414
 390 the marginal benefit found in MC and shown in Fig. 3. Fur-415
 391 thermore, insight can be gained into the features allowing fo-416
 392 quark/gluon discrimination if the origin of the improvement 417
 393 is understood. To quantitatively study this improvement, we 418
 394 build quark/gluon taggers from every pair-wise combination 419

of variables studied in the previous section for comparison with the all-variable combination.

In order to quantitatively study the value of each variable for quark/gluon tagging, we study the gluon rejection, defined as $1/\epsilon_{\text{gluon}}$, at a fixed quark selection efficiency of 50% using jets with $p_T = 1 - 1.1$ TeV and for different R parameters. Figure 5 shows the gluon rejection for each pair-wise combination. The pair-wise gluon rejection at 50% quark efficiency can be compared to the single-variable values shown along the diagonal. The gluon rejection for the BDT all-variable combination is also shown on the bottom right of each plot. As already observed in the previous section, n_{constits} is the most powerful single variable and $C_1^{(\beta=0)}$ follows closely. However, the gains are largely correlated; the combined performance of n_{constits} and $C_1^{(\beta=0)}$ is generally poorer than combinations of n_{constits} with other jet substructure observables, such as τ_1 . Interestingly, in spite of the high correlation between n_{constits} and $C_1^{(\beta=0)}$, the two-variable combinations of n_{constits} generally fare worse than two-variable combinations with $C_1^{(\beta=0)}$. In particular, the combinations of $\tau_1^{\beta=1}$ or $C_1^{(\beta=1)}$ with n_{constits} are capable of getting very close to the rejection achievable through the use of all variables for $R = 0.4$ and $R = 0.8$.

Tagger performance is generally better at small R . The overall loss in performance with increasing R can be seen in

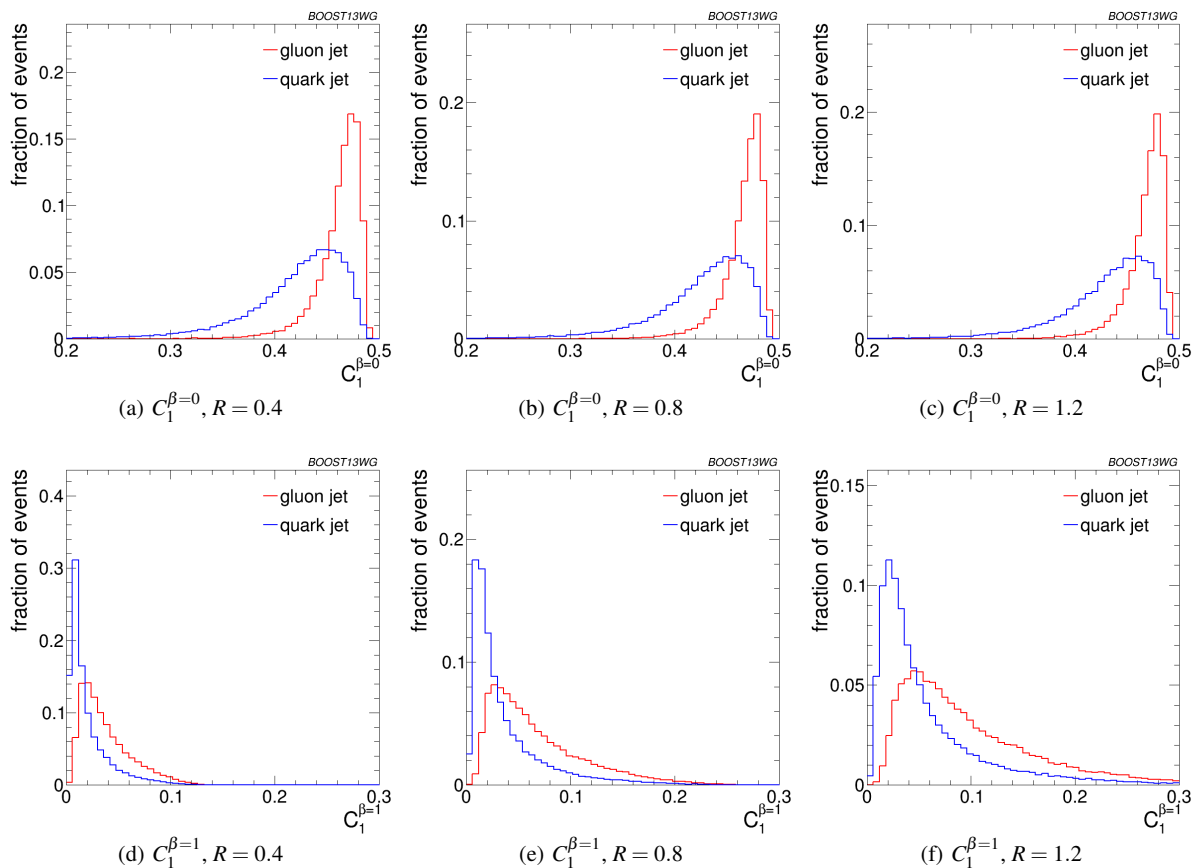


Fig. 4 Comparisons of quark and gluon distributions of $C_1^{\beta=0}$ (top) and $C_1^{\beta=1}$ (bottom) for leading jets in the $p_T = 1 - 1.1$ TeV bin using the anti- k_T algorithm with $R = 0.4, 0.8$ and 1.2 .

420 most single variables we study; this is expected, since more 442
 421 of the parton radiation is captured in the jet and more con- 443
 422 tamination from underlying event occurs, suppressing the 444
 423 differences between q/g jets. The principal exceptions are 445
 424 $C_1^{(\beta=0)}$ and the Q-jet mass volatility, which are both quite 446
 425 resilient to increasing R . For $C_1^{(\beta=0)}$, this is due to the fact 447
 426 that the exponent on ΔR is zero, and so soft radiation at the 448
 427 periphery of the jet does not substantially change the distri- 449
 428 bution; as a result, the performance is largely independent 450
 429 of R . Similarly, the soft radiation distant from the jet cen- 451
 430 tre will be vetoed during pruning regardless of the cluster 452
 431 sequence, and so the R -dependence of I_{Qjet} is not signifi- 453
 432 cant. (BS: Check my logic?) Their combination, however, 454
 433 does perform slightly worse at larger R . (BS: I don't un- 455
 434 derstand this, but it is a $\sim 10\%$ effect, so maybe not too 456
 435 significant?). By contrast, $\tau_1^{(\beta=2)}$ and $C_1^{(\beta=2)}$ are particu- 457
 436 larly sensitive to increasing R since, for $\beta = 2$, large-angle 458
 437 emissions are given a larger weight.

438 These observations are qualitatively similar across all 458
 439 ranges of p_T . Quantitatively, however, there is a loss of re- 459
 440 jection power for the taggers made of a combination of vari- 460
 441 ables as the p_T decreases. This can be observed in Fig. 661

for anti- k_T $R=0.4$ jets of different p_T s. Clearly, most single
 variables retain their gluon rejection potential at lower
 p_T . However, when combined with other variables, the high-
 est performing pairwise combinations lose ground with re-
 spect to other pairwise combinations. This is also reflected
 in the rejection of the tagger that uses a combination of all
 variables, which is lower at lower p_T s. [do we understand
 this?] (BS: This is a bit of a guess, but could it be that
 there is typically less radiation for low p_T , and so you're
 more sensitive to fluctuations; since you have less access
 to information, combinations of observables perform less
 well than at high p_T .)

6 Boosted W -Tagging

In this section, we study the discrimination of a boosted
 hadronically decaying W signal against a gluon background,
 comparing the performance of various groomed jet masses,
 substructure variables, and BDT combinations of groomed
 mass and substructure. We produce ROC curves that elu-
 cidate the performance of the various groomed mass and
 substructure variables. A range of different distance param-

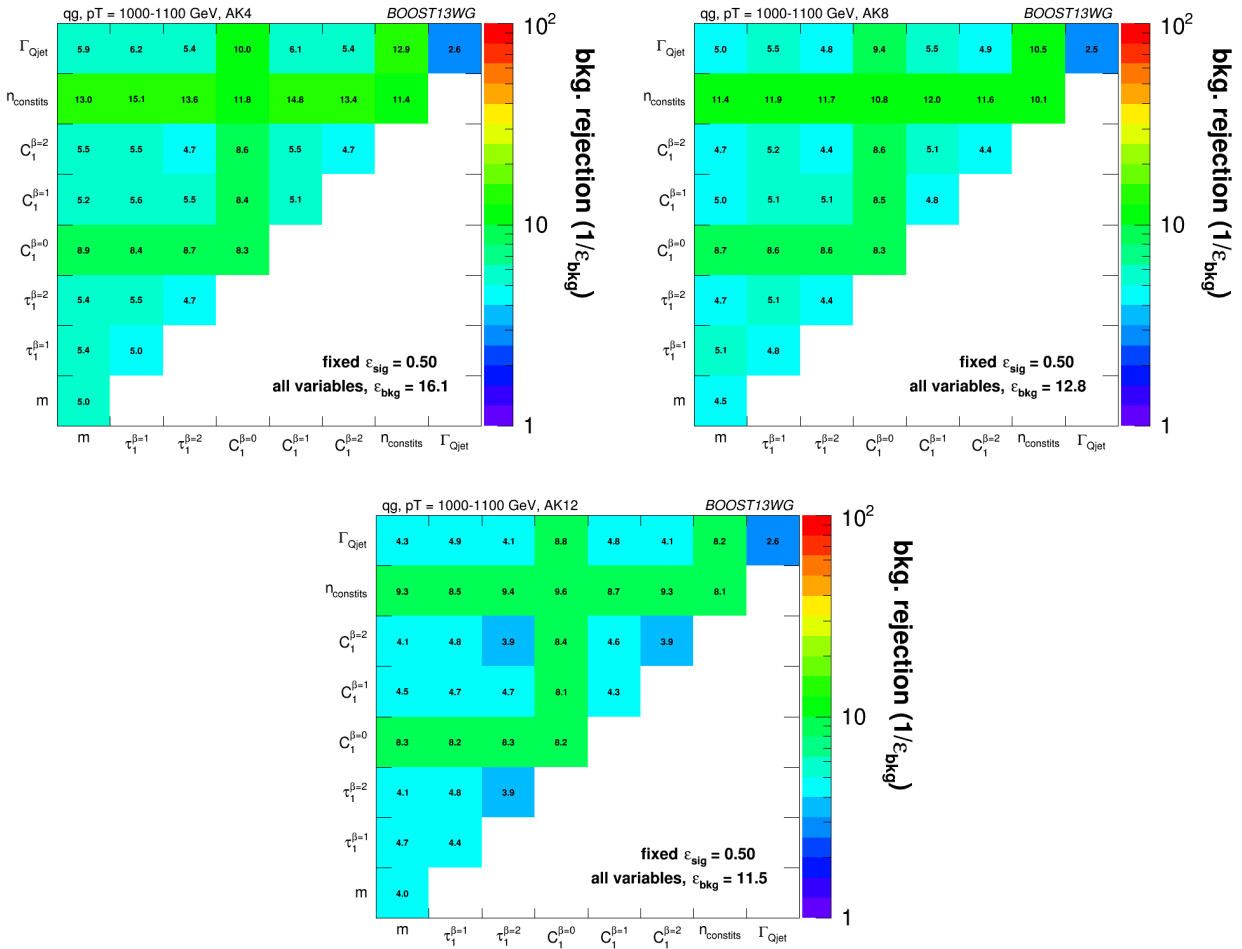


Fig. 5 Gluon rejection defined as $1/\epsilon_{\text{gluon}}$ when using each 2-variable combination as a tagger with 50% acceptance for quark jets. Results are shown for jets with $p_T = 1 - 1.1$ TeV and for (left) $R = 0.4$; (centre) $R = 0.8$; (right) $R = 1.2$. The rejection obtained with a tagger that uses all variables is also shown in the plots.

462 eters R for the anti- k_T jet algorithm are explored, as well as
 463 a variety of kinematic regimes (lead jet p_T 300-400 GeV,
 464 500-600 GeV, 1.0-1.1 TeV). This allows us to determine
 465 the performance of observables as a function of jet radius
 466 and jet boost, and to see where different approaches may
 467 break down. The groomed mass and substructure variables
 468 are then combined in a BDT as described in Section 4, and
 469 the performance of the resulting BDT discriminant explored
 470 through ROC curves to understand the degree to which vari-
 471 ables are correlated, and how this changes with jet boost and
 472 jet radius.

473 6.1 Methodology

474 These studies use the WW samples as signal and the dijet
 475 gg as background, described previously in Section 2. Whilst
 476 only gluonic backgrounds are explored here, the conclusions
 477 as to the dependence of the performance and correlations on

the jet boost and radius have been verified to hold also for
 qq backgrounds. **ED: To be checked!**

As in the q/g tagging studies, the showered events were
 clustered with FASTJET 3.03 using the anti- k_T algorithm
 with jet radii of $R = 0.4, 0.8, 1.2$. In both signal and back-
 ground samples, an upper and lower cut on the leading jet
 p_T is applied after showering/clustering, to ensure similar
 p_T spectra for signal and background in each p_T bin. The
 bins in leading jet p_T that are considered are 300-400 GeV,
 500-600 GeV, 1.0-1.1 TeV, for the 300-400 GeV, 500-600
 GeV, 1.0-1.1 TeV parton p_T slices respectively. The jets then
 have various grooming approaches applied and substructure
 observables reconstructed as described in Section 3.4. The
 substructure observables studied in this section are:

- 488 – The ungroomed, trimmed (m_{trim}), and pruned (m_{prun}) jet
 489 masses.
- 490 – The mass output from the modified mass drop tagger
 491 (m_{mmdt}).
- 492 – The soft drop mass with $\beta = -1, 2$ (m_{sd}).

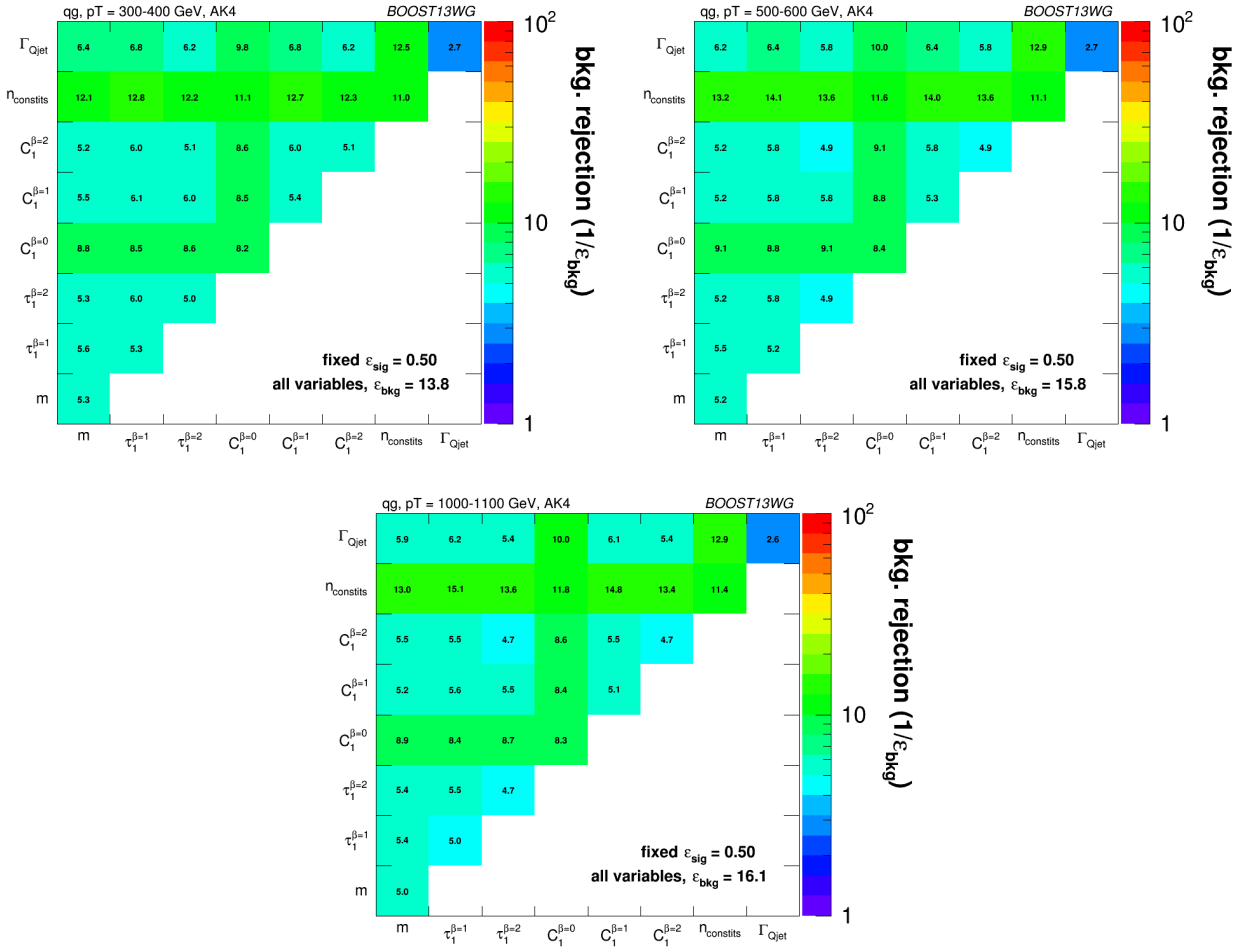


Fig. 6 Gluon rejection defined as $1/\epsilon_{\text{gluon}}$ when using each 2-variable combination as a tagger with 50% acceptance for quark jets. Results are shown for $R=0.4$ jets with $p_T = 300 - 400$ GeV, $p_T = 500 - 600$ GeV and $p_T = 1 - 1.1$ TeV. The rejection obtained with a tagger that uses all variables is also shown in the plots.

- 497 – 2-point energy correlation function ratio $C_2^{\beta=1}$ (we also studied $\beta = 2$ but do not show its results because it showed
- 498 poor discrimination power). 515
- 499 – N -subjettiness ratio τ_2/τ_1 with $\beta = 1$ ($\tau_2^{\beta=1}$) and with 516
- 500 axes computed using one-pass k_t axis optimization (we also studied $\beta = 2$ but did not show its results because it 517
- 501 showed poor discrimination power). 518
- 502 – The pruned Qjet mass volatility, Γ_{Qjet} . 519
- 503 520
- 504 521

505 6.2 Single Variable Performance 523

506 In this section we will explore the performance of the various 525

507 different groomed jet mass and substructure variables in terms 526

508 of discriminating signal and background. Since we have not 527

509 attempted to optimise the grooming parameter settings of 528

510 each grooming algorithm, we do not want to place too much 529

511 emphasis here on the relative performance of the groomed 530

512 masses, but instead concentrate on how their performance 531

changes depending on the kinematic bin and jet radius considered.

Figure 7 compares the signal and background in terms of the different groomed masses explored for the anti- k_T $R=0.8$ algorithm in the p_T 500-600 bin. One can clearly see that in terms of separating signal and background the groomed masses will be significantly more performant than the ungroomed anti- k_T $R=0.8$ mass. Figure 8 compares signal and background in the different substructure variables explored for the same jet radius and kinematic bin.

Figures 9, 10 and 11 show the single variable ROC curves compared to the ROC curve for a BDT combination of all the variables (labelled “allvars”), for each of the anti- k_T distance parameters considered in each of the kinematic bins. One can see that, in all cases, the “allvars” option is considerably better performant than any of the individual single variables considered, indicating that there is considerable complementarity between the variables, and this will be explored further in the next section.

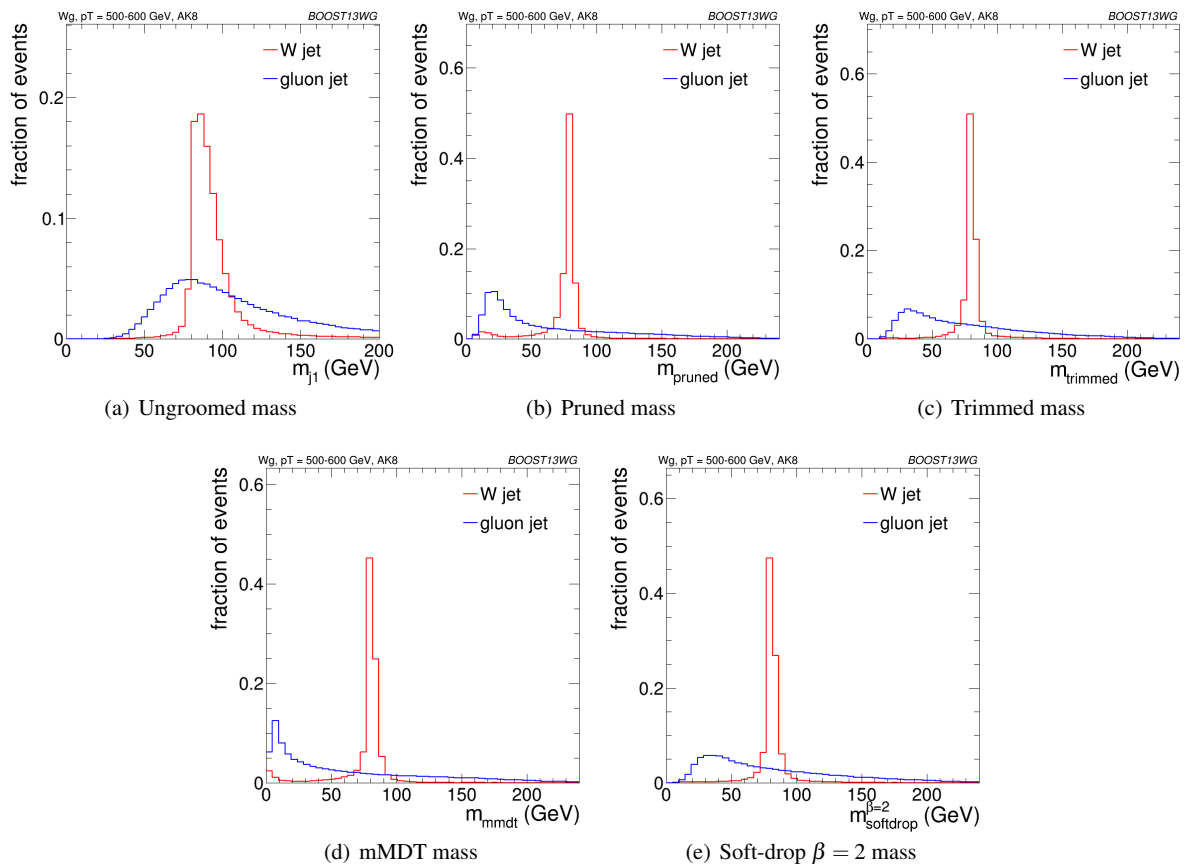


Fig. 7 Comparisons of the QCD background to the WW signal in the p_T 500-600 GeV bin using the anti- k_T $R=0.8$ algorithm: leading jet mass distributions.

532 Although the ROC curves give all the relevant informa-555
 533 tion, it is hard to compare performance quantitatively. In 556
 534 Figures 12, 13 and 14 are shown matrices which give the 557
 535 background rejection for a signal efficiency of 70% when 558
 536 two variables (that on the x-axis and that on the y-axis) are 559
 537 combined in a BDT. These are shown separately for each 560
 538 p_T bin and jet radius considered. In the final column of 561
 539 these plots are shown the background rejection performance 562
 540 for three-variable BDT combinations of $m_{sd}^{\beta=2} + C_2^{\beta=1} + X$ 563
 541 These results will be discussed later in Section 6.3.3. The 564
 542 diagonal of these plots correspond to the background rejec- 565
 543 tions for a single variable BDT, and can thus be examined to 566
 544 get a quantitative measure of the individual single variable 567
 545 performance, and to study how this changes with jet radius 568
 546 and momenta. 569

547 One can see that in general the most performant single 570
 548 variables are the groomed masses. However, in certain kine- 571
 549 matic bins and for certain jet radii, $C_2^{\beta=1}$ has a background 572
 550 rejection that is comparable to or better than the groomed 573
 551 masses. 574

552 By comparing Figures 12(a), 13(a) and 14(b), we can see 575
 553 how the background rejection performance evolves as we in- 576
 554 crease momenta whilst keeping the jet radius fixed to $R=0.8$ 577

Similarly, by comparing Figures 12(b), 13(b) and 14(c) we
 can see how performance evolves with p_T for $R=1.2$. For
 both $R=0.8$ and $R=1.2$ the background rejection power of the
 groomed masses increases with increasing p_T , with a factor
 1.5-2.5 increase in rejection in going from the 300-400 GeV
 to 1.0-1.1 TeV bins. **ED: Add some of the 1-D plots com-
 paring signal and bkgd in the different masses and p_T
 bins here?** However, the $C_2^{\beta=1}$, Γ_{Qjet} and $\tau_{21}^{\beta=1}$ substructure
 variables behave somewhat differently. The background re-
 jection power of the Γ_{Qjet} and $\tau_{21}^{\beta=1}$ variables both decrease
 with increasing p_T , by up to a factor two in going from
 the 300-400 GeV to 1.0-1.1 TeV bins. Conversely the rejec-
 tion power of $C_2^{\beta=1}$ dramatically increases with increasing
 p_T for $R=0.8$, but does not improve with p_T for the larger
 jet radius $R=1.2$. **ED: Can we explain this? Again, should
 we add some of the 1-D plots?**

By comparing the individual sub-figures of Figures 12, 13
 and 14 we can see how the background rejection perfor-
 mance depends on jet radius within the same p_T bin. To
 within $\sim 25\%$, the background rejection power of the groomed
 masses remains constant with respect to the jet radius. How-
 ever, we again see rather different behaviour for the sub-
 structure variables. In all p_T bins considered the most per-

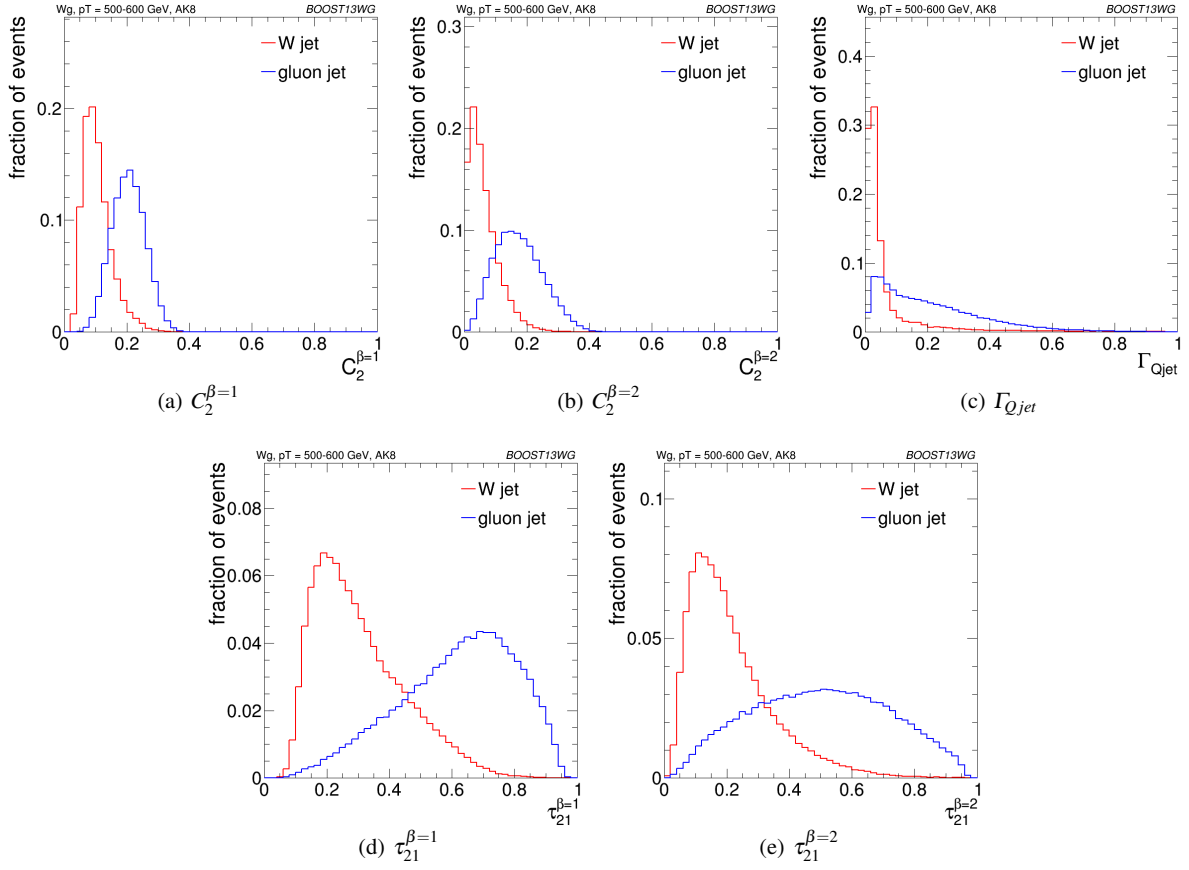


Fig. 8 Comparisons of the QCD background to the WW signal in the p_T 500-600 GeV bin using the anti- k_T R=0.8 algorithm: substructure variables.

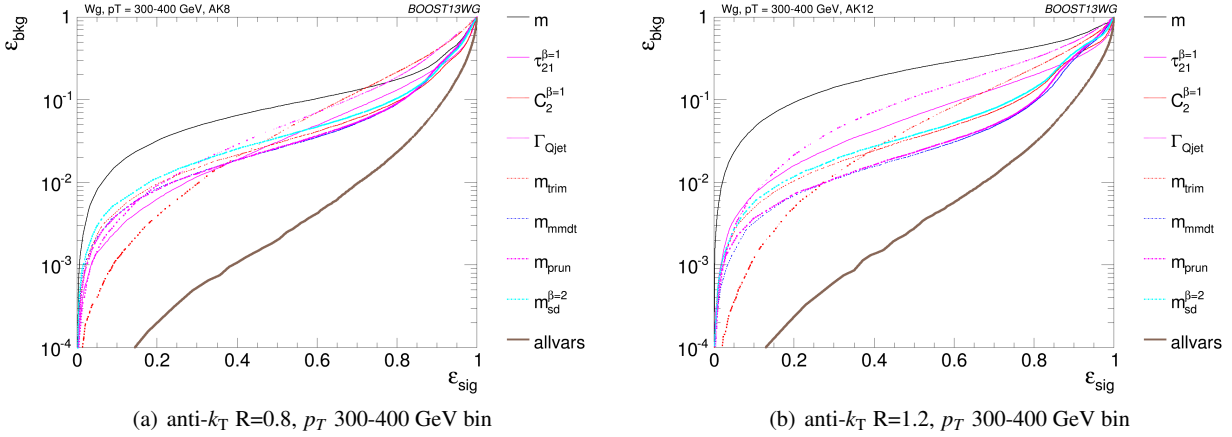


Fig. 9 The ROC curve for all single variables considered for W tagging in the p_T 300-400 GeV bin using the anti- k_T R=0.8 algorithm and R=1.2 algorithm.

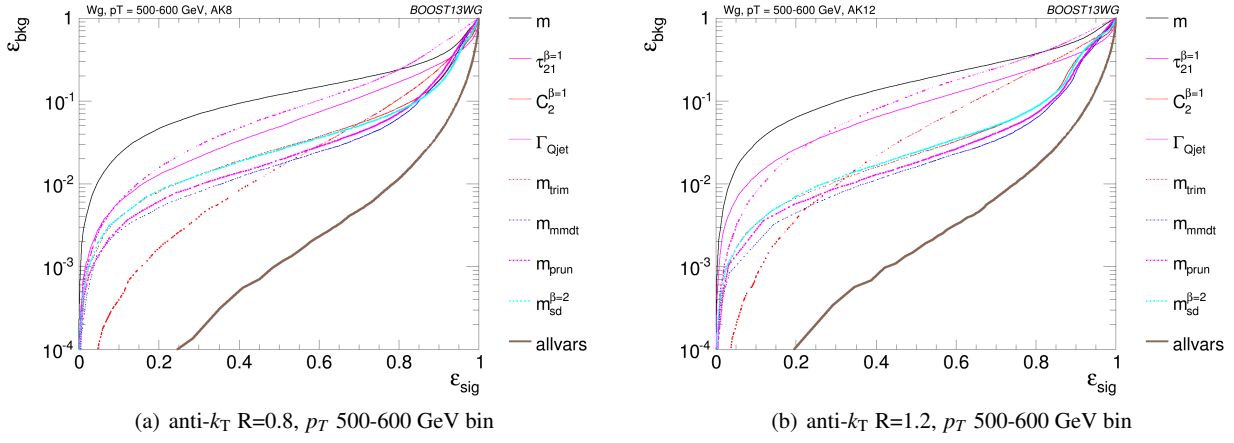


Fig. 10 The ROC curve for all single variables considered for W tagging in the p_T 500-600 GeV bin using the anti- k_T $R=0.8$ algorithm and $R=1.2$ algorithm.

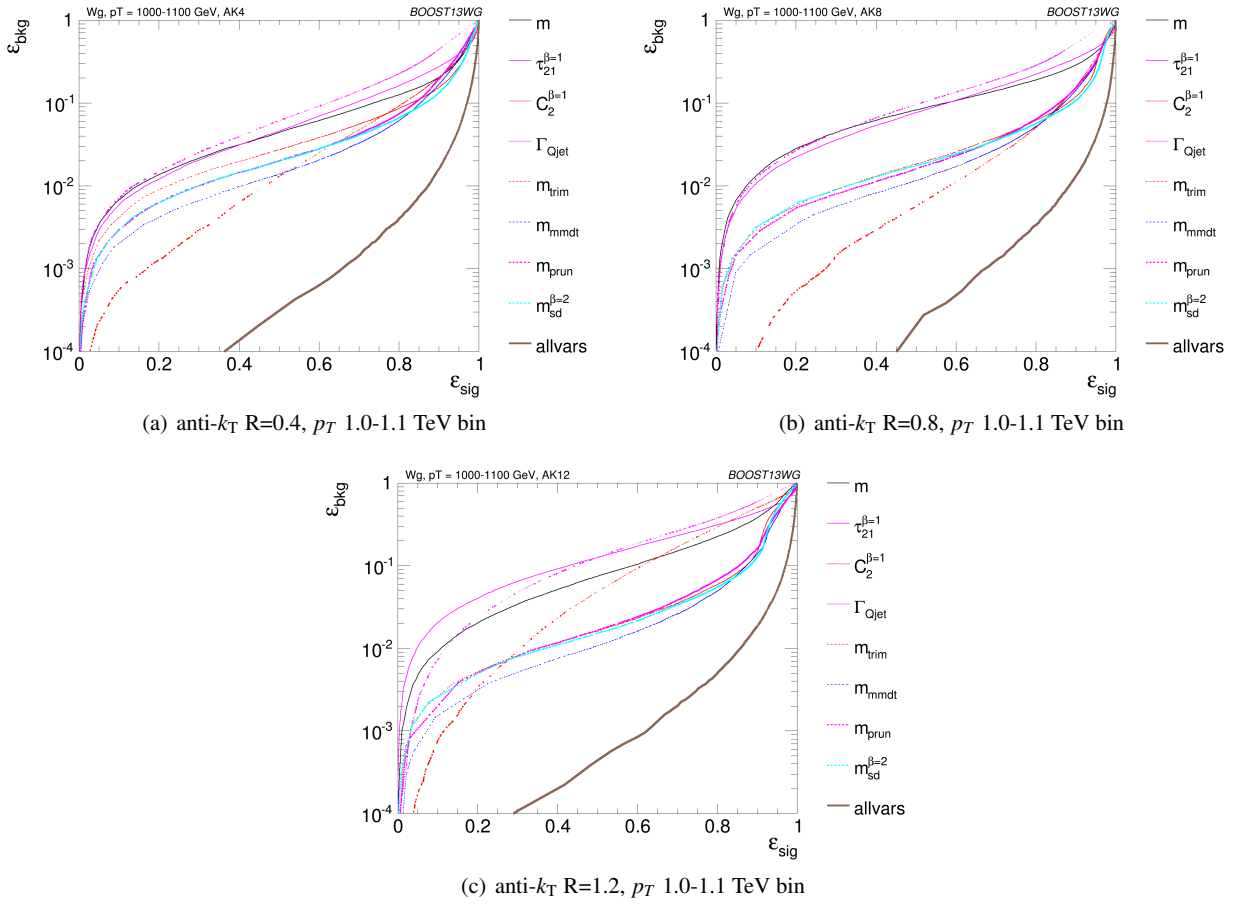


Fig. 11 The ROC curve for all single variables considered for W tagging in the p_T 1.0-1.1 TeV bin using the anti- k_T $R=0.4$ algorithm, anti- k_T $R=0.8$ algorithm and $R=1.2$ algorithm.

formant substructure variable, $C_2^{\beta=1}$, performs best for anti- k_T distance parameter of $R=0.8$. The performance of this variable is dramatically worse for the larger jet radius of $R=1.2$ (a factor seven worse background rejection in the 1.0-1.1 TeV bin), and substantially worse for $R=0.4$. For other jet substructure variables considered, Γ_{Qjet} and $\tau_{21}^{\beta=1}$ their background rejection power also reduces for larger jet radius, but not to the same extent. **ED: Insert some nice discussion/explanation of why jet substructure power generally gets worse as we go to large jet radius, but groomed mass performance does not. Probably need the 1-D figures for this.**

6.3 Combined Performance

The off-diagonal entries in Figures 12, 13 and 14 can be used to compare the performance of different BDT two-variable combinations, and see how this varies as a function of p_T and R . By comparing the background rejection achieved for the two-variable combinations to the background rejection of the ‘‘all variables’’ BDT, one can understand how much more discrimination is possible by adding further variables to the two-variable BDTs.

One can see that in general the most powerful two-variable combinations involve a groomed mass and a non-mass substructure variable ($C_2^{\beta=1}$, Γ_{Qjet} or $\tau_{21}^{\beta=1}$). Two-variable combinations of the substructure variables are not powerful in comparison. Which particular mass + substructure variable combination is the most powerful depends strongly on the p_T and R of the jet, as discussed in the sections that follow.

There is also modest improvement in the background rejection when different groomed masses are combined, compared to the single variable groomed mass performance, indicating that there is complementary information between the different groomed masses. In addition, there is an improvement in the background rejection when the groomed masses are combined with the ungroomed mass, indicating that grooming removes some useful discriminatory information from the jet. These observations are explored further in the section below.

Generally one can see that the $R=0.8$ jets offer the best two-variable combined performance in all p_T bins explored here. This is despite the fact that in the highest 1.0-1.1 GeV p_T bin the average separation of the quarks from the W decay is much smaller than 0.8, and well within 0.4. This conclusion could of course be susceptible to pile-up, which is not considered in this study.

6.3.1 Mass + Substructure Performance

As already noted, the largest background rejection at 70% signal efficiency are in general achieved using those two

variable BDT combinations which involve a groomed mass and a non-mass substructure variable. For both $R=0.8$ and $R=1.2$ jets, the rejection power of these two variable combinations increases substantially with increasing p_T , at least within the p_T range considered here.

For a jet radius of $R=0.8$, across the full p_T range considered, the groomed mass + substructure variable combinations with the largest background rejection are those which involve $C_2^{\beta=1}$. For example, in combination with $m_{sd}^{\beta=2}$, this produces a five-, eight- and fifteen-fold increase in background rejection compared to using the groomed mass alone. In Figure 15 the low degree of correlation between $m_{sd}^{\beta=2}$ versus $C_2^{\beta=1}$ that leads to these large improvements in background rejection can be seen. One can also see that what little correlation exists is rather non-linear in nature, changing from a negative to a positive correlation as a function of the groomed mass, something which helps to improve the background rejection in the region of the W mass peak.

However, when we switch to a jet radius of $R=1.2$ the picture for $C_2^{\beta=1}$ combinations changes dramatically. These become significantly less powerful, and the most powerful variable in groomed mass combinations becomes $\tau_{21}^{\beta=1}$ for all jet p_T considered. Figure 16 shows the correlation between $m_{sd}^{\beta=2}$ and $C_2^{\beta=1}$ in the p_T 1.0 - 1.2 TeV bin for the various jet radii considered. Figure 17 is the equivalent set of distributions for $m_{sd}^{\beta=2}$ and $\tau_{21}^{\beta=1}$. One can see from Figure 16 that, due to the sensitivity of the observable to soft, wide-angle radiation, as the jet radius increases $C_2^{\beta=1}$ increases and becomes more and more smeared out for both signal and background, leading to worse discrimination power. This does not happen to the same extent for $\tau_{21}^{\beta=1}$. We can see from Figure 17 that the negative correlation between $m_{sd}^{\beta=2}$ and $\tau_{21}^{\beta=1}$ that is clearly visible for $R=0.4$ decreases for larger jet radius, such that the groomed mass and substructure variable are far less correlated and $\tau_{21}^{\beta=1}$ offers improved discrimination within a $m_{sd}^{\beta=2}$ mass window.

6.3.2 Mass + Mass Performance

The different groomed masses and the ungroomed mass are of course not fully correlated, and thus one can always see some kind of improvement in the background rejection (relative to the single mass performance) when two different mass variables are combined in the BDT. However, in some cases the improvement can be dramatic, particularly at higher p_T , and particularly for combinations with the ungroomed mass. For example, in Figure 14 we can see that in the p_T 1.0-1.1 TeV bin the combination of pruned mass with ungroomed mass produces a greater than eight-fold improvement in the background rejection for $R=0.4$ jets, a greater than five-fold improvement for $R=0.8$ jets, and a factor \sim two improvement for $R=1.2$ jets. A similar behaviour can be seen

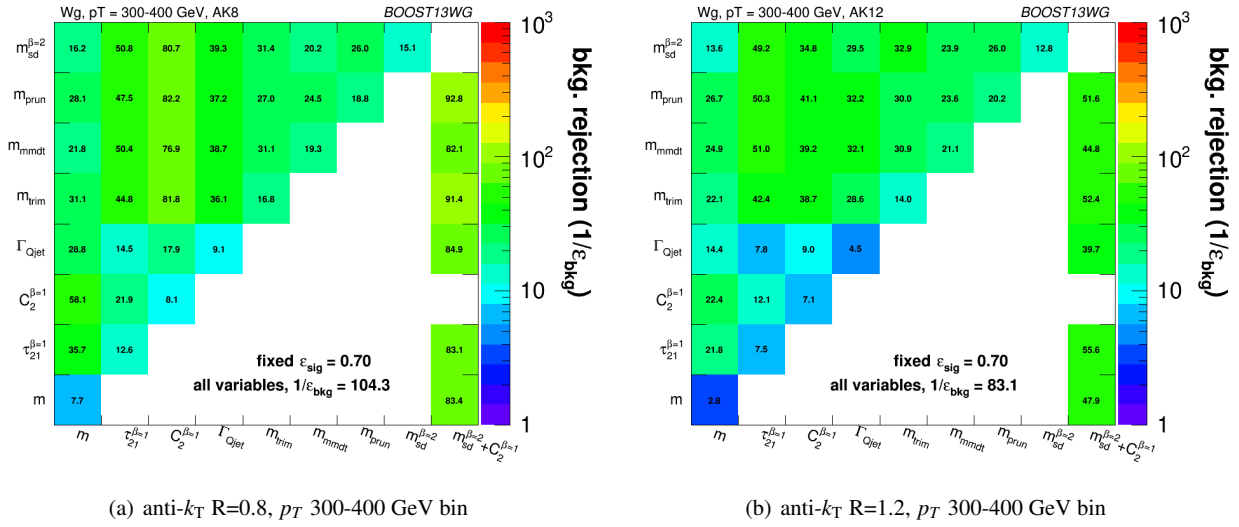


Fig. 12 The background rejection for a fixed signal efficiency (70%) of each BDT combination of each pair of variables considered, in the p_T 300-400 GeV bin using the anti- k_T $R=0.8$ algorithm and $R=1.2$ algorithm. Also shown is the background rejection for a BDT combination of all of the variables considered.

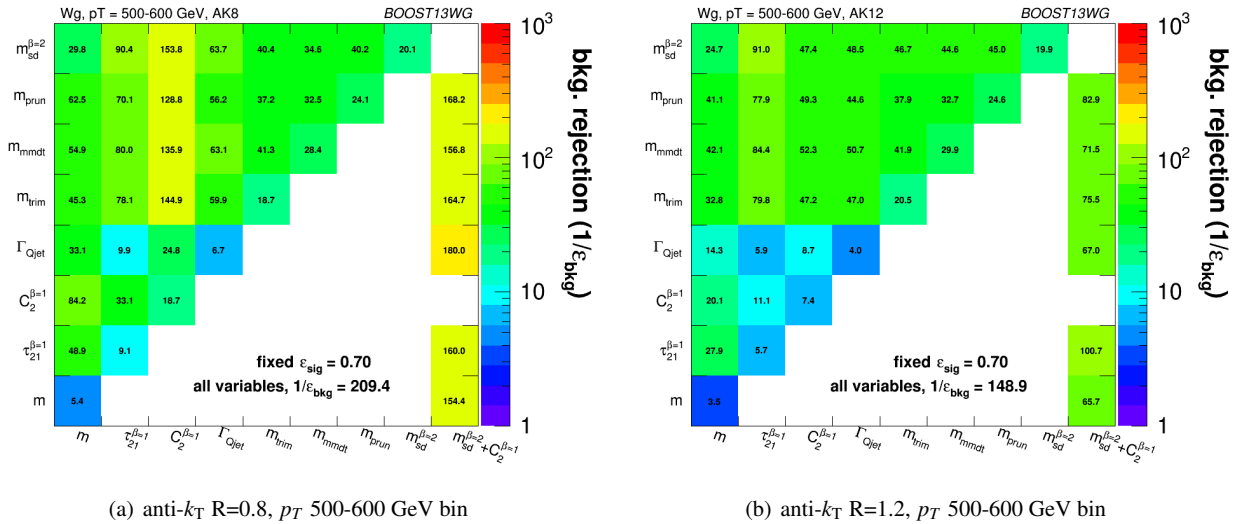


Fig. 13 The background rejection for a fixed signal efficiency (70%) of each BDT combination of each pair of variables considered, in the p_T 500-600 GeV bin using the anti- k_T $R=0.8$ algorithm and $R=1.2$ algorithm. Also shown is the background rejection for a BDT combination of all of the variables considered.

676 for mMDT mass. In Figures 18, 19 and 20 is shown the 2-D₈₈
 677 correlation plots of the pruned mass versus the ungroomed₈₉
 678 mass separately for the WW signal and gg background sam₉₀
 679 ples in the p_T 1.0-1.1 TeV bin, for the various jet radii₉₁
 680 considered. For comparison, the correlation of the trimmed₉₂
 681 mass with the ungroomed mass, a combination that does not₉₃
 682 improve on the single mass as dramatically, is shown. In all₉₄
 683 cases one can see that there is a much smaller degree of cor₉₅
 684 relation between the pruned mass and the ungroomed mass₉₆
 685 in the backgrounds sample than for the trimmed mass and₉₇
 686 the ungroomed mass. This is most obvious in Figure 18₉₈
 687 where the high degree of correlation between the trimmed₉₉

and ungroomed mass is expected, since with the parameters
 used (in particular $R_{trim} = 0.2$) we cannot expect trimming
 to have a significant impact on an $R=0.4$ jet. The reduced
 correlation with ungroomed mass for pruning in the back-
 ground means that, once we have made the requirement that
 the pruned mass is consistent with a W (i.e. ~ 80 GeV), a
 relatively large difference between signal and background
 in the ungroomed mass still remains, and can be exploited
 to improve the background rejection further. In other words,
 many of the background events which pass the pruned mass
 requirement do so because they are shifted to lower mass (to
 be within a signal mass window) by the grooming, but these

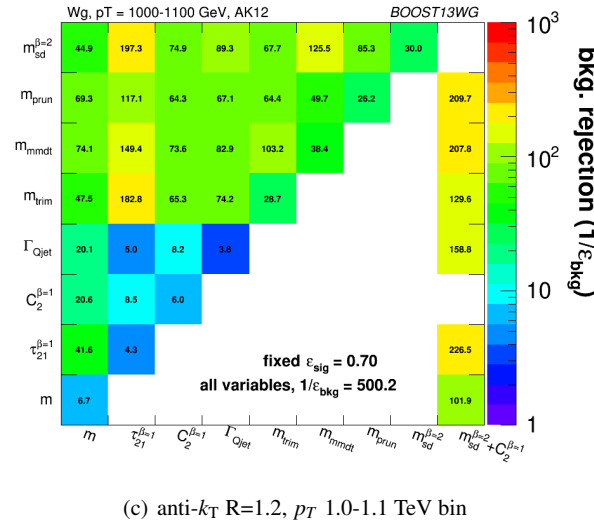
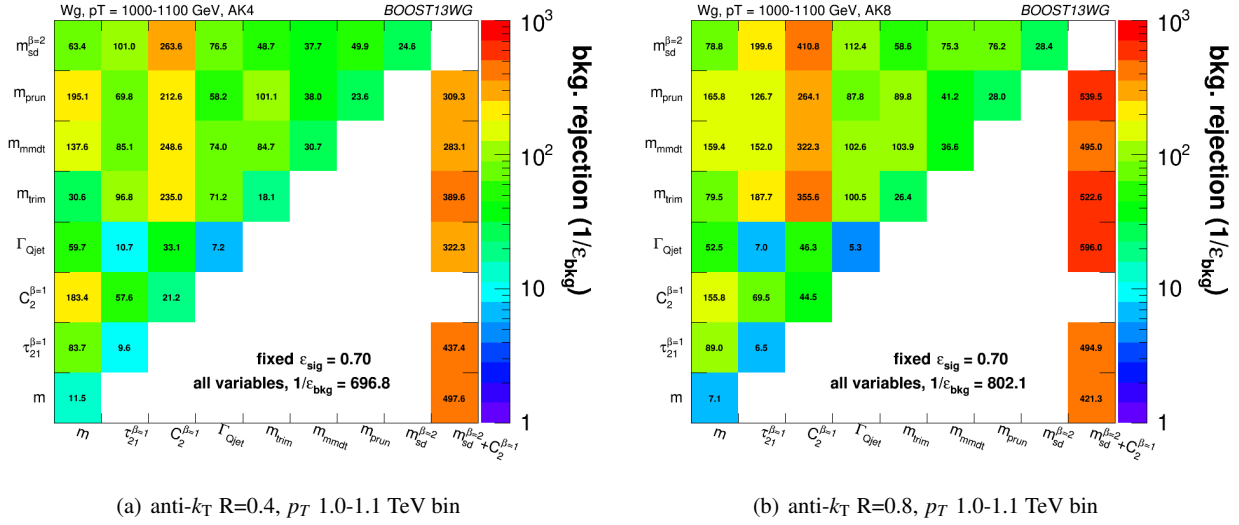


Fig. 14 The background rejection for a fixed signal efficiency (70%) of each BDT combination of each pair of variables considered, in the p_T 1.0-1.1 TeV bin using the anti- k_T $R=0.4$, $R=0.8$ and $R=1.2$ algorithm. Also shown is the background rejection for a BDT combination of all of the variables considered.

700 events still have the property that they look very much like
 701 background events before the grooming. A single require
 702 ment on the groomed mass only does not exploit this. Of
 703 course, the impact of pile-up, not considered in this study
 704 could significantly limit the degree to which the ungroomed
 705 mass could be used to improve discrimination in this way.

706 6.3.3 “All Variables” Performance

707 As well as the background rejection at a fixed 70% sig-
 708 nal efficiency for two-variable combinations, Figures 12, 13
 709 and 14 also report the background rejection achieved by
 710 a combination of all the variables considered into a single
 711 BDT discriminant. One can see that, in all cases, the re-
 712 jection power of this “all variables” BDT is significantly
 713 larger than the best two-variable combination. This indicate

that beyond the best two-variable combination there is still
 significant complementary information available in the re-
 maining variables in order to improve the discrimination of
 signal and background. How much complementary informa-
 tion is available appears to be p_T dependent. In the lower p_T
 300-400 and 500-600 GeV bins the background rejection of
 the “all variables” combination is a factor ~ 1.5 greater than
 the best two-variable combination, but in the highest p_T bin
 it is a factor ~ 2.5 greater.

The final column in Figures 12, 13 and 14 allows us
 to explore the all variables performance a little further. It
 shows the background rejection for three variable BDT com-
 binations of $m_{sd}^{\beta=2} + C_2^{\beta=1} + X$, where X is the variable on
 the y-axis. For jets with $R=0.4$ and $R=0.8$, the combination
 $m_{sd}^{\beta=2} + C_2^{\beta=1}$ is the best performant (or very close to the best

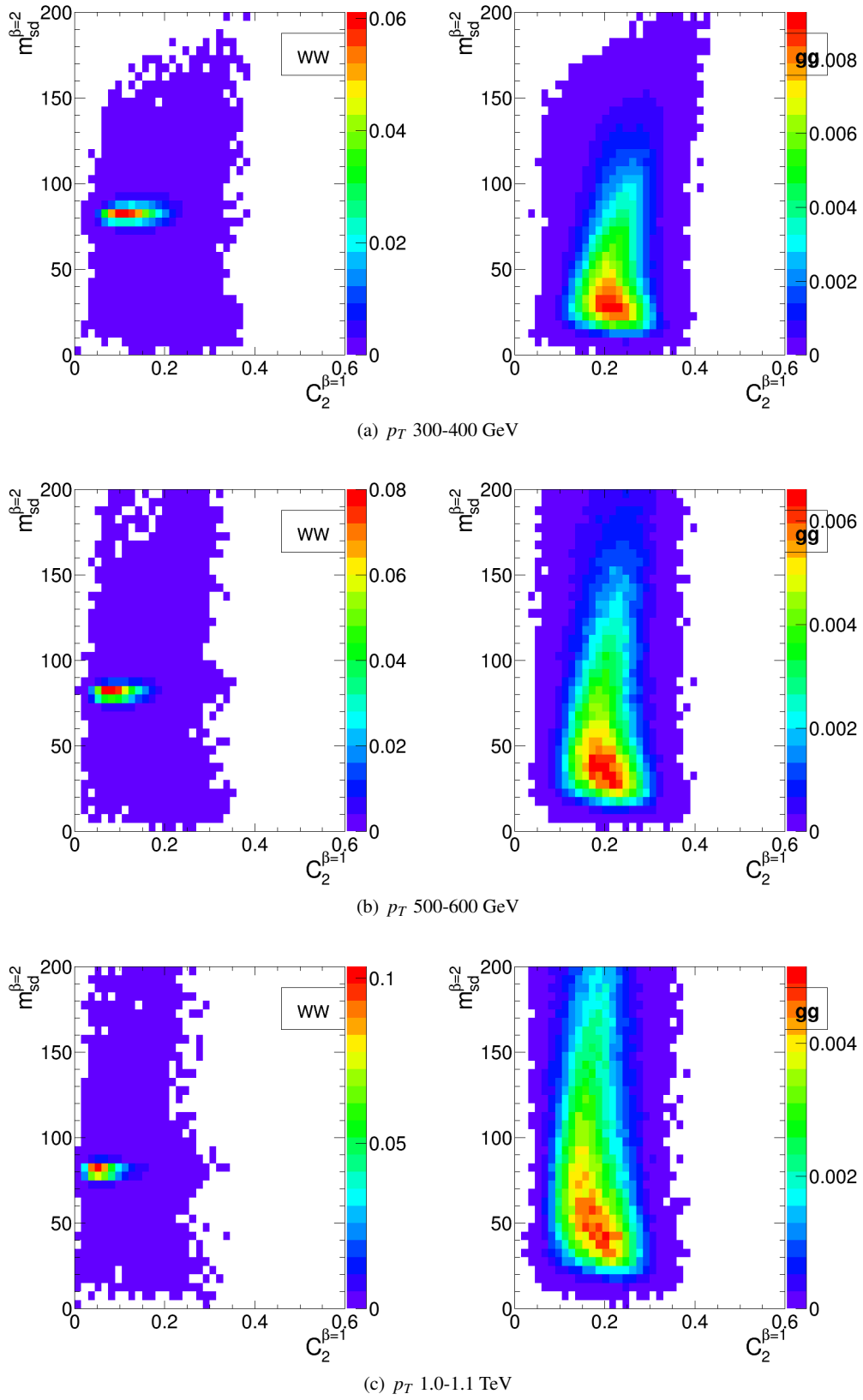


Fig. 15 2-D plots showing $m_{sd}^{\beta=2}$ versus $C_2^{\beta=1}$ for $R=0.8$ jets in the various p_T bins considered.

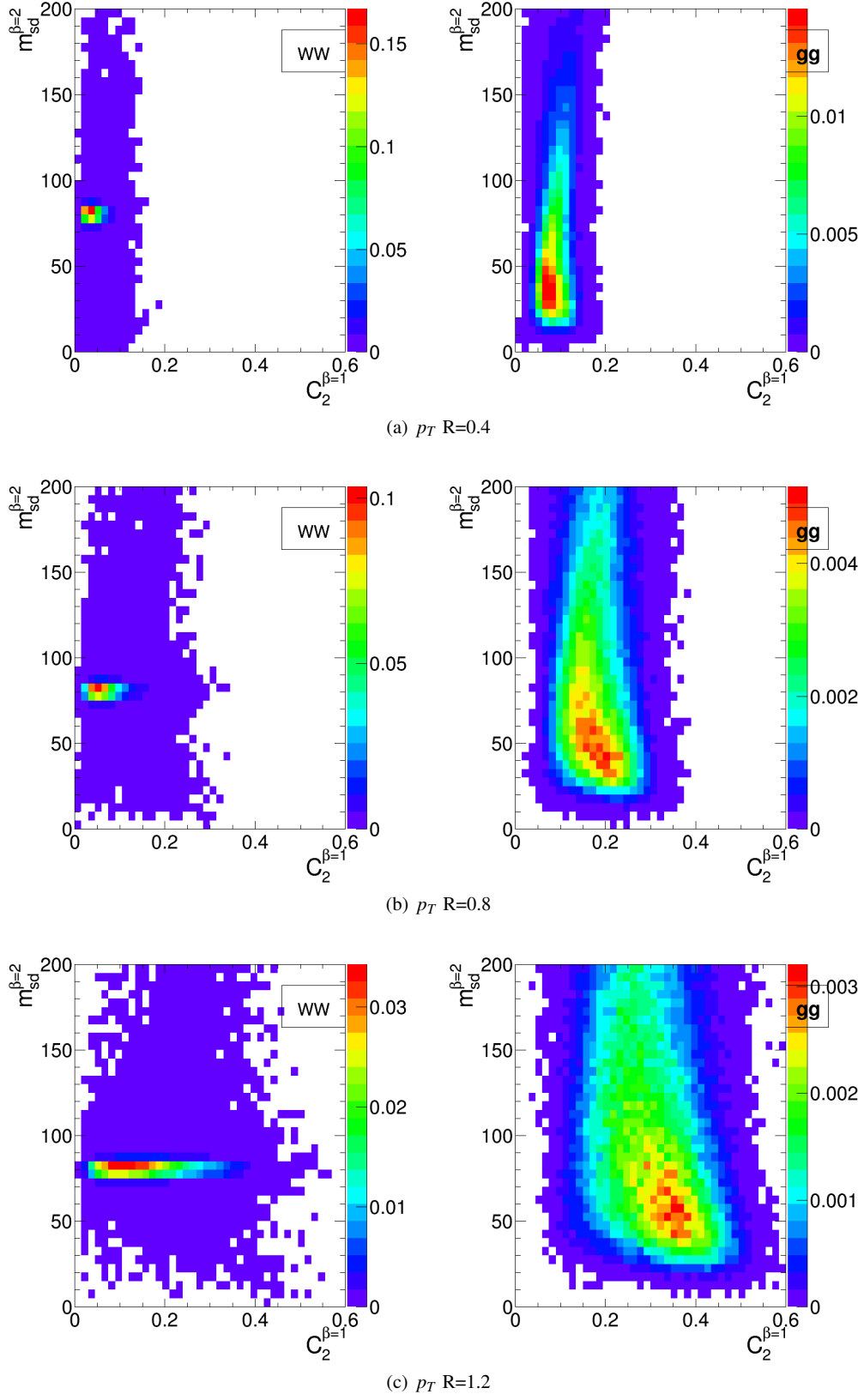


Fig. 16 2-D plots showing $m_{sd}^{\beta=2}$ versus $C_2^{\beta=1}$ for $R=0.4, 0.8$ and 1.2 jets in the p_T 1.0-1.1 TeV bin.

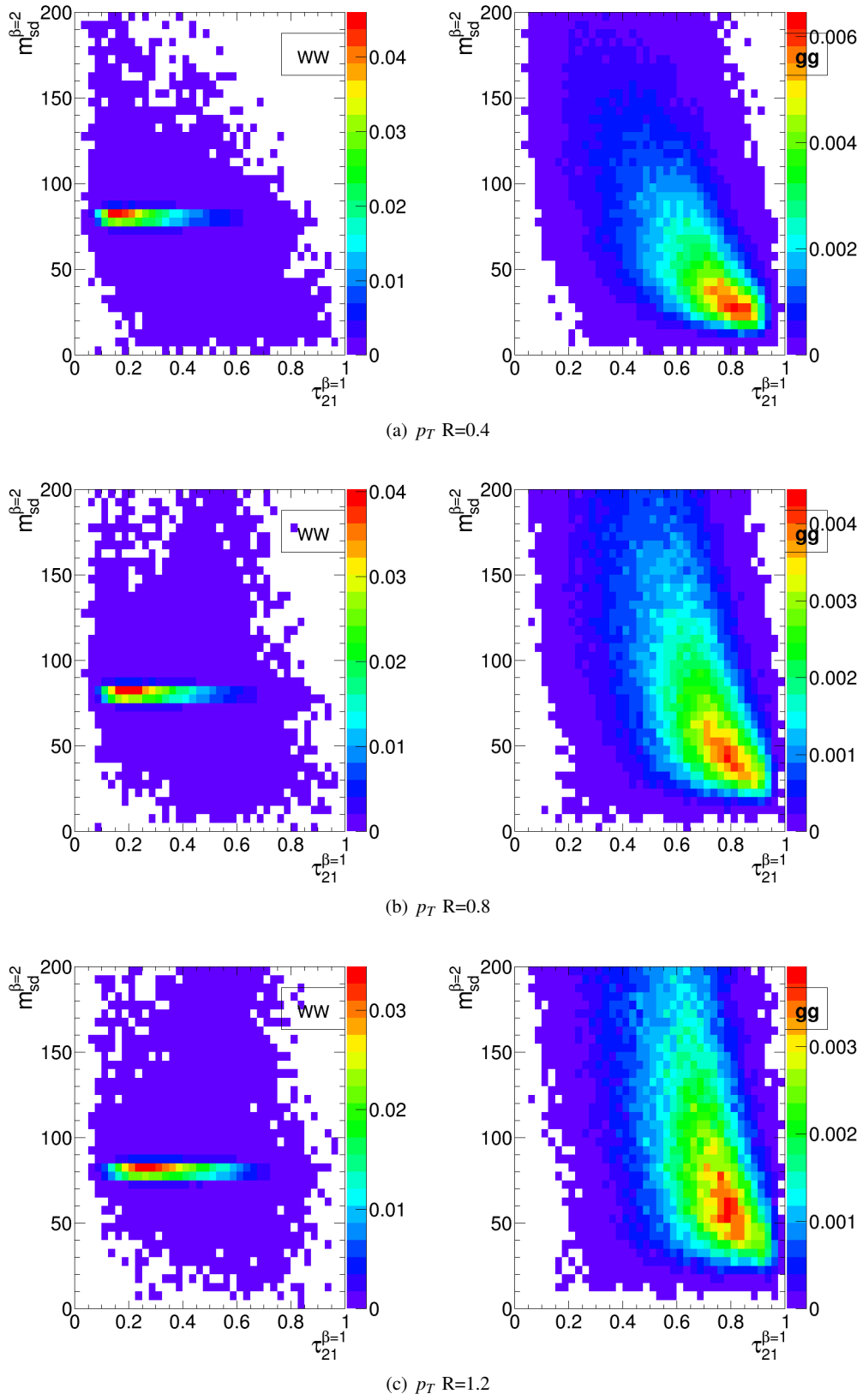


Fig. 17 2-D plots showing $m_{sd}^{\beta=2}$ versus $\tau_{21}^{\beta=1}$ for $R=0.4, 0.8$ and 1.2 jets in the p_T 1.0-1.1 TeV bin.

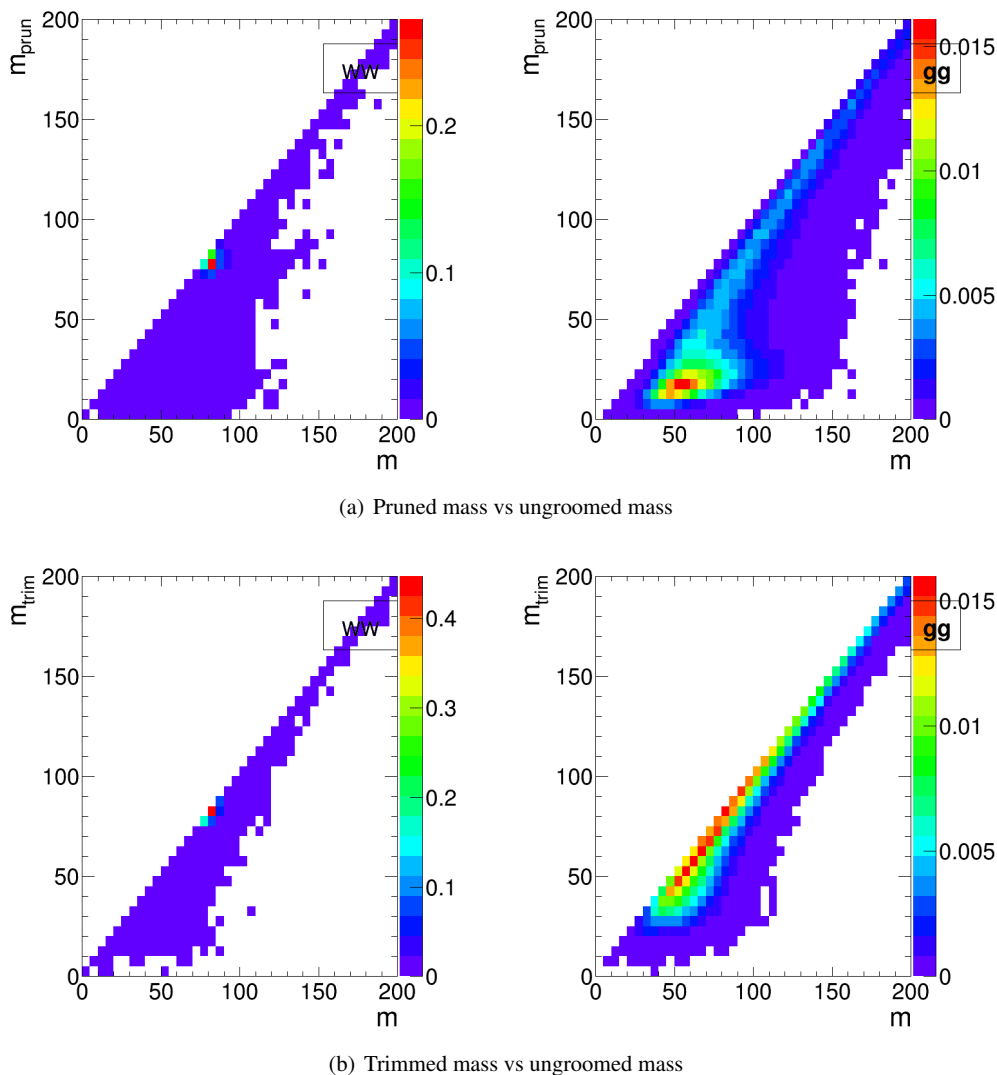


Fig. 18 2-D plots showing the correlation between groomed and ungroomed mass for WW and gg events in the p_T 1.0-1.1 TeV bin using the anti- k_T $R=0.4$ algorithm.

performant) two-variable combination in every p_T bin considered. For $R=1.2$ this is not the case, as $C_2^{\beta=1}$ is superseded by $\tau_{21}^{\beta=1}$ in performance, as discussed earlier. Thus, in considering the three-variable combination results it is best to focus on the $R=0.4$ and $R=0.8$ cases. Here we see that, for the lower p_T 300-400 and 500-600 GeV bins, adding the third variable to the best two-variable combination brings us to within $\sim 15\%$ of the “all variables” background rejection. However, in the highest p_T 1.0-1.1 TeV bin, whilst adding the third variable does improve the performance considerably, we are still $\sim 40\%$ from the observed “all variables” background rejection, and clearly adding a fourth or maybe even fifth variable would bring considerable gains. In terms of which variable offers the best improvement when added to the $m_{sd}^{\beta=2} + C_2^{\beta=1}$ combination, it is hard to see an obvious

pattern; the best third variable changes depending on the p_T and R considered.

In conclusion, it appears that there is a rich and complex structure in terms of the degree to which the discriminatory information provided by the set of variables considered overlaps, with the degree of overlap apparently decreasing at higher p_T . This suggests that in all p_T ranges, but especially at higher p_T , there are substantial performance gains to be made by designing a more complex multivariate W tagger.

6.4 Conclusions

We have studied the performance, in terms of the degree to which a hadronically decaying W boson can be separated from a gluonic background, of a number of groomed jet masses, substructure variables, and BDT combinations of

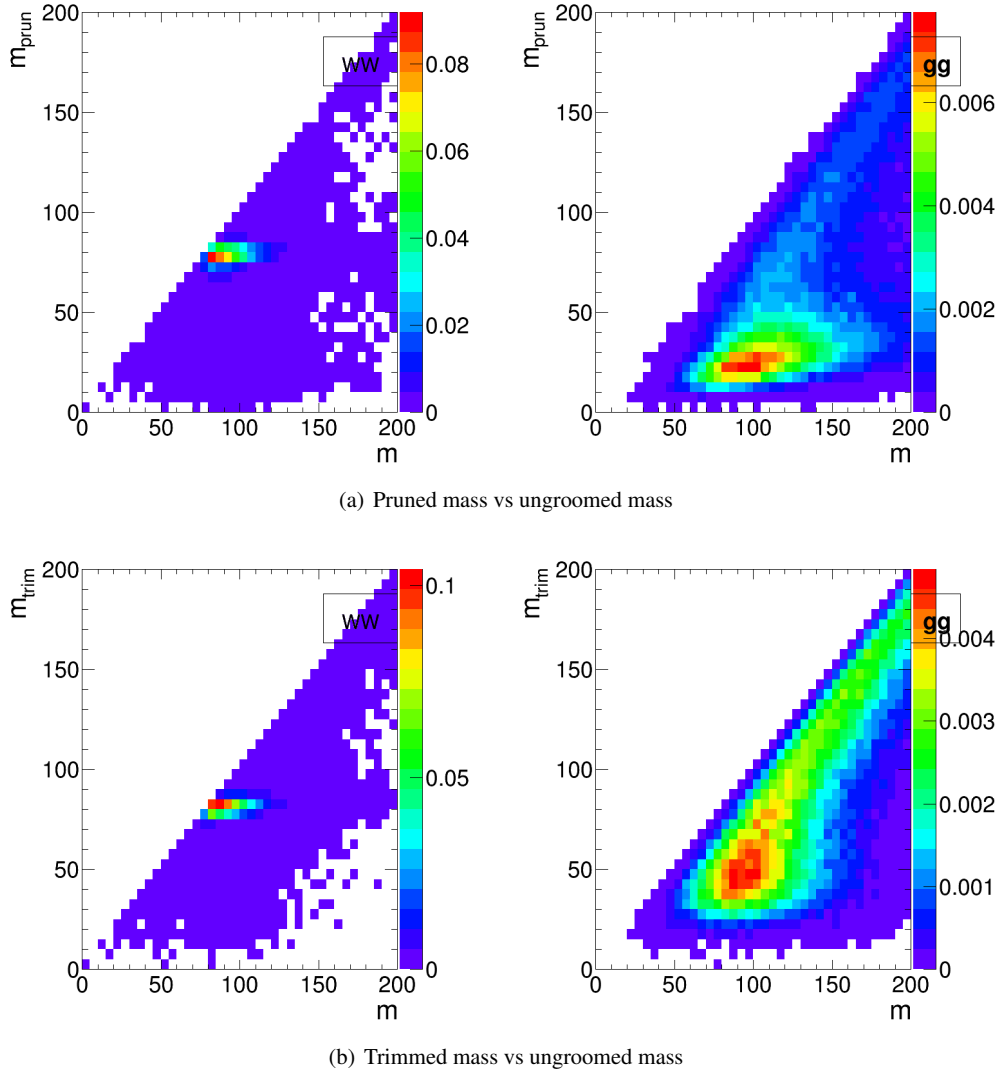


Fig. 19 2-D plots showing the correlation between groomed and ungroomed mass for WW and gg events in the p_T 1.0-1.1 TeV bin using the anti- k_T $R=0.8$ algorithm.

the above. We have used this to build a picture of how the discriminatory information contained in the variables overlaps, and how this complementarity between the variables changes with p_T and anti- k_T distance parameter R .

In terms of the performance of individual variables, we find that, in agreement with other studies [REF], in general the groomed masses perform best, with a background rejection power that increases with increasing p_T , but which is more constant with respect to changes in R . Conversely, the performance of other substructure variables, such as $C_2^{\beta=1}$ and $\tau_{21}^{\beta=1}$ is more susceptible to changes in radius, with background rejection power decreasing with increasing R .

The best two-variable performance is obtained by combining a groomed mass with a substructure variable. Which particular substructure variable works best in combination is strongly dependent on p_T and R . $C_2^{\beta=1}$ offers significant

complementarity to groomed mass at smaller R , owing to the small degree of correlation between the variables. However, the sensitivity of $C_2^{\beta=1}$ to soft, wide-angle radiation leads to worse discrimination power at large R , where $\tau_{21}^{\beta=1}$ performs better in combination. Our studies also demonstrate the potential for enhanced discrimination by combining groomed and ungroomed mass information, although the use of ungroomed mass in this may in practice be limited by the presence of pile-up that is not considered in these studies.

By examining the performance of a BDT combination of all the variables considered, it is clear that there are potentially substantial performance gains to be made by designing a more complex multivariate W tagger, especially at higher p_T .

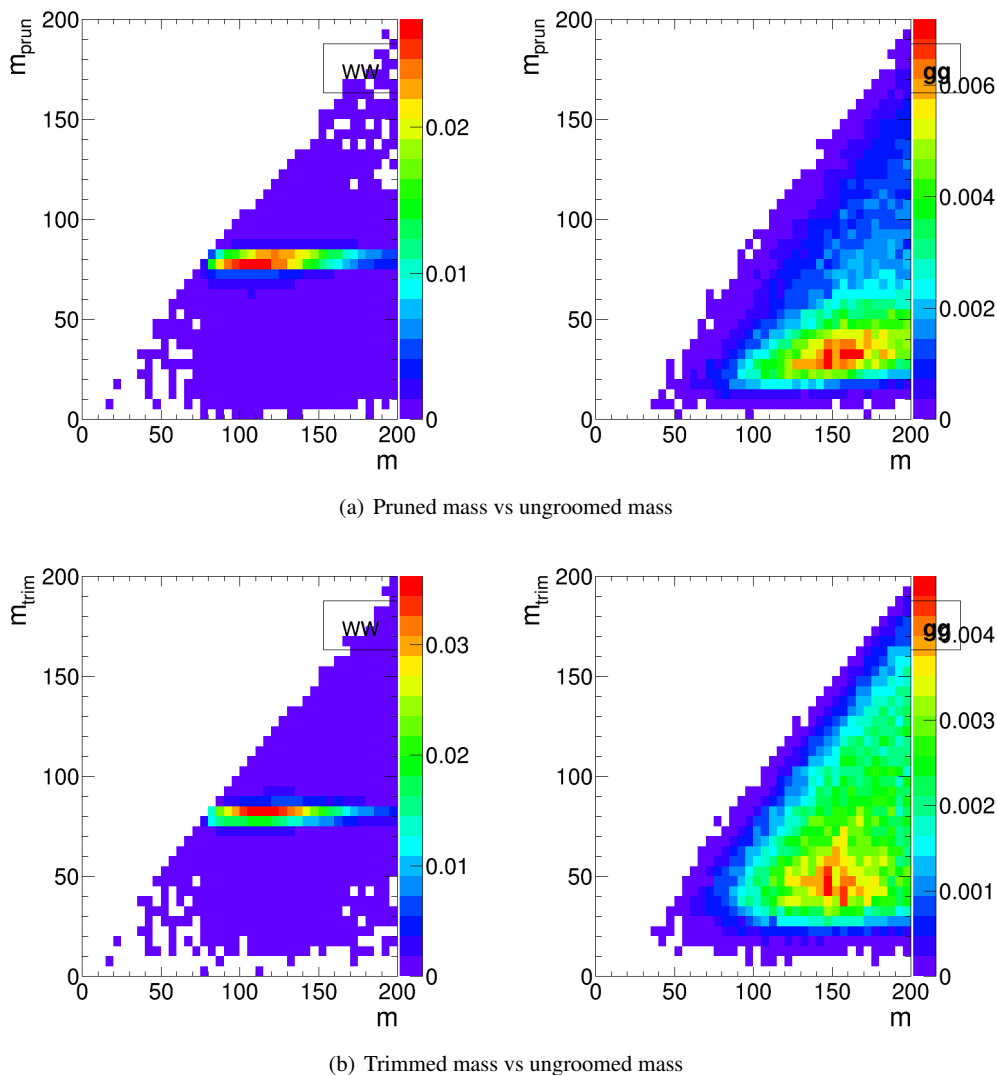


Fig. 20 2-D plots showing the correlation between groomed and ungroomed mass for WW and gg events in the p_T 1.0-1.1 TeV bin using the anti- k_T $R=1.2$ algorithm.

788 7 Top Tagging

789 In this section, we study the identification of boosted top
 790 quarks at Run II of the LHC. Boosted top quarks result in
 791 large-radius jets with complex substructure, containing a b -
 792 subjet and a boosted W . The additional kinematic handles
 793 coming from the reconstruction of the W mass and b -tagging
 794 allow a very high degree of discrimination of top quark jets
 795 from QCD backgrounds.

796 We consider top quarks with moderate boost (600-1000
 797 GeV), and perhaps most interestingly, at high boost ($\gtrsim 1500$
 798 GeV). Top tagging faces several challenges in the high- p_T
 799 regime. For such high- p_T jets, the b -tagging efficiencies are
 800 no longer reliably known. Also, the top jet can also accom-
 801 panied by additional radiation with $p_T \sim m_t$, leading to com-
 802 binatoric ambiguities of reconstructing the top and W , and

803 the possibility that existing taggers or observables shape the
 804 background by looking for subjet combinations that recon-
 805 struct m_t/m_W . To study this, we examine the performance of
 806 both mass-reconstruction variables, as well as shape observ-
 807 ables that probe the three-pronged nature of the top jet and
 808 the accompanying radiation pattern.

We use the top quark MC samples for each bin described
 in Section 2.2. The analysis relies on FASTJET 3.0.3 for jet
 clustering and calculation of jet substructure observables.
 Jets are clustered using the anti- k_t algorithm. An upper and
 lower p_T cut are applied after jet clustering to each sample
 to ensure similar p_T spectra in each bin. The bins in lead-
 ing jet p_T that are investigated for top tagging are 600-700
 GeV, 1-1.1 TeV, and 1.5-1.6 TeV. Jets are clustered with radii
 $R = 0.4, 0.8, \text{ and } 1.2$; $R = 0.4$ jets are only studied in the 1.5-

818 1.6 TeV bin because for top quarks with this boost, the top
819 decay products are all contained within an $R = 0.4$ jet.

820 7.1 Methodology

821 We study a number of top-tagging strategies, in particular:

- 822 1. HEPTopTagger
- 823 2. Johns Hopkins Tagger (JH)
- 824 3. Trimming
- 825 4. Pruning

826 The top taggers have criteria for reconstructing a top and
827 W candidate, and a corresponding top and W mass, as de-
828 scribed in Section 3.3, while the grooming algorithms (trim-
829 ming and pruning) do not incorporate a W -identification step.
830 For a level playing field, where grooming is used we con-
831 struct a W candidate mass, m_W , from the three leading sub-
832 jets by taking the mass of the pair of subjets with the smallest
833 invariant mass; in the case that only two subjets are recon-
834 structed, we take the mass of the leading subjet. The top
835 mass, m_t , is the mass of the groomed jet. All of the above
836 taggers and groomers incorporate a step to remove pile-up
837 and other soft radiation.

838 We also consider the performance of the following jet
839 shape observables:

- 840 – The ungroomed jet mass.
- 841 – N -subjettiness ratios τ_2/τ_1 and τ_3/τ_2 with $\beta = 1$ and the
842 “winner-takes-all” axes.
- 843 – 2-point energy correlation function ratios $C_2^{\beta=1}$ and $C_3^{\beta=1}$
- 844 – The pruned Qjet mass volatility, Γ_{Qjet} .

845 In addition to the jet shape performance, we combine the
846 jet shapes with the mass-reconstruction methods described
847 above to determine the optimal combined performance.

848 For determining the performance of multiple variables,
849 we combine the relevant tagger output observables and/or jet
850 shapes into a boosted decision tree (BDT), which determines
851 the optimal cut. Additionally, because each tagger has two
852 input parameters, as described in Section 3.3, we scan over
853 reasonable values of the parameters to determine the optimal
854 value that gives the largest background rejection for each top
855 tagging signal efficiency. This allows a direct comparison
856 of the optimized version of each tagger. The input values
857 scanned for the various algorithms are:

- 858 – **HEPTopTagger:** $m \in [30, 100]$ GeV, $\mu \in [0.5, 1]$
- 859 – **JH Tagger:** $\delta_p \in [0.02, 0.15]$, $\delta_R \in [0.07, 0.2]$
- 860 – **Trimming:** $f_{\text{cut}} \in [0.02, 0.14]$, $R_{\text{trim}} \in [0.1, 0.5]$
- 861 – **Pruning:** $z_{\text{cut}} \in [0.02, 0.14]$, $R_{\text{cut}} \in [0.1, 0.6]$

862 7.2 Single-observable performance

863 We start by investigating the behaviour of individual jet sub-
864 structure observables. Because of the rich, three-pronged struc-

ture of the top decay, it is expected that combinations of
masses and jet shapes will far outperform single observables
in identifying boosted tops. However, a study of the top-
tagging performance of single variables facilitates a direct
comparison with the W tagging results in Section 6, and also
allows a straightforward examination of the performance of
each observable for different p_T and jet radius.

Fig. 21 shows the ROC curves for each of the top-tagging
observables, with the bare (ungroomed) jet mass also plotted
for comparison. The jet shape observables all perform sub-
stantially worse than jet mass, unlike W tagging for which
several observables are competitive with or perform better
than jet mass (see, for example, Fig. 7). To understand why
this is the case, consider N -subjettiness. The W is two-pronged
and the top is three-pronged; therefore, we expect τ_{21} and
 τ_{32} to be the best-performant N -subjettiness ratio, respec-
tively. However, τ_{21} also contains an implicit cut on the de-
nominator, τ_1 , which is strongly correlated with jet mass.
Therefore, τ_{21} combines both mass and shape information
to some extent. By contrast, and as is clear in Fig.21(a), the
best shape for top tagging is τ_{32} , which contains no informa-
tion on the mass. Therefore, it is unsurprising that the shapes
most useful for top tagging are less sensitive to the jet mass,
and under-perform relative to the corresponding observables
for W tagging.

Of the two top tagging algorithms, we can see from Fig-
ure 21 that the Johns Hopkins (JH) tagger out-performs the
HEPTopTagger in terms of its signal-to-background separa-
tion power in both the top and W candidate masses. In Fig-
ure 22 we show the histograms for the top mass output from
the JH and HEPTopTagger for different R in the p_T 1.5-1.6
TeV bin, and in Figure 23 for different p_T at $R = 0.8$, opti-
mized at a signal efficiency of 30%. One can see from these
figures that the likely reason for the better performance of
the JH tagger is that, in the HEPTopTagger algorithm, the
jet is filtered to select the five hardest subjets, and then three
subjets are chosen which reconstruct the top mass. This re-
quirement tends to shape a peak in the QCD background
around m_t for the HEPTopTagger, while the JH tagger has
no such requirement. It has been suggested by Anders *et*
al. [37] that performance in the HEPTopTagger may be im-
proved by selecting the three subjets reconstructing the top
only among those that pass the W mass constraints, which
somewhat reduces the shaping of the background. The dis-
crepancy between the JH and HEPTopTaggers is more pro-
nounced at higher p_T and larger jet radius (see Figs. 26 and
29).

We also see in Figure 21(b) that the top mass from the
JH tagger and the HEPTopTagger has superior performance
relative to either of the grooming algorithms; this is because
the pruning and trimming algorithms do not have inherent
 W -identification steps and are not optimized for this pur-
pose. Indeed, because of the lack of a W -identification step,

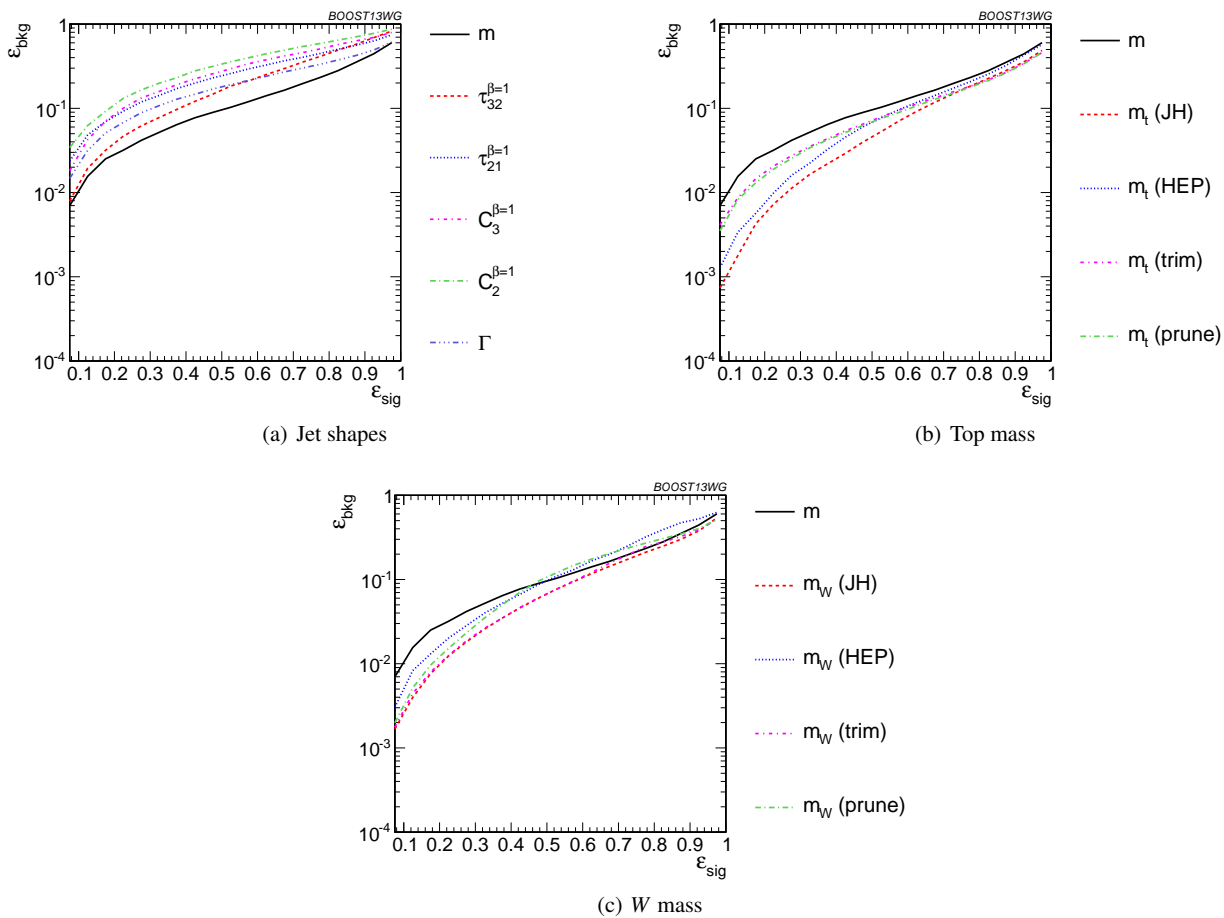


Fig. 21 Comparison of single-variable top-tagging performance in the $p_T = 1 - 1.1$ GeV bin using the anti- k_T , $R=0.8$ algorithm.

grooming algorithms are forced to strike a balance between under-grooming the jet, which broadens the signal peak due to UE contamination and features a larger background rate, and over-grooming the jet, which occasionally throws out the b -jet and preserves only the W components inside the jet. We demonstrate this effect in Figures 22 and 23, showing that with $\epsilon_{\text{sig}} = 0.3 - 0.35$, the optimal performance of the tagger over-grooms a substantial fraction of the jets ($\sim 20 - 30\%$), leading to a spurious second peak at the W mass. This effect is more pronounced at large R and p_T , since more aggressive grooming is required in these limits to combat the increased contamination from UE and QCD radiation.

In Figures 24 and 26 we directly compare ROC curves for jet shape observable performance and top mass performance respectively in the three different p_T bins considered, whilst keeping the jet radius fixed at $R=0.8$. The input parameters of the taggers, groomers and shape variables are separately optimized in each p_T bin. One can see from Figure 24 that the tagging performance of jet shapes do not change substantially with p_T . The observables $\tau_{32}^{(\beta=1)}$ and Qjet volatility Γ have the most variation and tend to degrade with higher p_T , as can be seen in Figure 25. This makes

sense, as higher- p_T QCD jets have more, harder emissions within the jet, giving rise to substructure that fakes the signal. By contrast, from Figure 26 we can see that most of the top mass observables have superior performance at higher p_T due to the radiation from the top quark becoming more collimated. The notable exception is the HEP TopTagger, which degrades at higher p_T , likely in part due to the background-shaping effects discussed earlier.

In Figures 27 and 29 we directly compare ROC curves for jet shape observable performance and top mass performance respectively for the three different jet radii considered within the p_T 1.5-1.6 TeV bin. Again, the input parameters of the taggers, groomers and shape variables are separately optimized for each jet radius. We can see from these figures that most of the top tagging variables, both shape and reconstructed top mass, perform best for smaller radius. This is likely because, at such high p_T , most of the radiation from the top quark is confined within $R = 0.4$, and having a larger jet radius makes the observable more susceptible to contamination from the underlying event and other uncorrelated radiation. In Figure 28, we compare the individual top signal and QCD background distributions for each shape variable

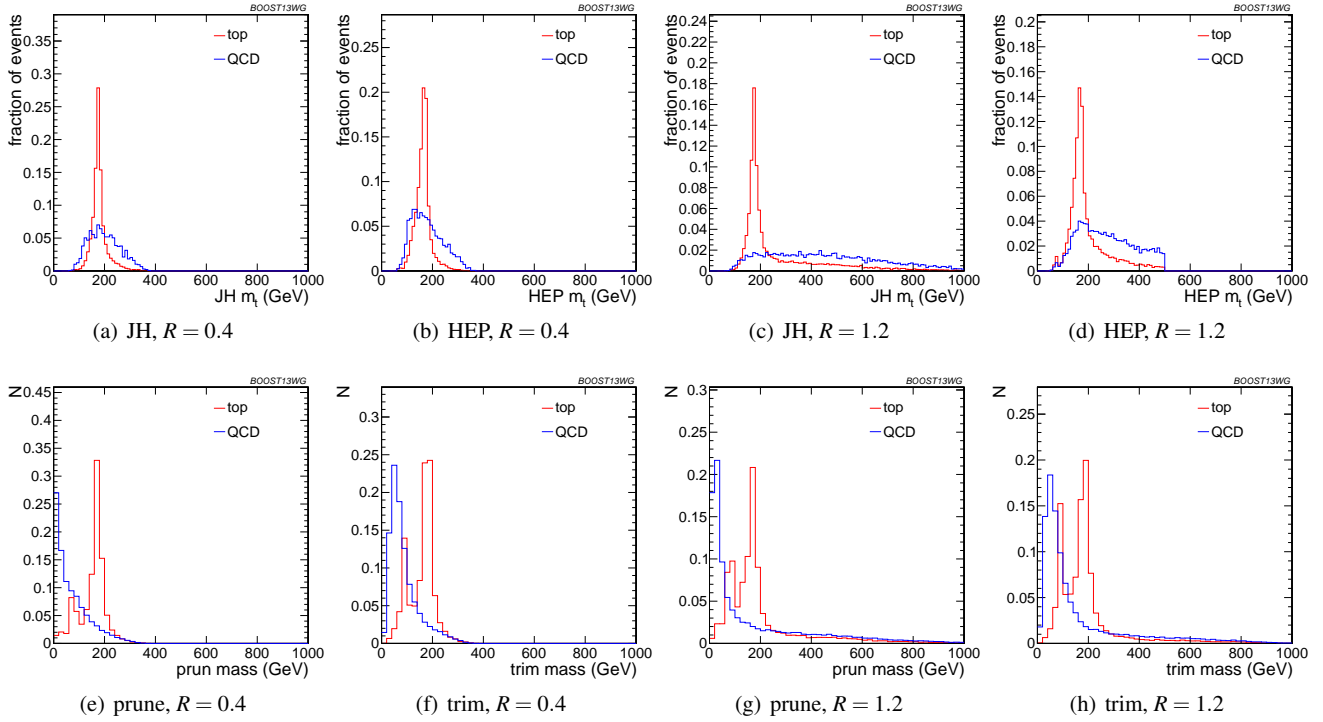


Fig. 22 Comparison of top mass reconstruction with the Johns Hopkins (JH), HEPTopTaggers (HEP), pruning, and trimming at different R using the anti- k_T algorithm, $p_T = 1.5 - 1.6$ TeV. Each histogram is shown for the working point optimized for best performance with m_t in the $0.3 - 0.35$ signal efficiency bin, and is normalized to the fraction of events passing the tagger. In this and subsequent plots, the HEPTopTagger distribution cuts off at 500 GeV because the tagger fails to tag jets with a larger mass.

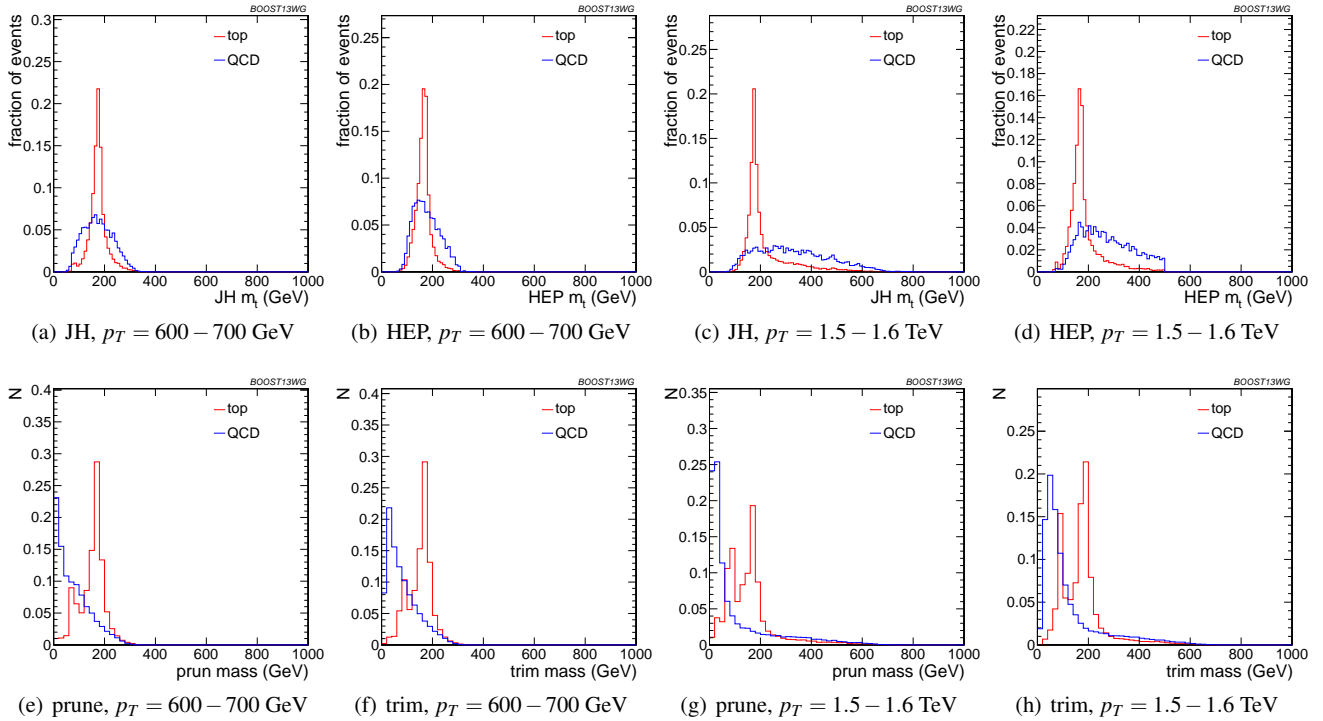


Fig. 23 Comparison of top mass reconstruction with the Johns Hopkins (JH), HEPTopTaggers (HEP), pruning, and trimming at different p_T using the anti- k_T algorithm, $R = 0.8$. Each histogram is shown for the working point optimized for best performance with m_t in the $0.3 - 0.35$ signal efficiency bin, and is normalized to the fraction of events passing the tagger.

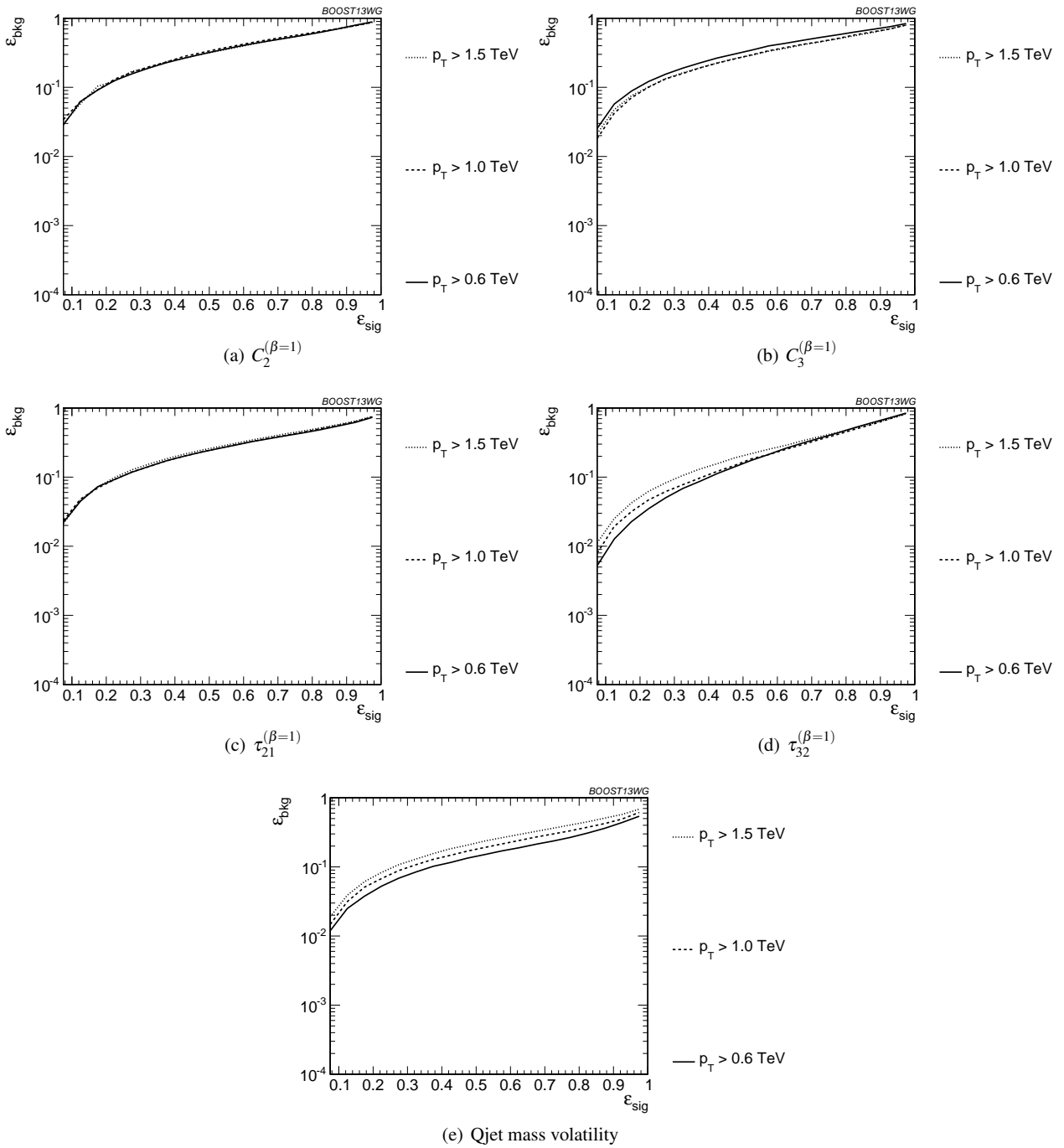


Fig. 24 Comparison of individual jet shape performance at different p_T using the anti- k_T $R=0.8$ algorithm.

962 considered in the p_T 1.5-1.6 TeV bin for the various jet radii
 963 One can see that the distributions for both signal and back-
 964 ground broaden with increasing R , degrading the discrimi-
 965 nating power. For $C_2^{(\beta=1)}$ and $C_3^{(\beta=1)}$, the background distri-
 966 butions are shifted upward as well. Therefore, the discrim-
 967 inating power generally gets worse with increasing R . The
 968 main exception is for $C_3^{(\beta=1)}$, which performs optimally at
 969 $R = 0.8$; in this case, the signal and background coinciden-

tally happen to have the same distribution around $R = 0.4$,
 and so $R = 0.8$ gives better discrimination.

7.3 Performance of multivariable combinations

We now consider various BDT combinations of the observables from Section 7.2, using the techniques described in Section 4. In particular, we consider the performance of in-

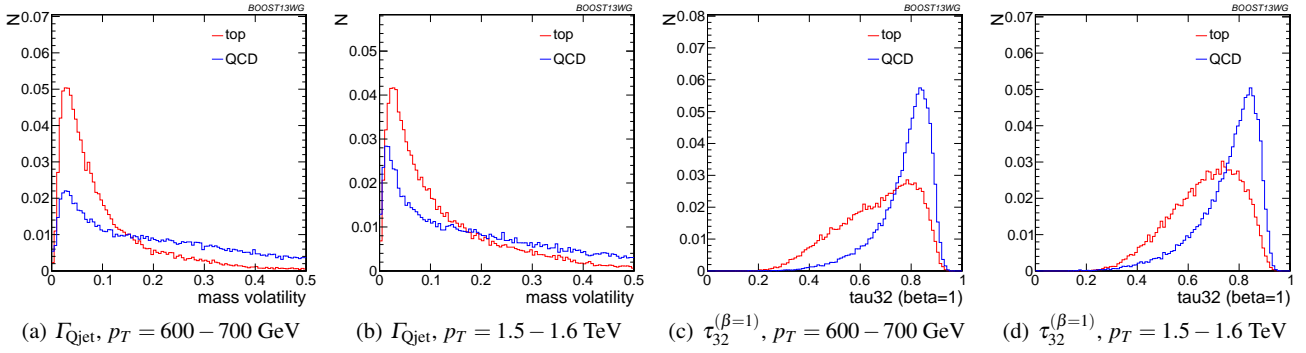


Fig. 25 Comparison of Γ_{Qjet} and $\tau_{32}^{\beta=1}$ at $R = 0.8$ and different values of the p_T . These shape observables are the most sensitive to varying p_T .

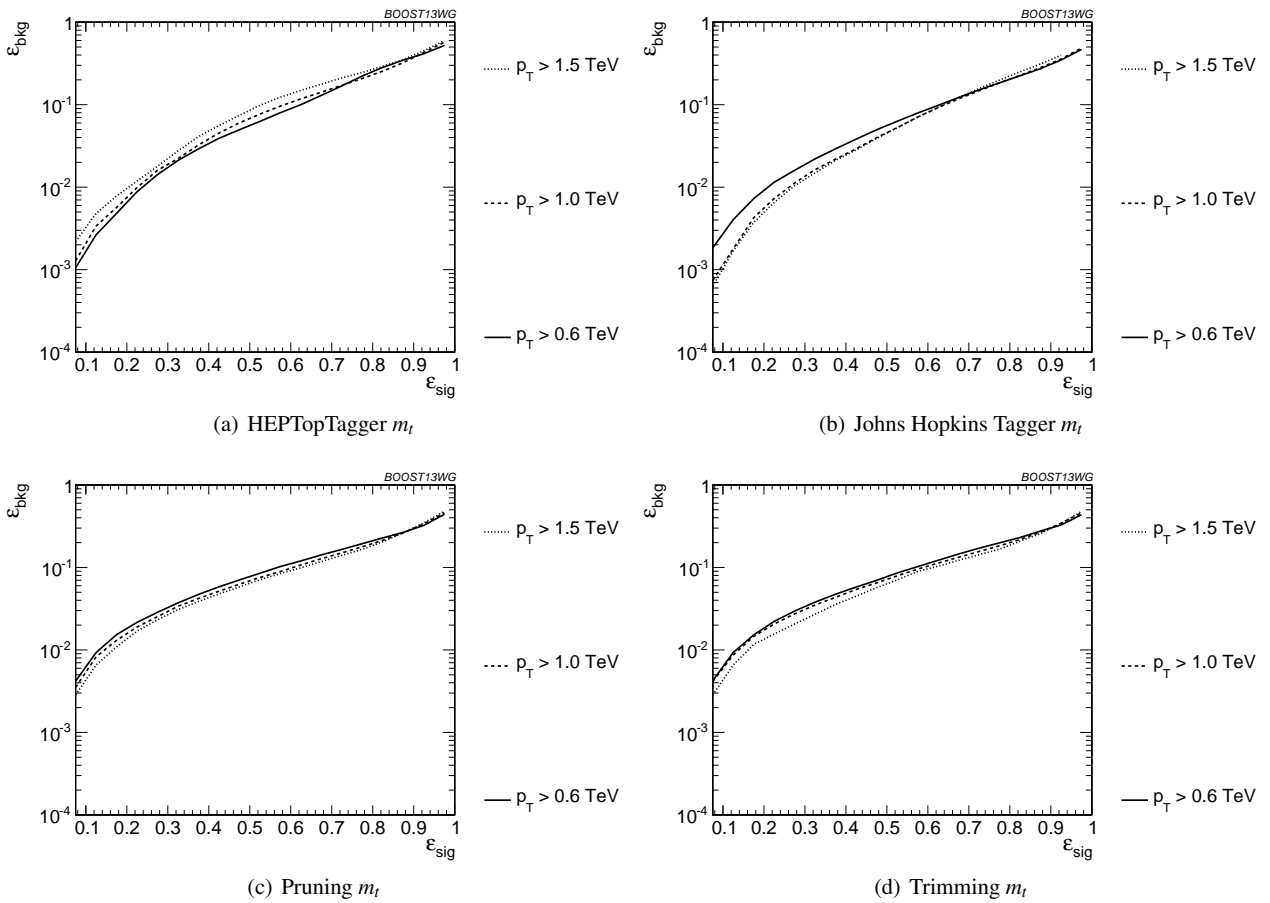


Fig. 26 Comparison of top mass performance of different taggers at different p_T using the anti- k_T $R=0.8$ algorithm.

976 individual taggers such as the JH tagger and HEPTopTagger₉₈₅
 977 which output information about the top and W candidate₉₈₆
 978 masses and the helicity angle; groomers, such as trimming₉₈₇
 979 and pruning, which remove soft, uncorrelated radiation from
 980 the top candidate to improve mass reconstruction, and to₉₈₈
 981 which we have added a W reconstruction step; and the com-₉₈₉
 982 bination of the outputs of the above taggers/groomers, both₉₉₀
 983 with each other, and with shape variables such as N -subjettiness₉₉₁
 984 ratios and energy correlation ratios. For all observables with₉₉₂
 993

tunable input parameters, we scan and optimize over realistic values of such parameters, as described in Section 7.1.

In Figure 30, we directly compare the performance of the HEPTopTagger, the JH tagger, trimming, and pruning, in the $p_T = 1 - 1.1 \text{ TeV}$ bin using jet radius $R=0.8$, where both m_t and m_W are used in the groomers. Generally, we find that pruning, which does not naturally incorporate subjets into the algorithm, does not perform as well as the others. Interestingly, trimming, which does include a subject-identification

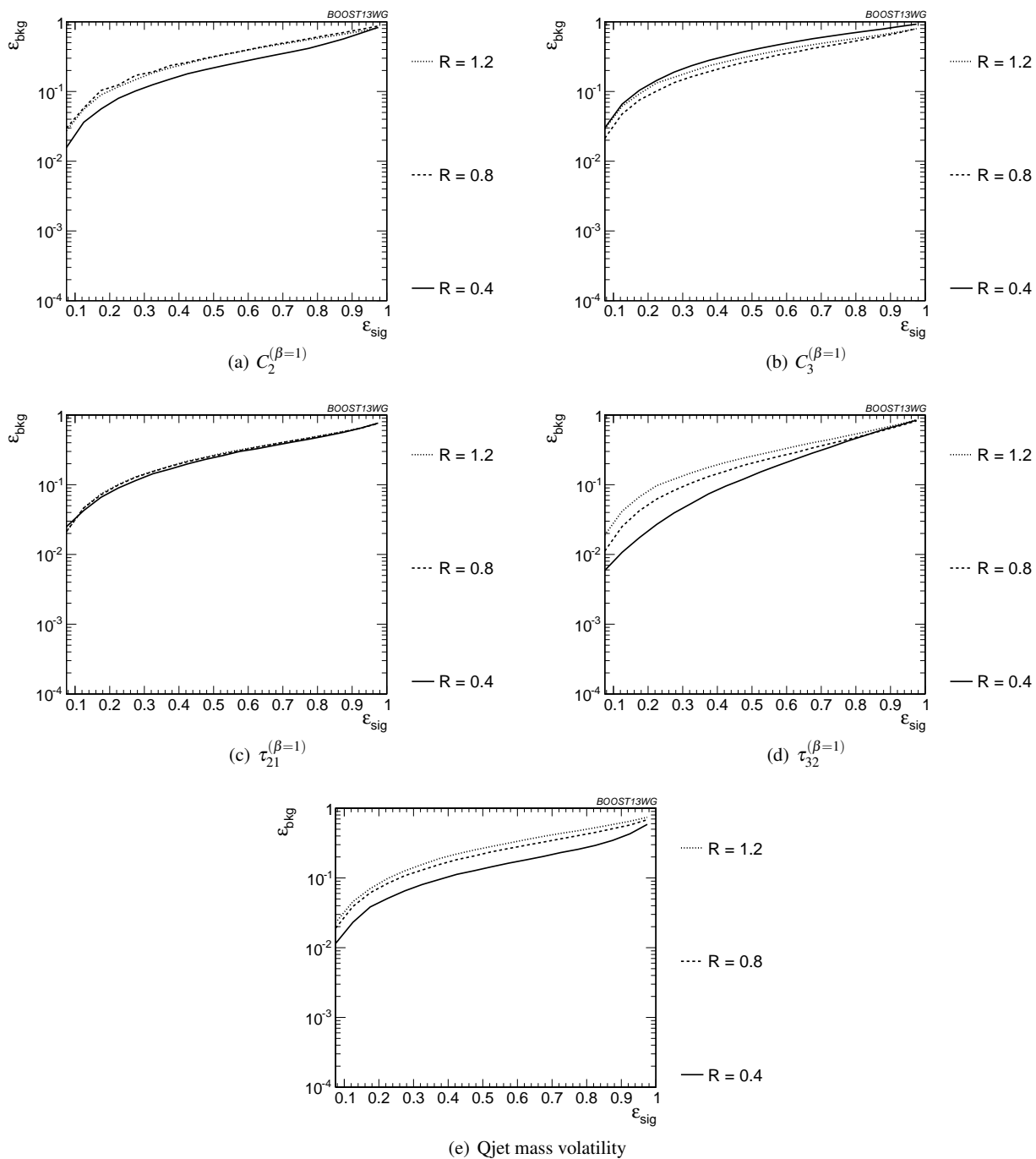


Fig. 27 Comparison of individual jet shape performance at different R in the $p_T = 1.5 - 1.6$ TeV bin.

994 step, performs comparably to the HEPTopTagger over much
 995 of the range, possibly due to the background-shaping ob-
 996 served in Section 7.2. By contrast, the JH tagger outperforms
 997 the other algorithms. To determine whether there is comple-
 998 mentary information in the mass outputs from different top
 999 taggers, we also consider in Figure 30 a multivariable com-
 1000 bination of all of the JH and HEPTopTagger outputs. The
 1001 maximum efficiency of the combined JH and HEPTopTagger

is limited, as some fraction of signal events inevitably
 fails either one or other of the taggers. We do see a 20-50%
 improvement in performance when combining all outputs,
 which suggests that the different algorithms used to identify
 the top and W for different taggers contains complementary
 information.

In Figure 31 we present the results for multivariable com-
 binations of the top tagger outputs with and without shape

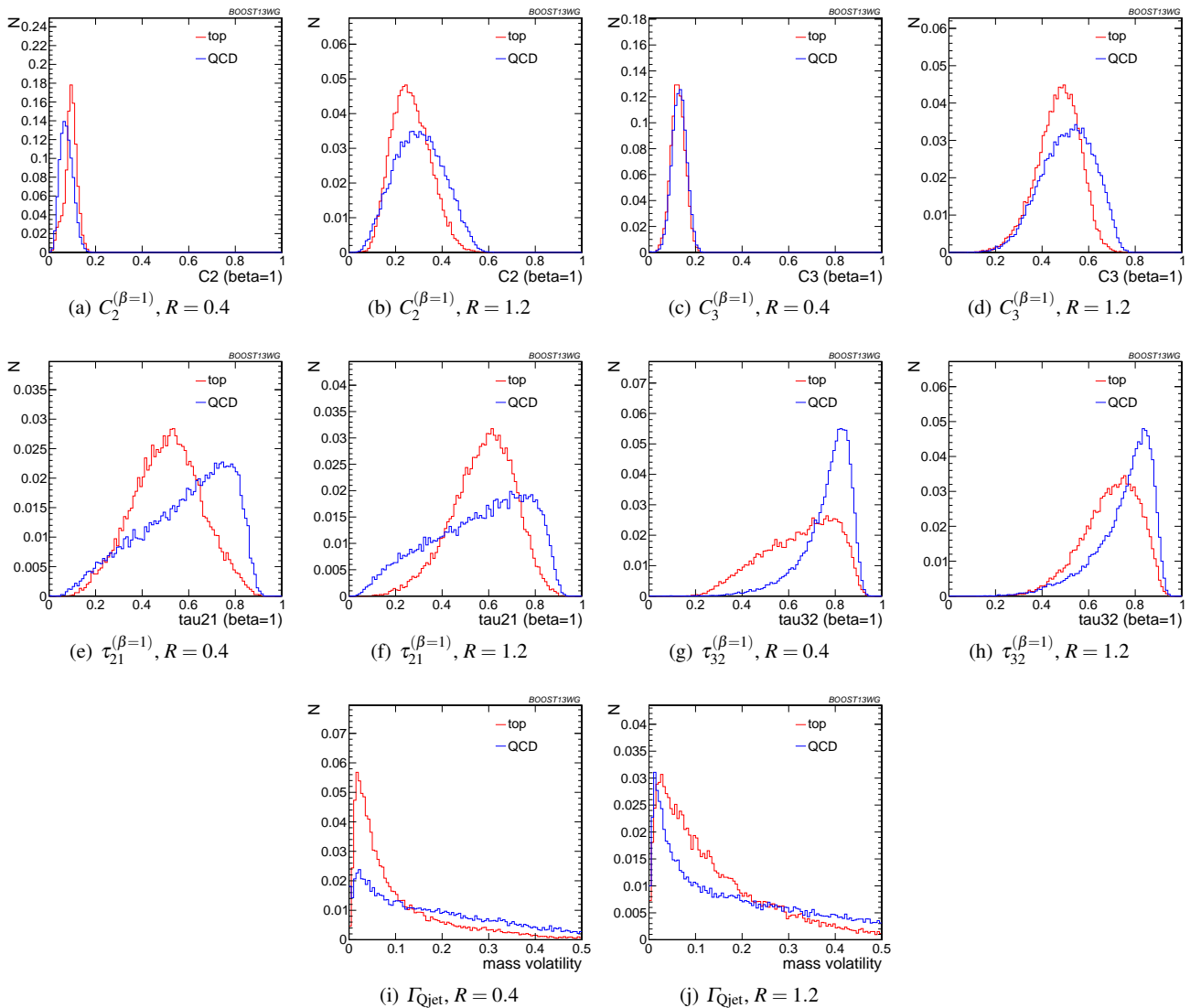


Fig. 28 Comparison of various shape observables in the $p_T = 1.5 - 1.6$ TeV bin and different values of the anti- k_T radius R .

1010 variables. We see that, for both the HEPTopTagger and the
 1011 JH tagger, the shape observables contain additional information
 1012 uncorrelated with the masses and helicity angle, and
 1013 give on average a factor 2-3 improvement in signal discrimination.
 1014 We see that, when combined with the tagger outputs,
 1015 both the energy correlation functions $C_2 + C_3$ and the N
 1016 subjettness ratios $\tau_{21} + \tau_{32}$ give comparable performance,
 1017 while the Qjet mass volatility is slightly worse; this is un-
 1018 surprising, as Qjets accesses shape information in a more
 1019 indirect way from other shape observables. Combining all
 1020 shape observables with a single top tagger provides even
 1021 greater enhancement in discrimination power. We directly
 1022 compare the performance of the JH and HEPTopTaggers in
 1023 Figure 31(c). Combining the taggers with shape information
 1024 nearly erases the difference between the tagging methods
 1025 observed in Figure 30; this indicates that combining the

shape information with the HEPTopTagger identifies the differ-
 ences between signal and background missed by the tagger
 alone. This also suggests that further improvement to discrimi-
 nating power may be minimal, as various multivariable combina-
 tions are converging to within a factor of 20% or so.

In Figure 32 we present the results for multivariable combina-
 tions of groomer outputs with and without shape variables. As
 with the tagging algorithms, combinations of groomers with shape
 observables improves their discriminating power; combinations
 with $\tau_{32} + \tau_{21}$ perform comparably to those with $C_3 + C_2$,
 and both of these are superior to combinations with the mass
 volatility, Γ . Substantial improvement is further possible by
 combining the groomers with all shape observables. Not surpris-
 ingly, the taggers that lag behind in performance enjoy the largest
 gain in signal-background

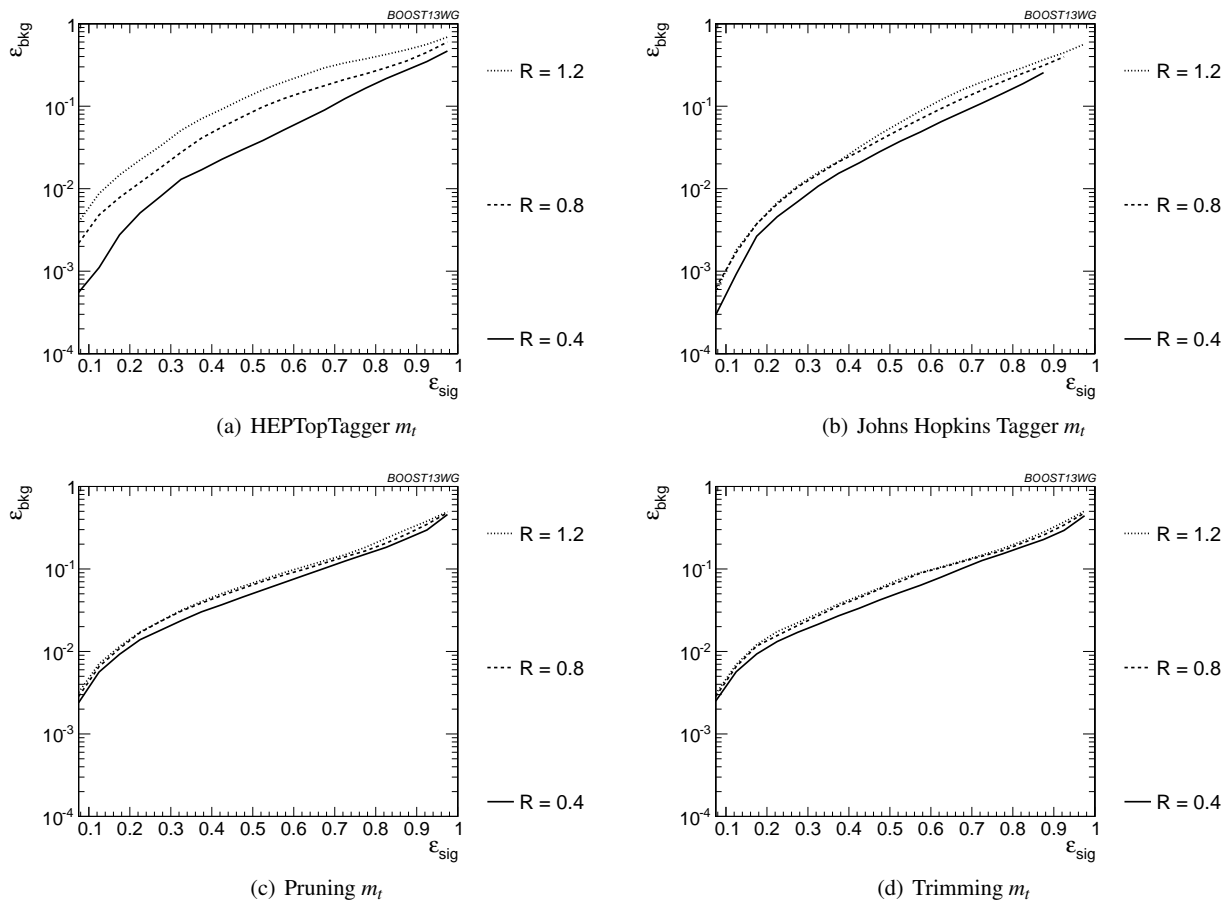


Fig. 29 Comparison of top mass performance of different taggers at different R in the $p_T = 1.5 - 1.6$ TeV bin.

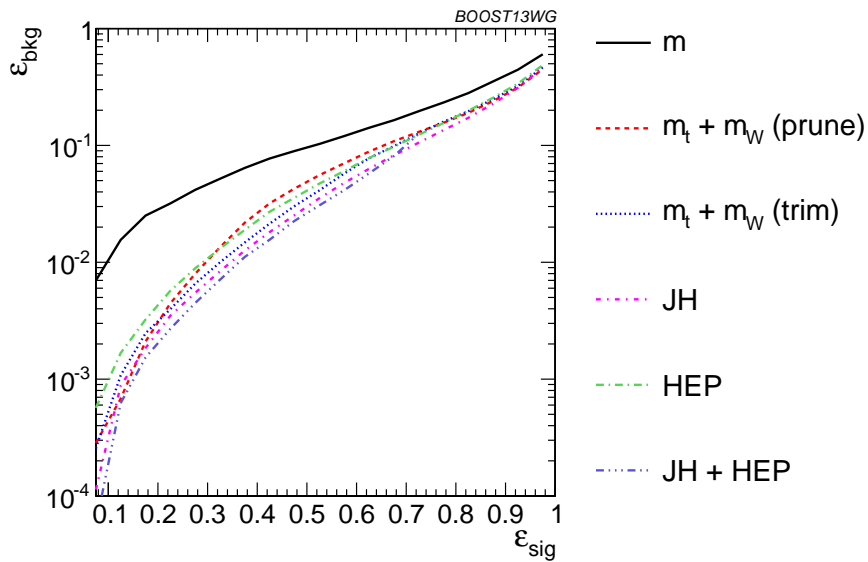


Fig. 30 The performance of the various taggers in the $p_T = 1 - 1.1$ TeV bin using the anti- k_T $R=0.8$ algorithm. For the groomers a BDT combination of the reconstructed m_t and m_W are used. Also shown is a multivariable combination of all of the JH and HEPTopTagger outputs. The ungroomed mass performance is shown for comparison.

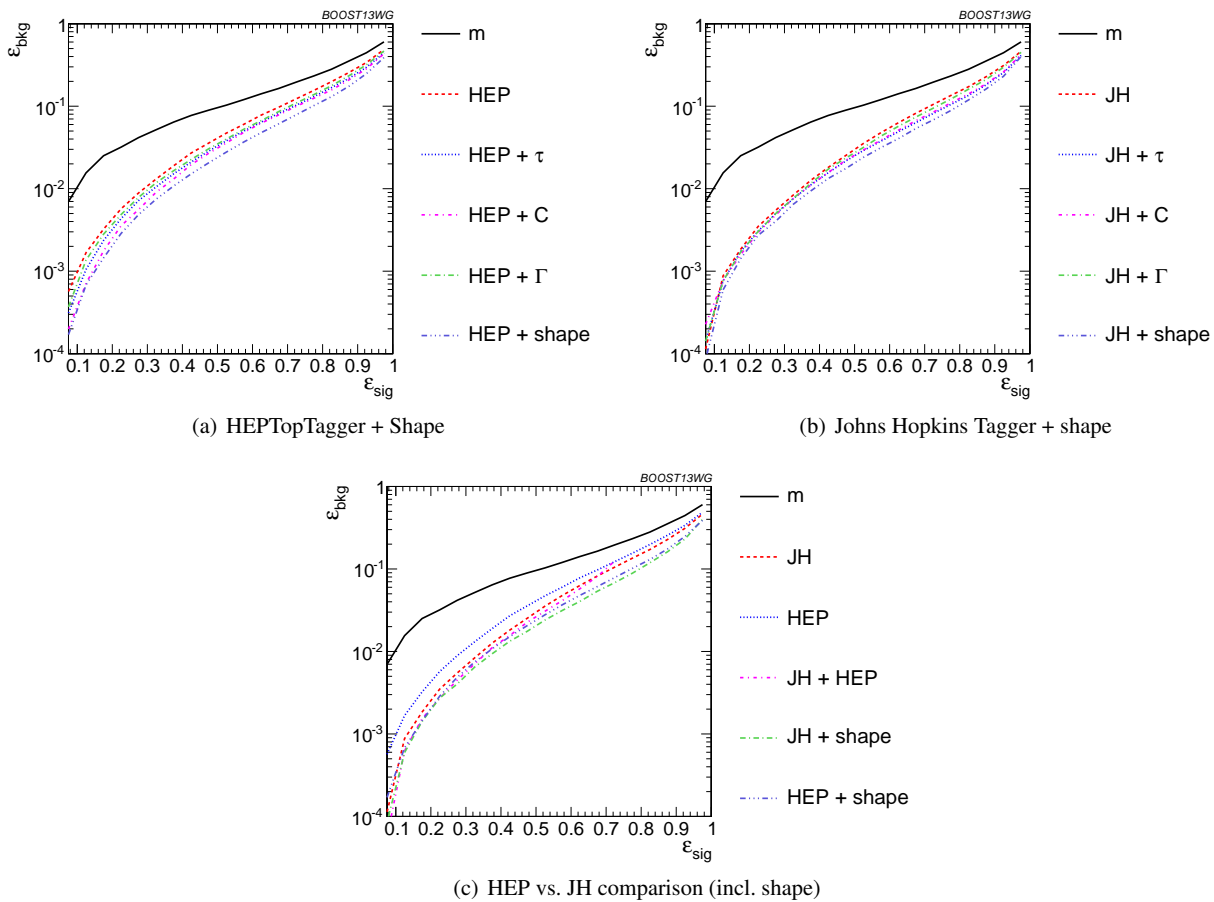


Fig. 31 The performance of BDT combinations of the JH and HepTopTagger outputs with various shape observables in the $p_T = 1 - 1.1$ TeV bin using the anti- k_T $R=0.8$ algorithm. Taggers are combined with the following shape observables: $\tau_{21}^{(\beta=1)} + \tau_{32}^{(\beta=1)}$, $C_2^{(\beta=1)} + C_3^{(\beta=1)}$, Γ_{Qjet} , and all of the above (denoted “shape”).

1042 discrimination with the addition of shape observables. Once
 1043 again, in Figure 32(c), we find that the differences between
 1044 pruning and trimming are erased when combined with shape
 1045 information. 1066

1046 Finally, in Figure 33, we compare the performance of
 1047 each of the tagger/groomers when their outputs are com-
 1048 bined with all of the shape observables considered. One can
 1049 see that the discrepancies between the performance of the
 1050 different taggers/groomers all but vanishes, suggesting per-
 1051 haps that we are here utilising all available signal-background
 1052 discrimination information, and that this is the optimal top
 1053 tagging performance that could be achieved in these condi-
 1054 tions. 1074

1055 Up to this point we have just considered the combined
 1056 multivariable performance in the p_T 1.0-1.1 TeV bin with
 1057 jet radius $R=0.8$. We now compare the BDT combinations
 1058 of tagger outputs, with and without shape variables, at dif-
 1059 ferent p_T . The taggers are optimized over all input param-
 1060 eters for each choice of p_T and signal efficiency. As with the
 1061 single-variable study, we consider anti- k_T jets clustered with
 1062 $R = 0.8$ and compare the outcomes in the $p_T = 500 - 600$

GeV, $p_T = 1 - 1.1$ TeV, and $p_T = 1.5 - 1.6$ TeV bins. The
 comparison of the taggers/groomers is shown in Figure 34.
 The behaviour with p_T is qualitatively similar to the be-
 haviour of the m_t observable for each tagger/groomer shown
 in Figure 26; this suggests that the p_T behaviour of the tag-
 gers is dominated by the top mass reconstruction. As before,
 the HEPTopTagger performance degrades slightly with in-
 creased p_T due to the background shaping effect, while the
 JH tagger and groomers modestly improve in performance.

In Figure 35, we show the p_T dependence of BDT com-
 binations of the JH tagger output combined with shape ob-
 servables. We find that the curves look nearly identical: the
 p_T dependence is dominated by the top mass reconstruction,
 and combining the tagger outputs with different shape ob-
 servables does not substantially change this behaviour. The
 same holds true for trimming and pruning. By contrast, HEPTopTagger
 ROC curves, shown in Figure 36, do change somewhat when
 combined with different shape observables; due to the suboptimal
 performance of the HEPTopTagger at high p_T , we find that
 combining the HEPTopTagger with

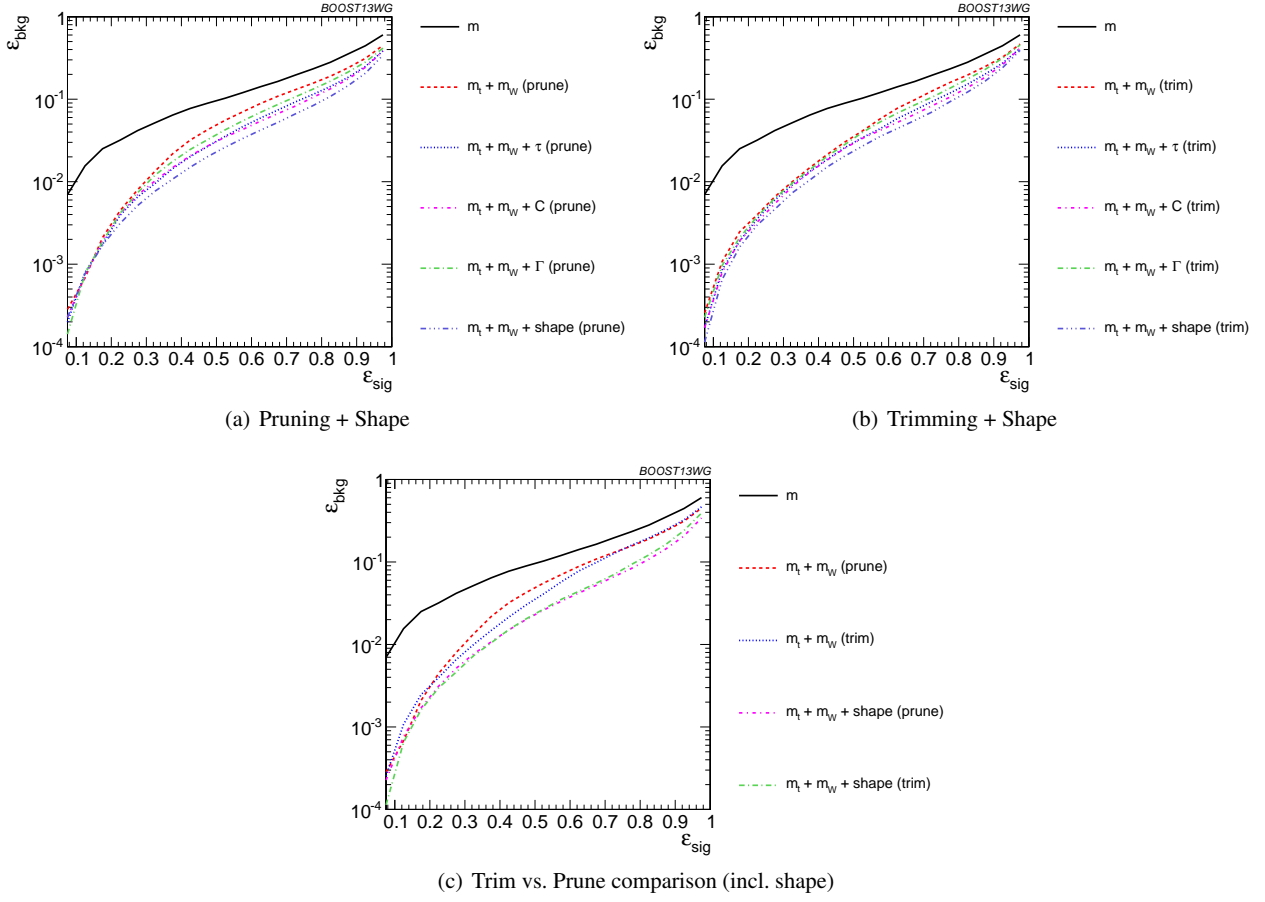


Fig. 32 The performance of the BDT combinations of the trimming and pruning outputs with various shape observables in the $p_T = 1 - 1.1$ TeV bin using the anti- k_T $R=0.8$ algorithm. Groomer mass outputs are combined with the following shape observables: $\tau_{21}^{(\beta=1)} + \tau_{32}^{(\beta=1)}$, $C_2^{(\beta=1)} + C_3^{(\beta=1)}$, Γ_{Qjet} , and all of the above (denoted “shape”).

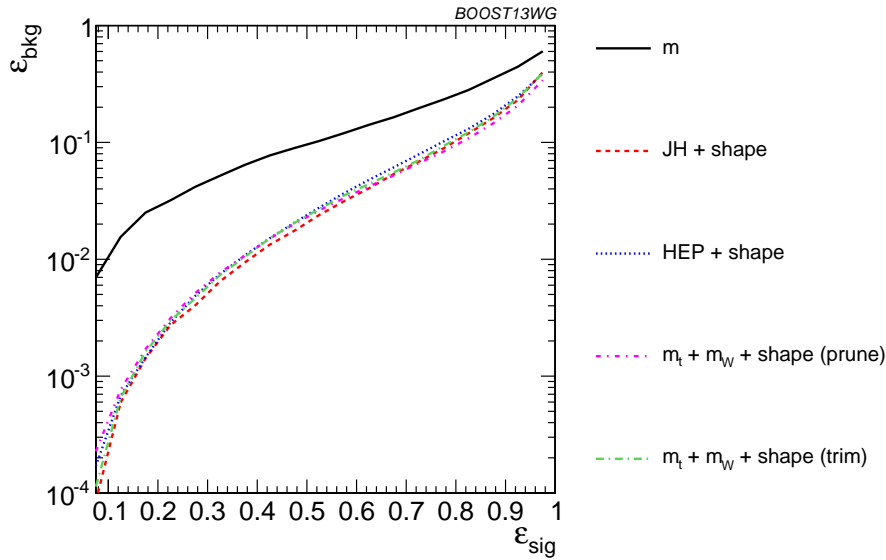


Fig. 33 Comparison of the performance of the BDT combinations of all the groomer/tagger outputs with all the available shape observables in the $p_T = 1 - 1.1$ TeV bin using the anti- k_T $R=0.8$ algorithm. Tagger/groomer outputs are combined with all of the following shape observables: $\tau_{21}^{(\beta=1)} + \tau_{32}^{(\beta=1)}$, $C_2^{(\beta=1)} + C_3^{(\beta=1)}$, Γ_{Qjet} .

$C_3^{(\beta=1)}$, which in Figure 24(b) is seen to have some modest improvement at high p_T , can improve its performance. Combining the HEPTopTagger with multiple shape observables gives the maximum improvement in performance at high p_T relative to at low p_T .

In Figure 37 we compare the BDT combinations of tagger outputs, with and without shape variables, at different radius R in the $p_T = 1.5 - 1.6$ TeV bin. The taggers are optimized over all input parameters for each choice of R and signal efficiency. We find that, for all taggers and groomers, the performance is always best at small R ; the choice of R is sufficiently large to admit the full top quark decay at such high p_T , but is small enough to suppress contamination from additional radiation. This is not altered when the taggers are combined with shape observable. For example, in Figure 38 is shown the dependence on R of the JH tagger when combined with shape observables, where one can see that the R -dependence is identical for all combinations. The same holds true for the HEPTopTagger, trimming, and pruning.

7.4 Performance at Sub-Optimal Working Points

Up until now, we have re-optimized our tagger and groomer parameters for each p_T , R , and signal efficiency working point. In reality, experiments will choose a finite set of working points to use. How do our results hold up when this is taken into account? To address this concern, we replicate our analyses, but only optimize the top taggers for a particular $p_T/R/$ efficiency and apply the same parameters to other scenarios. This allows us to determine the extent to which re-optimization is necessary to maintain the high signal-background discrimination power seen in the top tagging algorithms we study. The shape observables typically do not have any input parameters to optimize. Therefore, we focus on the taggers and groomers, and their combination with shape observables, in this section.

Optimizing at a single p_T : We show in Figure 39 the performance of the top taggers, using just the reconstructed top mass as the discriminating variable, with all input parameters optimized to the $p_T = 1.5 - 1.6$ TeV bin, relative to the performance optimized at each p_T . We see that while the performance degrades by about 50% when the high- p_T optimized points are used at other momenta, this is only an order-one adjustment of the tagger performance, with trimming and the Johns Hopkins tagger degrading the most. The jagged behaviour of the points is due to the finite resolution of the scan. We also observe a particular effect associated with using suboptimal taggers: since taggers sometimes fail to return a top candidate, parameters optimized for a particular efficiency ϵ_S at $p_T = 1.5 - 1.6$ TeV may not return enough signal candidates to reach the same efficiency at a different p_T . Consequently, no point appears

for that p_T value. This is not often a practical concern, as the largest gains in signal discrimination and significance are for smaller values of ϵ_S , but it is something that must be considered when selecting benchmark tagger parameters and signal efficiencies.

The degradation in performance is more pronounced for the BDT combinations of the full tagger outputs, shown in Figure 40), particularly at very low signal efficiency where the optimization picks out a cut on the tail of some distribution that depends precisely on the p_T/R of the jet. Once again, trimming and the Johns Hopkins tagger degrade more markedly. Similar behaviour holds for the BDT combinations of tagger outputs plus all shape observables.

Optimizing at a single R : We perform a similar analysis, optimizing tagger parameters for each signal efficiency at $R = 1.2$, and then use the same parameters for smaller R , in the p_T 1.5-1.6 TeV bin. In Figure 41 we show the ratio of the performance of the top taggers, using just the reconstructed top mass as the discriminating variable, with all input parameters optimized to the $R = 1.2$ values compared to input parameters optimized separately at each radius. While the performance of each observable degrades at small ϵ_{sig} compared to the optimized search, the HEPTopTagger fares the worst as the observed is quite sensitive to the selected value of R . It is not surprising that a tagger whose top mass reconstruction is susceptible to background-shaping at large R and p_T would require a more careful optimization of parameters to obtain the best performance.

The same holds true for the BDT combinations of the full tagger outputs, shown in Figure 42). The performance for the sub-optimal taggers is still within an $O(1)$ factor of the optimized performance, and the HEPTopTagger performs better with the combination of all of its outputs relative to the performance with just m_t . The same behaviour holds for the BDT combinations of tagger outputs and shape observables.

Optimizing at a single efficiency: The strongest assumption we have made so far is that the taggers can be re-optimized for each signal efficiency point. This is useful for making a direct comparison of the power of different top tagging algorithms, but is not particularly practical for the LHC analyses. We now consider the effects when the tagger inputs are optimized once, in the $\epsilon_S = 0.3 - 0.35$ bin, and then used to determine the full ROC curve. We do this in the p_T 1 - 1.1 TeV bin and with $R = 0.8$.

The performance of each tagger, normalized to its performance optimized in each bin, is shown in Figure 43 for cuts on the top mass and W mass, and in Figure 44 for BDT combinations of tagger outputs and shape variables. In both plots, it is apparent that optimizing the taggers in the 0.3-0.35 efficiency bin gives comparable performance over ef-

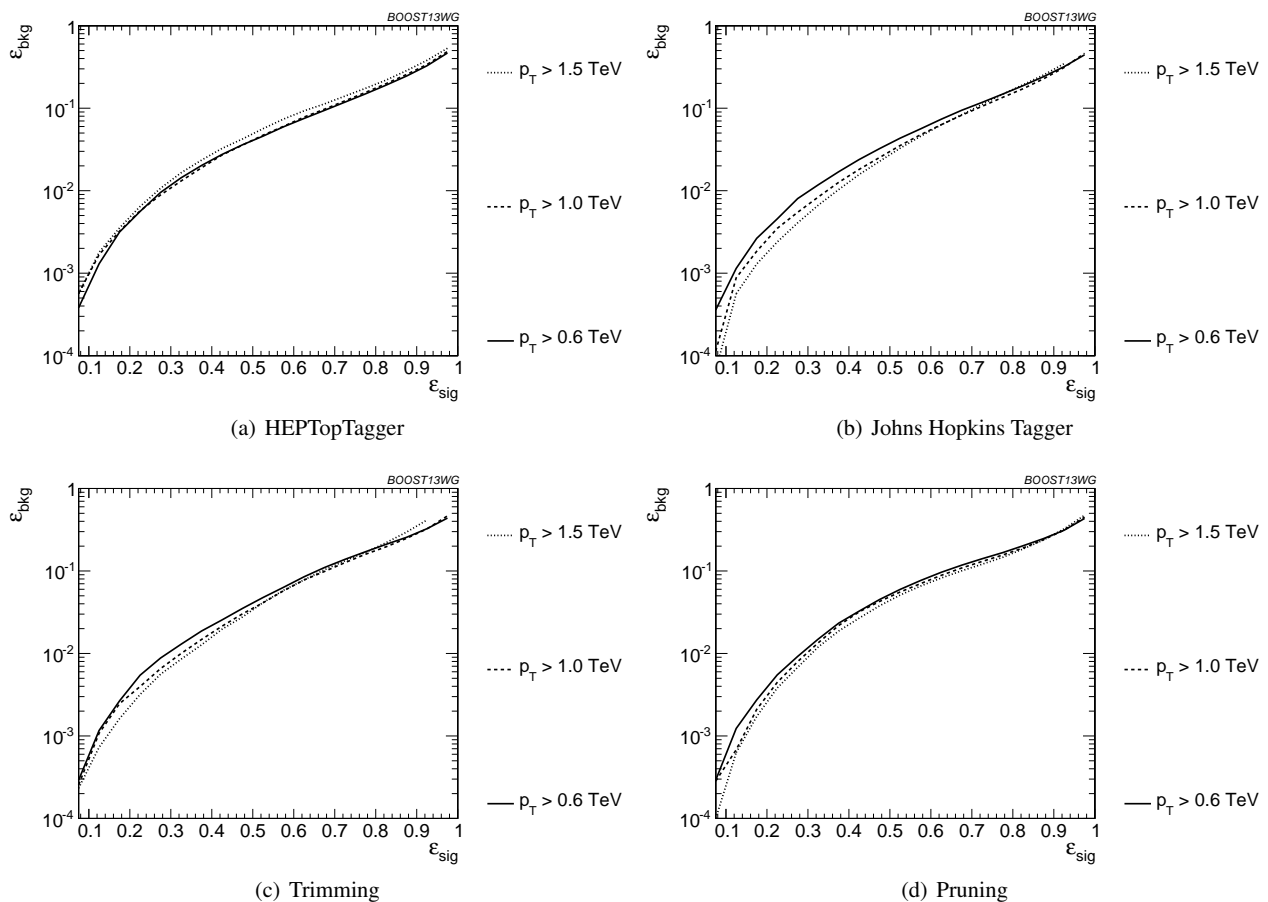


Fig. 34 Comparison of BDT combination of tagger performance at different p_T using the anti- k_T $R=0.8$ algorithm.

1187 efficiencies ranging from 0.2-0.5, although performance degrades at small and large signal efficiencies. Pruning appears to give especially robust signal-background discrimination without re-optimization, possibly due to the fact that there are no absolute distance or p_T scales that appear in the algorithm. Figures 43 and 44 suggest that, while optimization of all signal efficiencies is a useful tool for comparing different algorithms, it is not crucial to achieve good top-tagging performance in experiments.

1196 7.5 Conclusions

1197 We have studied the performance of various jet substructure observables, groomed masses, and top taggers to study the performance of top tagging at different p_T and jet radius parameter. At each p_T , R , and signal efficiency working point we optimize the parameters for those observables with tunable inputs. Overall, we have found that these techniques individually and in combination, continue to perform well at high p_T , which is important for future LHC running. In general, the John Hopkins tagger performs best, while jet grooming algorithms under-perform relative to the best top

1215 taggers due to the lack of an optimized W -identification step. Tagger performance can be improved by a further factor of 2-4 through combination with jet substructure observables such as τ_{32} , C_3 , and Qjet mass volatility; when combined with jet substructure observables, the performance of various groomers and taggers becomes very comparable, suggesting that, taken together, the observables studied are sensitive to nearly all of the physical differences between top and QCD jets. A small improvement is also found by combining the Johns Hopkins and HEPTopTaggers, indicating that different taggers are not fully correlated.

1218 Comparing results at different p_T and R , top tagging performance is generally better at smaller R due to less contamination from uncorrelated radiation. Similarly, most observables perform better at larger p_T due to the higher degree of collimation of radiation. Some observables fare worse at higher p_T , such as the N -subjettiness ratio τ_{32} and the Qjet mass volatility Γ , as higher- p_T QCD jets have more, harder emissions that fake the top jet substructure. The HEPTop-Tagger is also worse at large p_T due to the tendency of the tagger to shape backgrounds around the top mass. The p_T - and R -dependence of the multivariable combinations is

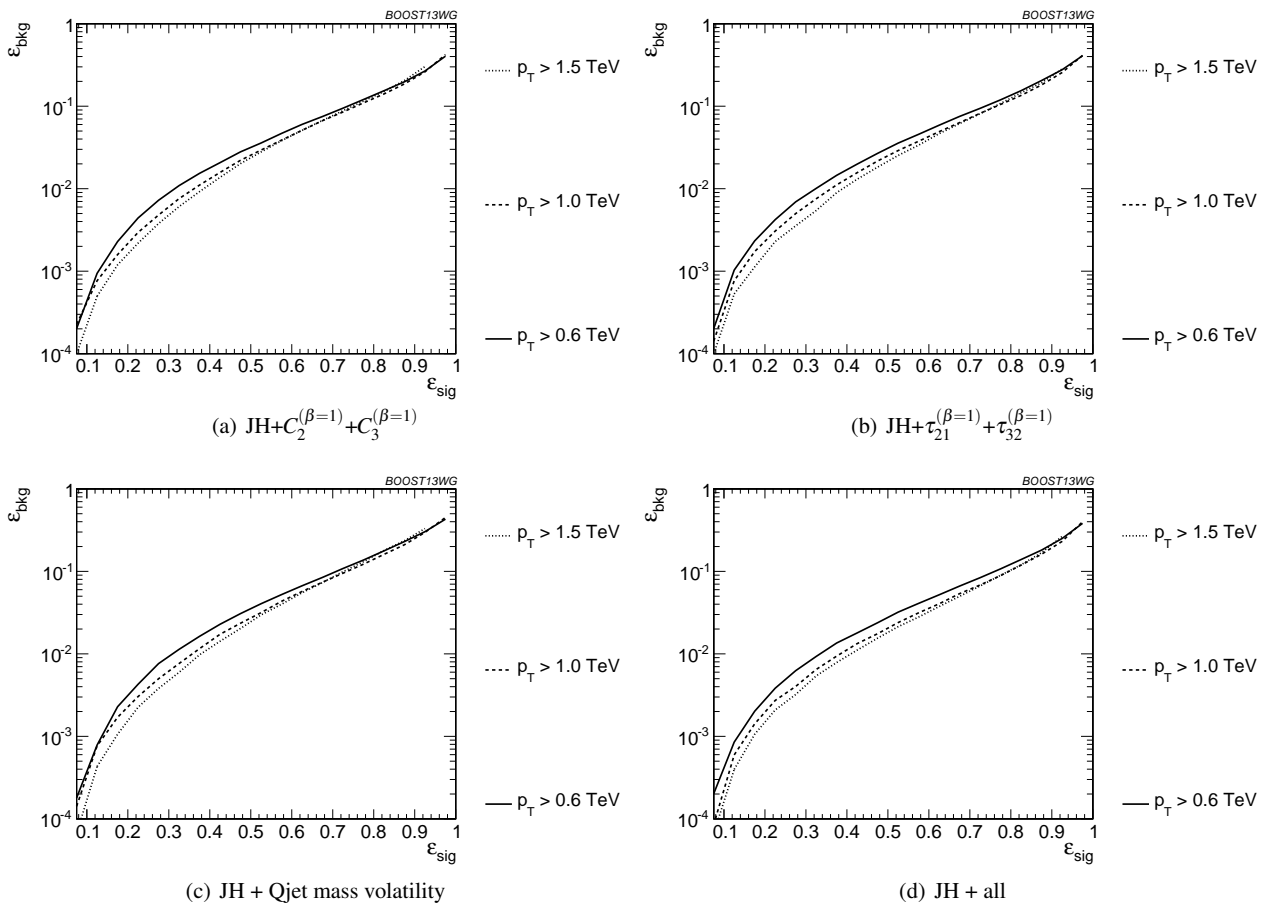


Fig. 35 Comparison of BDT combination of JH tagger + shape at different p_T using the anti- k_T $R=0.8$ algorithm.

1229 dominated by the p_T - and R -dependence of the top mass R_{249}
 1230 construction component of the tagger/groomer. 1250

1231 Finally, we consider the performance of various observables 1251
 1232 able combinations under the more realistic assumption that 1252
 1233 the input parameters are only optimized at a single p_T , R , Q_{E53}
 1234 signal efficiency, and then the same inputs are used at other 1254
 1235 working points. Remarkably, the performance of all observables 1255
 1236 is typically within a factor of 2 of the fully optimized 1256
 1237 inputs, suggesting that while optimization can lead to substantial 1257
 1238 gains in performance, the general behaviour found 1258
 1239 in the fully optimized analyses extends to more general applica- 1259
 1240 tions of each variable. In particular, the performance of 1260
 1241 pruning typically varies the least when comparing suboptimal 1261
 1242 working points to the fully optimized tagger due to the 1262
 1243 scale-invariant nature of the pruning algorithm.

1244 8 Summary & Conclusions 1263

1245 In this report we have attempted to understand the degree 1265
 1246 to which the discriminatory information in various jet sub- 1266
 1247 structure observables/taggers overlaps, and how this varies 1267
 1248 as a function of the parameters of the jets, such as their p_T 1268

and radius. This has been done by combining the variables into BDT discriminants, and comparing the background rejection power of this discriminant to the rejection power achieved by the individual variables. The performance of “all variables” BDT discriminants has also been investigated, to understand the potential of the “ultimate” tagger where “all” available information (at least, all of that provided by the variables considered) is used.

Ideas for general conclusions:

- It is clear from both the q/g tagging and W tagging studies that the correlation structure between the observables considered is complicated, being both p_T and R dependent.

1262 References

1. A. Abdesselam, E. B. Kuutmann, U. Bitenc, G. Brooijmans, J. Butterworth, et al., *Boosted objects: A Probe of beyond the Standard Model physics*, *Eur.Phys.J. C* **71** (2011) 1661, [[arXiv:1012.5412](https://arxiv.org/abs/1012.5412)].
2. A. Altheimer, S. Arora, L. Asquith, G. Brooijmans, J. Butterworth, et al., *Jet Substructure at the Tevatron*

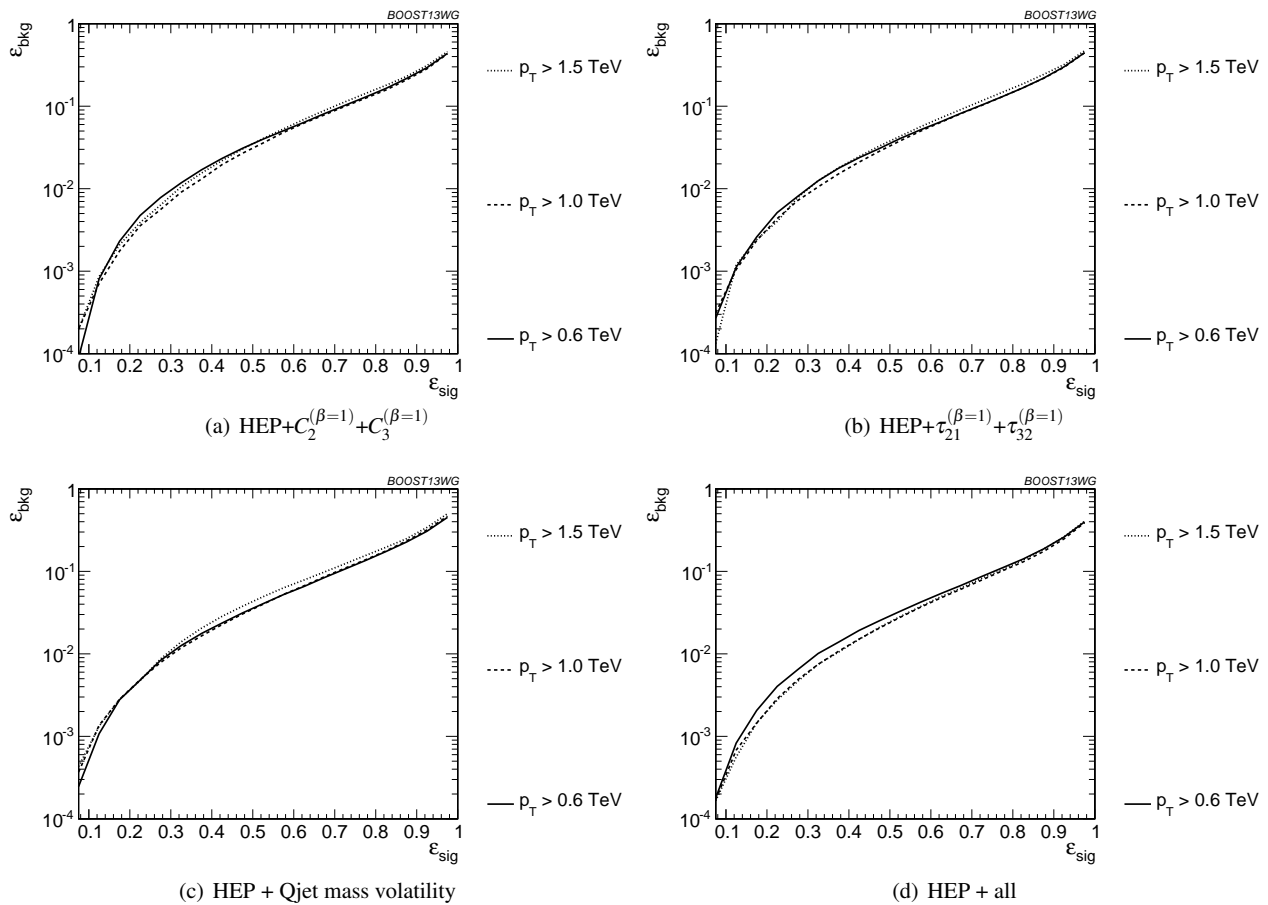


Fig. 36 Comparison of BDT combination of HEP tagger + shape at different p_T using the anti- k_T $R=0.8$ algorithm.

- 1269 and LHC: New results, new tools, new benchmarks, 1291
 1270 *J.Phys.* **G39** (2012) 063001, [[arXiv:1201.0008](#)]. 1292
 1271 3. A. Altheimer, A. Arce, L. Asquith, J. Backus Mayes, 1293
 1272 E. Bergeaas Kuutmann, et al., *Boosted objects and jet* 1294
 1273 *substructure at the LHC*, [[arXiv:1311.2708](#)]. 1295
 1274 4. M. Cacciari, G. P. Salam, and G. Soyez, *FastJet User* 1296
 1275 *Manual*, *Eur.Phys.J.* **C72** (2012) 1896, 1297
 1276 [[arXiv:1111.6097](#)]. 1298
 1277 5. T. Plehn, M. Spannowsky, M. Takeuchi, and 1299
 1278 D. Zerwas, *Stop Reconstruction with Tagged Tops*, 1300
 1279 *JHEP* **1010** (2010) 078, [[arXiv:1006.2833](#)]. 1301
 1280 6. D. E. Kaplan, K. Rehermann, M. D. Schwartz, and 1302
 1281 B. Tweedie, *Top Tagging: A Method for Identifying* 1303
 1282 *Boosted Hadronically Decaying Top Quarks*, 1304
 1283 *Phys.Rev.Lett.* **101** (2008) 142001, 1305
 1284 [[arXiv:0806.0848](#)]. 1306
 1285 7. J. Alwall, M. Herquet, F. Maltoni, O. Mattelaer, and 1307
 1286 T. Stelzer, *MadGraph 5 : Going Beyond*, *JHEP* **1106** 1308
 1287 (2011) 128, [[arXiv:1106.0522](#)]. 1309
 1288 8. Y. Gao, A. V. Gritsan, Z. Guo, K. Melnikov, 1310
 1289 M. Schulze, et al., *Spin determination of* 1311
 1290 *single-produced resonances at hadron colliders*, 1312
Phys.Rev. **D81** (2010) 075022, [[arXiv:1001.3396](#)].
 9. S. Bolognesi, Y. Gao, A. V. Gritsan, K. Melnikov,
 M. Schulze, et al., *On the spin and parity of a*
single-produced resonance at the LHC, *Phys.Rev.* **D86**
 (2012) 095031, [[arXiv:1208.4018](#)].
 10. I. Anderson, S. Bolognesi, F. Caola, Y. Gao, A. V.
 Gritsan, et al., *Constraining anomalous HVV*
interactions at proton and lepton colliders, *Phys.Rev.*
D89 (2014) 035007, [[arXiv:1309.4819](#)].
 11. J. Pumplin, D. Stump, J. Huston, H. Lai, P. M.
 Nadolsky, et al., *New generation of parton*
distributions with uncertainties from global QCD
analysis, *JHEP* **0207** (2002) 012, [[hep-ph/0201195](#)].
 12. T. Sjostrand, S. Mrenna, and P. Z. Skands, *A Brief*
Introduction to PYTHIA 8.1, *Comput.Phys.Commun.*
178 (2008) 852–867, [[arXiv:0710.3820](#)].
 13. A. Buckley, J. Butterworth, S. Gieseke, D. Grellscheid,
 S. Hoche, et al., *General-purpose event generators for*
LHC physics, *Phys.Rept.* **504** (2011) 145–233,
 [[arXiv:1101.2599](#)].
 14. T. Gleisberg, S. Hoeche, F. Krauss, M. Schonherr,
 S. Schumann, et al., *Event generation with SHERPA*

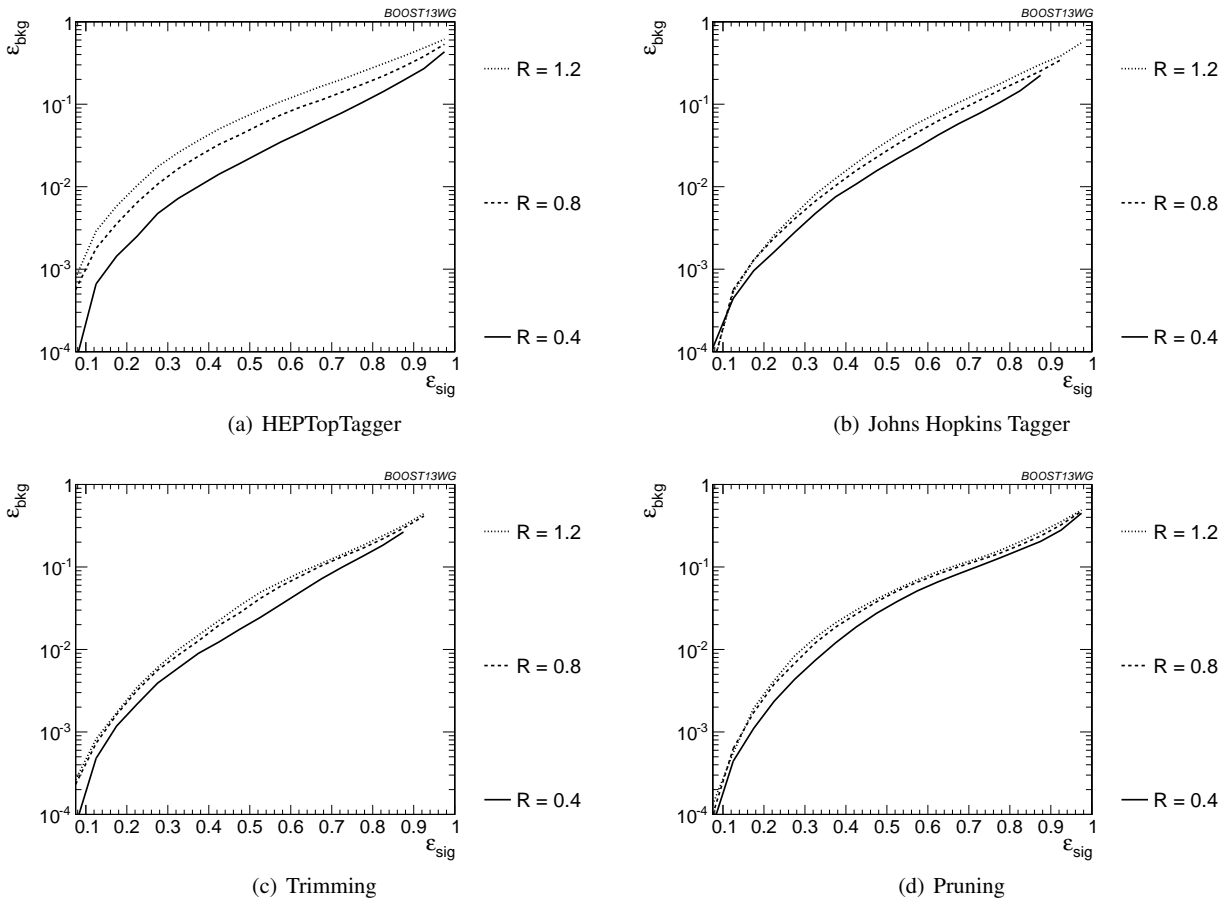


Fig. 37 Comparison of tagger and jet shape performance at different radius at $p_T = 1.5\text{-}1.6$ TeV.

- 1313 1.1, *JHEP* **0902** (2009) 007, [[arXiv:0811.4622](#)]. 1334 21. M. Cacciari, G. P. Salam, and G. Soyez, *The Anti- $k(t)$*
1314 15. S. Schumann and F. Krauss, *A Parton shower* 1335 *jet clustering algorithm*, *JHEP* **0804** (2008) 063,
1315 *algorithm based on Catani-Seymour dipole* 1336 [[arXiv:0802.1189](#)].
1316 *factorisation*, *JHEP* **0803** (2008) 038, 1337 22. Y. L. Dokshitzer, G. Leder, S. Moretti, and B. Webber,
1317 [[arXiv:0709.1027](#)]. 1338 *Better jet clustering algorithms*, *JHEP* **9708** (1997)
1318 16. F. Krauss, R. Kuhn, and G. Soff, *AMEGIC++ 1.0: A* 1339 001, [[hep-ph/9707323](#)].
1319 *Matrix element generator in C++*, *JHEP* **0202** (2002) 1340 23. M. Wobisch and T. Wengler, *Hadronization*
1320 044, [[hep-ph/0109036](#)]. 1341 *corrections to jet cross-sections in deep inelastic*
1321 17. T. Gleisberg and S. Hoeche, *Comix, a new matrix* 1342 *scattering*, [[hep-ph/9907280](#)].
1322 *element generator*, *JHEP* **0812** (2008) 039, 1343 24. S. Catani, Y. L. Dokshitzer, M. Seymour, and
1323 [[arXiv:0808.3674](#)]. 1344 B. Webber, *Longitudinally invariant K_t clustering*
1324 18. S. Hoeche, F. Krauss, S. Schumann, and F. Siegert, 1345 *algorithms for hadron hadron collisions*, *Nucl.Phys.*
1325 *QCD matrix elements and truncated showers*, *JHEP* 1346 **B406** (1993) 187–224.
1326 **0905** (2009) 053, [[arXiv:0903.1219](#)]. 1347 25. S. D. Ellis and D. E. Soper, *Successive combination jet*
1327 19. M. Schonherr and F. Krauss, *Soft Photon Radiation in* 1348 *algorithm for hadron collisions*, *Phys.Rev.* **D48** (1993)
1328 *Particle Decays in SHERPA*, *JHEP* **0812** (2008) 018, 1349 3160–3166, [[hep-ph/9305266](#)].
1329 [[arXiv:0810.5071](#)]. 1350 26. S. D. Ellis, A. Hornig, T. S. Roy, D. Krohn, and M. D.
1330 20. **JADE Collaboration** Collaboration, S. Bethke et al., 1351 Schwartz, *Qjets: A Non-Deterministic Approach to*
1331 *Experimental Investigation of the Energy Dependence* 1352 *Tree-Based Jet Substructure*, *Phys.Rev.Lett.* **108** (2012)
1332 *of the Strong Coupling Strength*, *Phys.Lett.* **B213** 1353 182003, [[arXiv:1201.1914](#)].
1333 (1988) 235. 1354 27. S. D. Ellis, C. K. Vermilion, and J. R. Walsh,
1355 *Recombination Algorithms and Jet Substructure:*

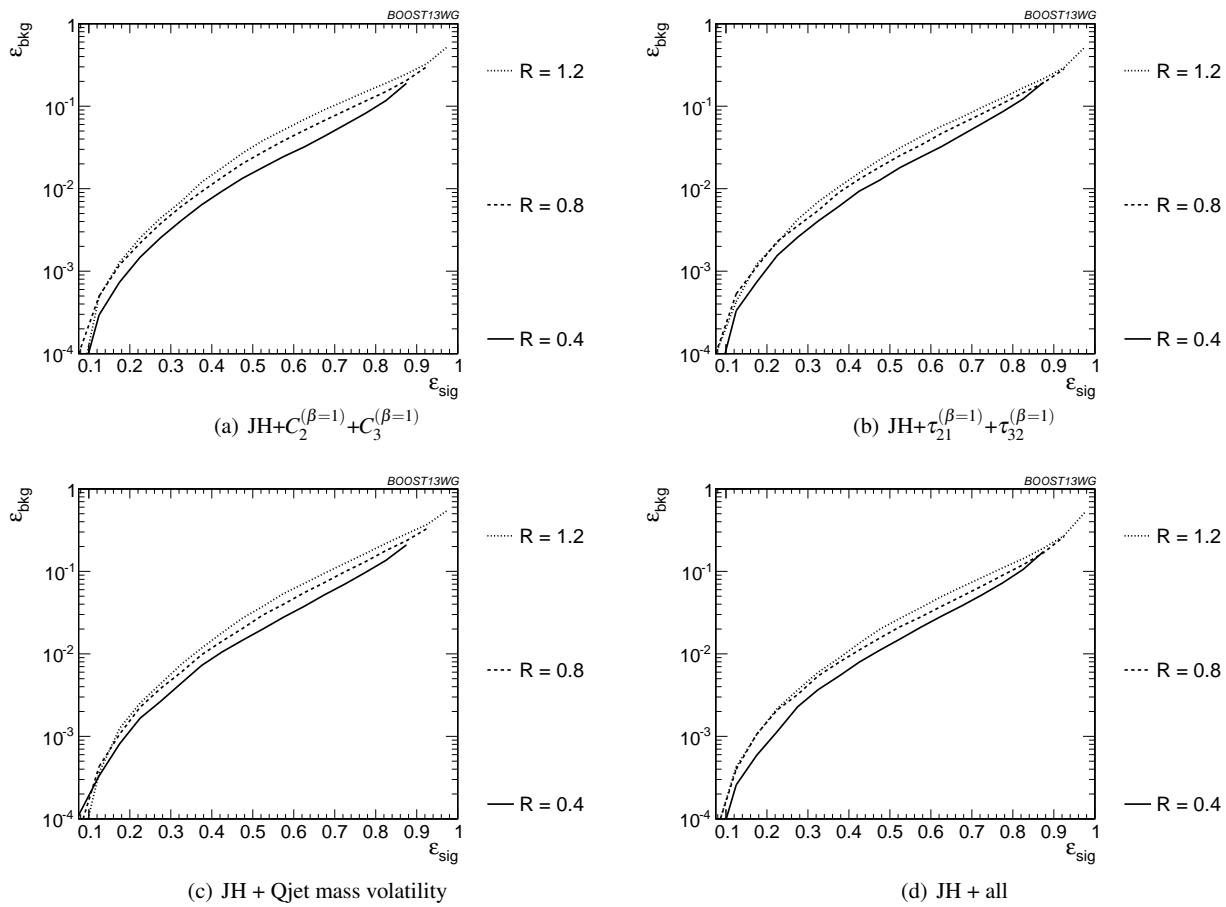


Fig. 38 Comparison of BDT combination of JH tagger + shape at different radius at $p_T = 1.5-1.6$ TeV.

- 1356 *Pruning as a Tool for Heavy Particle Searches,* 1378
 1357 *Phys.Rev.* **D81** (2010) 094023, [[arXiv:0912.0033](#)]. 1379
- 1358 28. D. Krohn, J. Thaler, and L.-T. Wang, *Jet Trimming,* 1380
 1359 *JHEP* **1002** (2010) 084, [[arXiv:0912.1342](#)]. 1381
- 1360 29. J. M. Butterworth, A. R. Davison, M. Rubin, and G. P. Salam, *Jet substructure as a new Higgs search channel* 1382
 1361 *at the LHC, Phys.Rev.Lett.* **100** (2008) 242001, 1384
 1362 [[arXiv:0802.2470](#)]. 1385
- 1363 30. A. J. Larkoski, S. Marzani, G. Soyez, and J. Thaler, 1386
 1364 *Soft Drop, JHEP* **1405** (2014) 146, 1387
 1365 [[arXiv:1402.2657](#)]. 1388
- 1366 31. M. Dasgupta, A. Fregoso, S. Marzani, and G. P. Salam, 1389
 1367 *Towards an understanding of jet substructure, JHEP*
 1368 **1309** (2013) 029, [[arXiv:1307.0007](#)].
- 1369 32. J. Thaler and K. Van Tilburg, *Identifying Boosted*
 1370 *Objects with N-subjettiness, JHEP* **1103** (2011) 015,
 1371 [[arXiv:1011.2268](#)]. 1372
- 1373 33. A. J. Larkoski, D. Neill, and J. Thaler, *Jet Shapes with*
 1374 *the Broadening Axis, JHEP* **1404** (2014) 017,
 1375 [[arXiv:1401.2158](#)].
- 1376 34. A. J. Larkoski and J. Thaler, *Unsafe but Calculable:*
 1377 *Ratios of Angularities in Perturbative QCD, JHEP*
 1309 (2013) 137, [[arXiv:1307.1699](#)].
35. A. J. Larkoski, G. P. Salam, and J. Thaler, *Energy*
Correlation Functions for Jet Substructure, JHEP **1306**
 (2013) 108, [[arXiv:1305.0007](#)].
36. A. Hoecker, P. Speckmayer, J. Stelzer, J. Therhaag,
 E. von Toerne, and H. Voss, *TMVA: Toolkit for*
Multivariate Data Analysis, PoS ACAT (2007) 040,
 [[physics/0703039](#)].
37. C. Anders, C. Bernaciak, G. Kasieczka, T. Plehn, and
 T. Schell, *Benchmarking an Even Better*
HEPTopTagger, Phys.Rev. **D89** (2014) 074047,
 [[arXiv:1312.1504](#)].

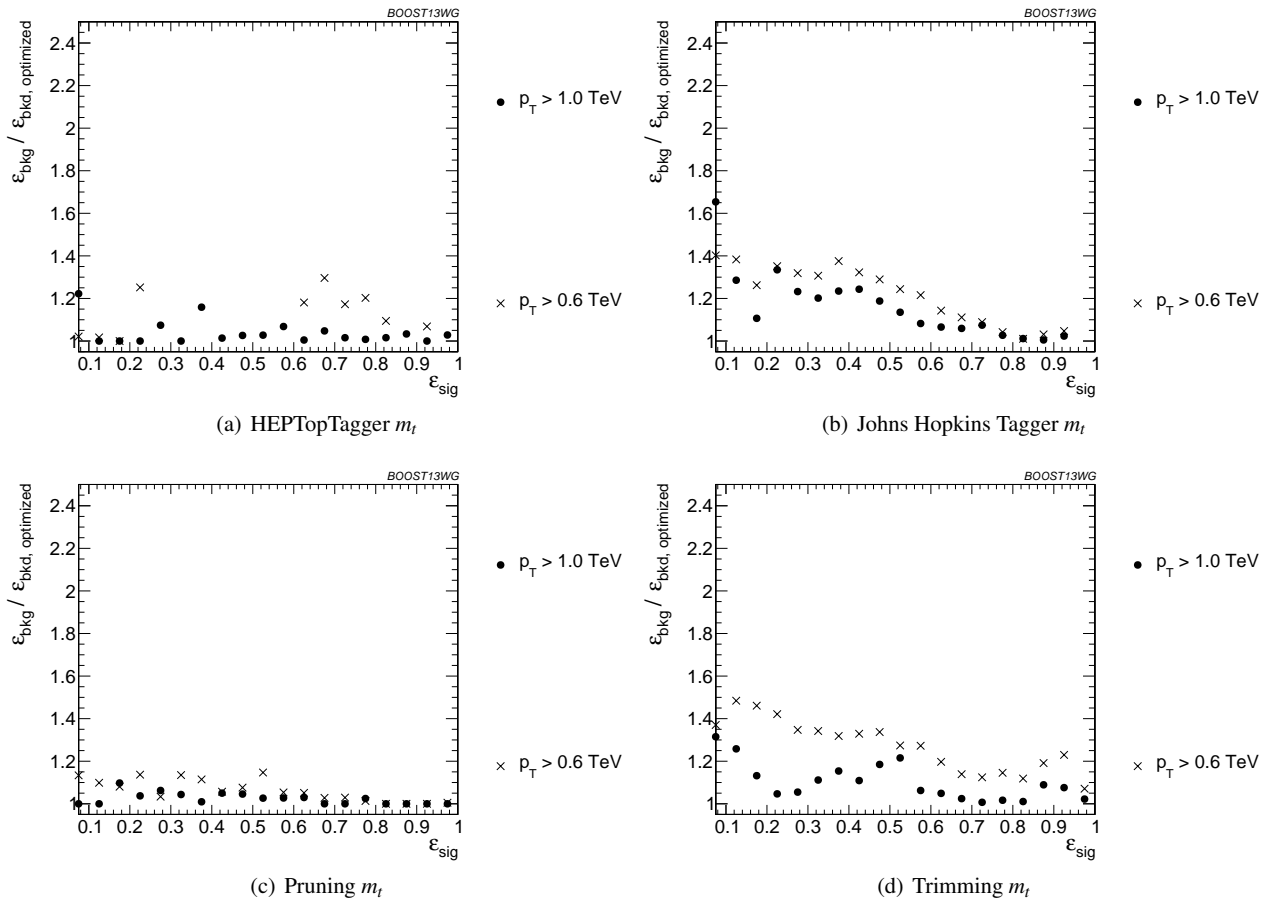


Fig. 39 Comparison of top mass performance of different taggers at different p_T using the anti- k_T $R=0.8$ algorithm; the tagger inputs are set to the optimum value for $p_T = 1.5 - 1.6$ TeV.

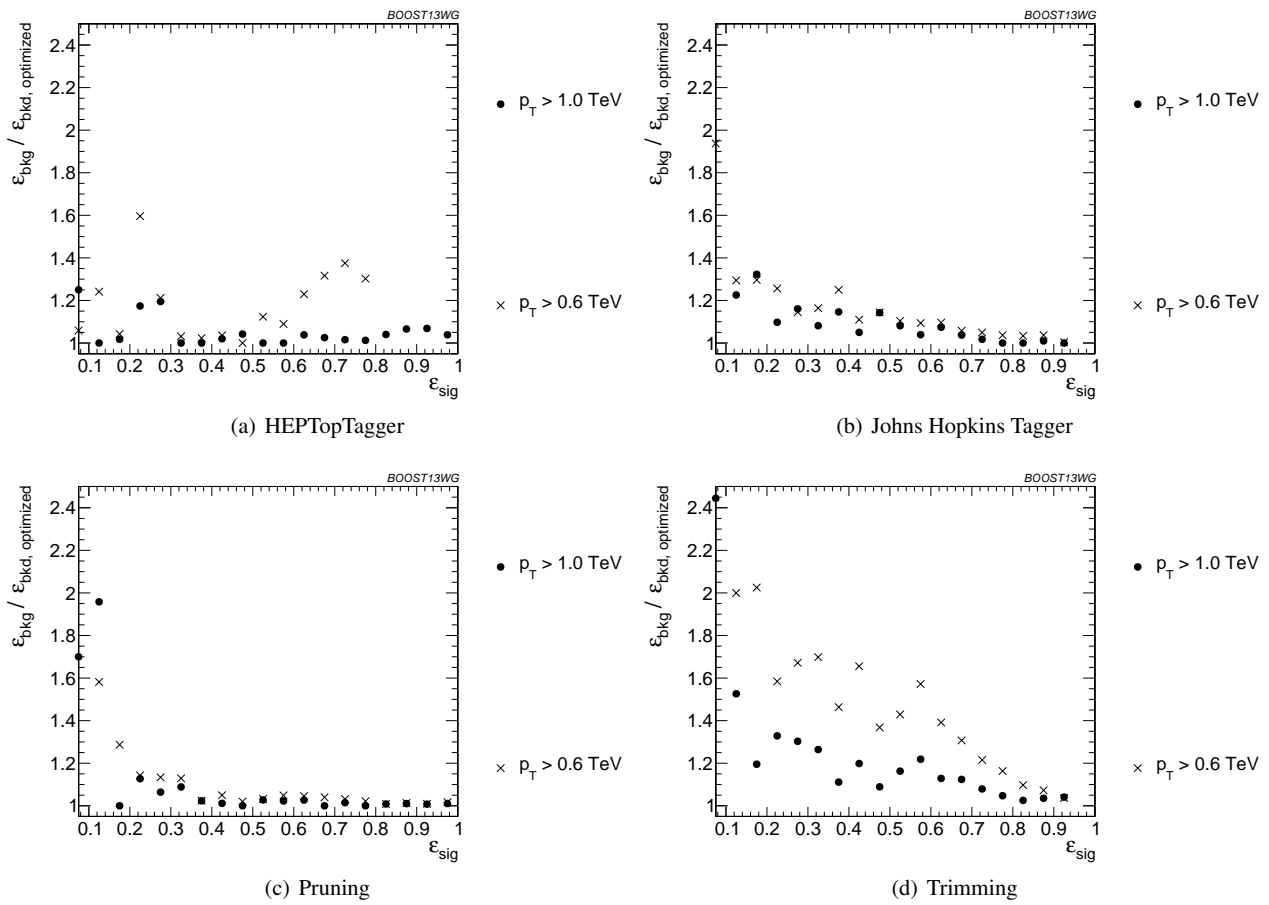


Fig. 40 Comparison of BDT combination of tagger performance at different p_T using the anti- k_T $R=0.8$ algorithm; the tagger inputs are set to the optimum value for $p_T = 1.5 - 1.6$ TeV.

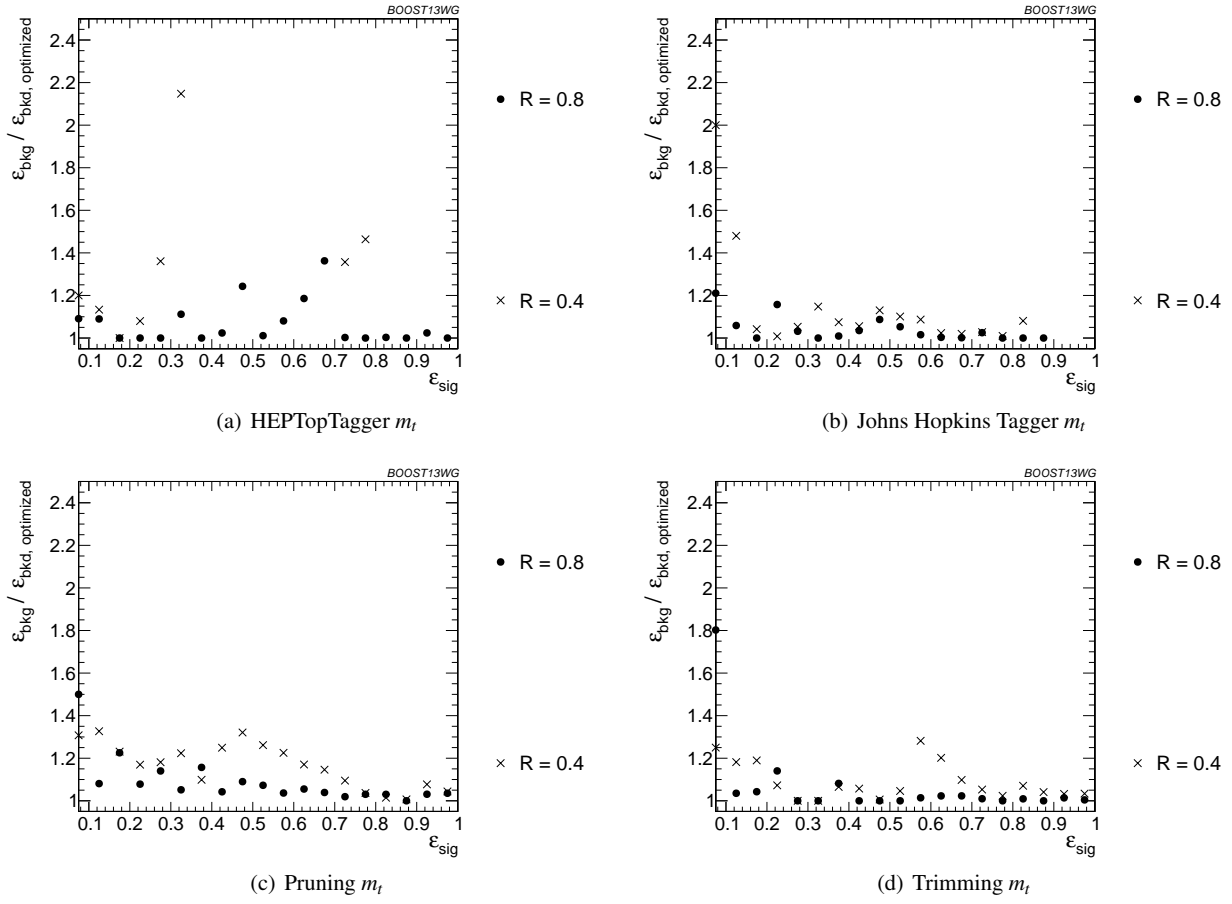


Fig. 41 Comparison of top mass performance of different taggers at different R in the $p_T = 1500 - 1600$ GeV bin; the tagger inputs are set to the optimum value for $R = 1.2$.

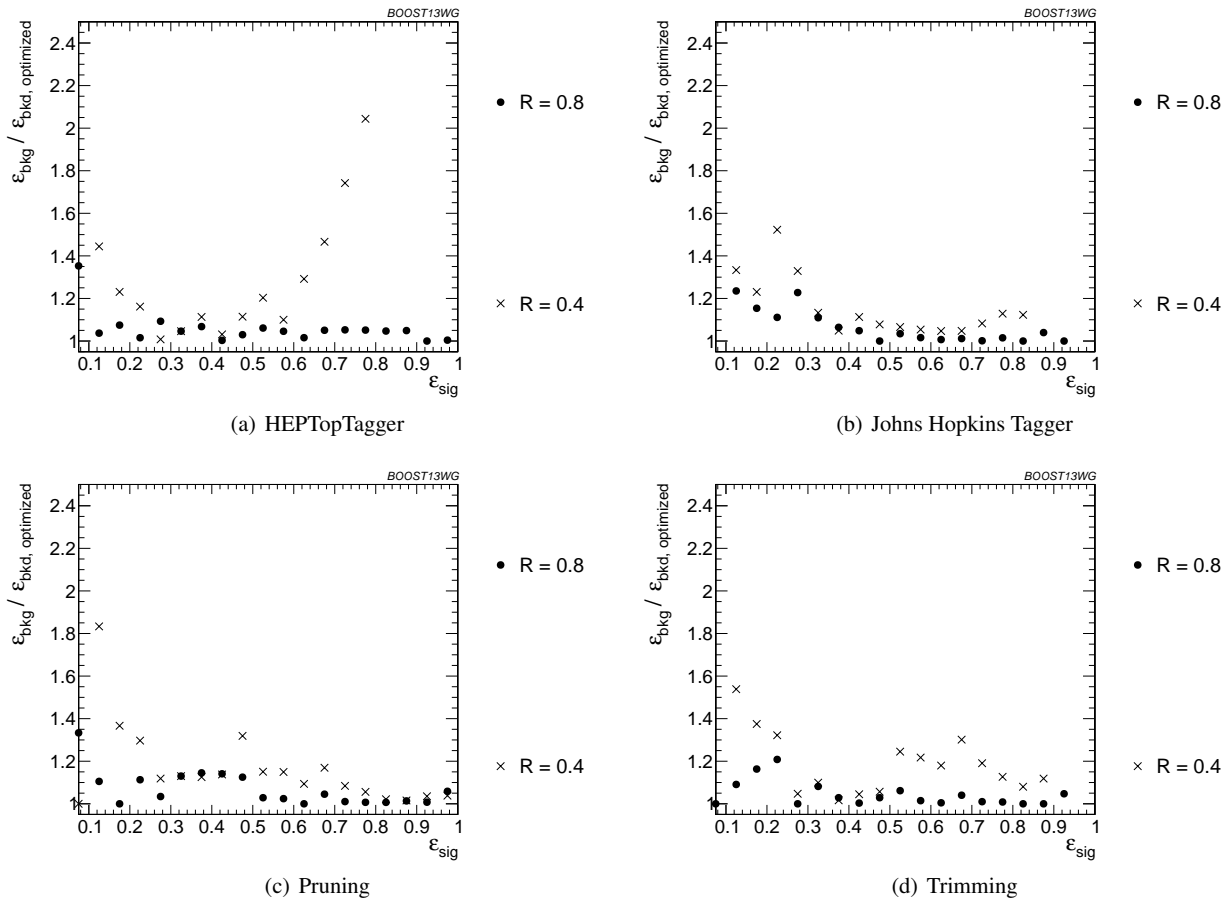


Fig. 42 Comparison of BDT combination of tagger performance at different radius at $p_T = 1.5-1.6$ TeV; the tagger inputs are set to the optimum value for $R = 1.2$.

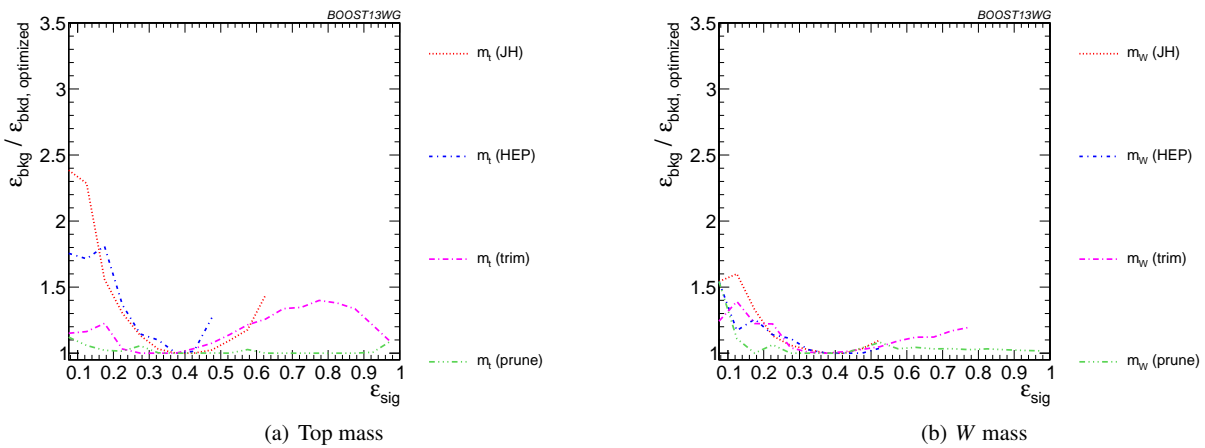


Fig. 43 Comparison of single-variable top-tagging performance in the $p_T = 1 - 1.1$ GeV bin using the anti- k_T , $R=0.8$ algorithm; the inputs for each tagger are optimized for the $\epsilon_{\text{sig}} = 0.3 - 0.35$ bin.

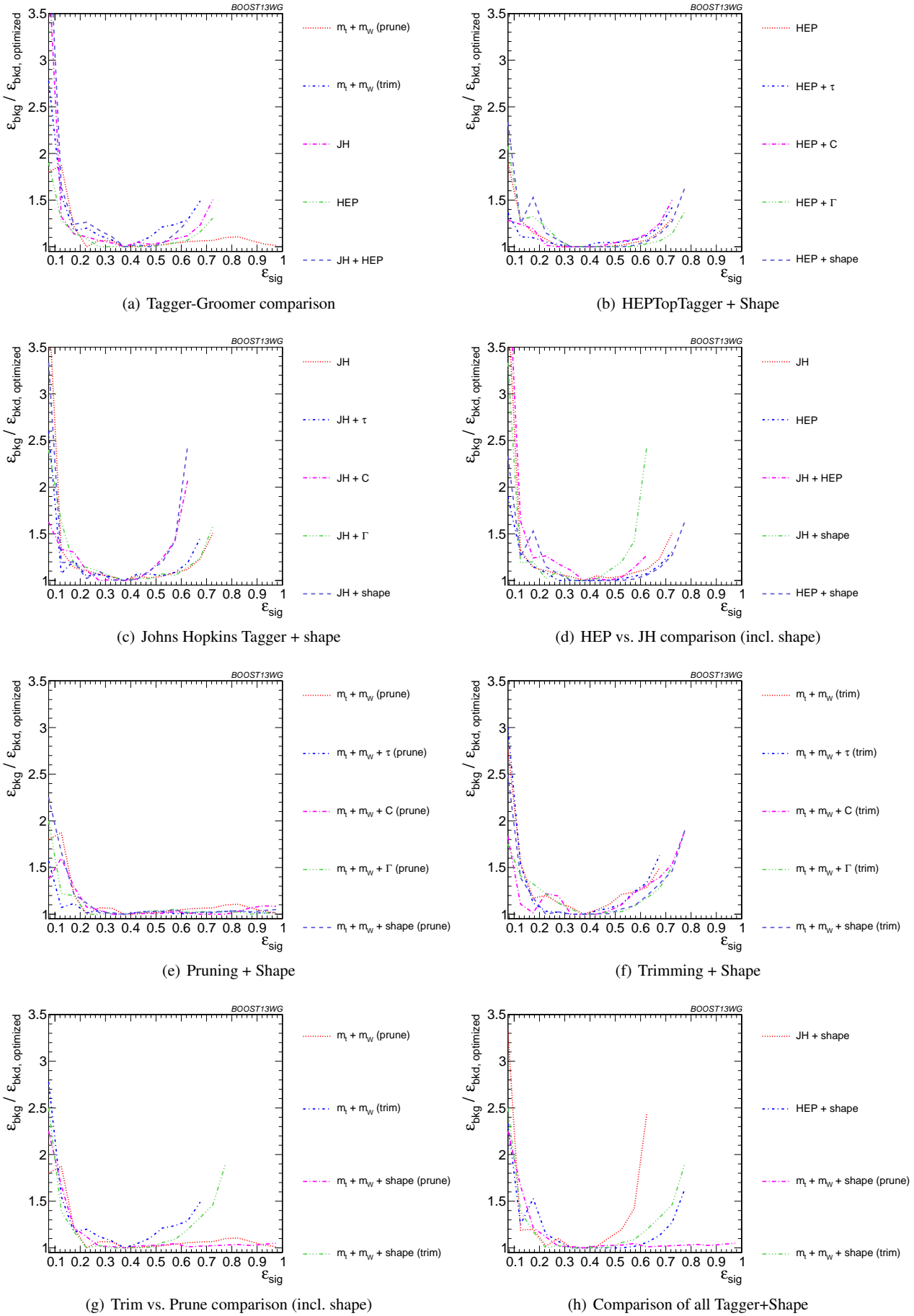


Fig. 44 The BDT combinations in the $p_T = 1 - 1.1$ TeV bin using the anti- k_T $R=0.8$ algorithm. Taggers are combined with the following shape observables: $\tau_{21}^{(\beta=1)} + \tau_{32}^{(\beta=1)}$, $C_2^{(\beta=1)} + C_3^{(\beta=1)}$, Γ_{Qjet} , and all of the above (denoted “shape”). The inputs for each tagger are optimized for the $\epsilon_{\text{sig}} = 0.3 - 0.35$ bin.